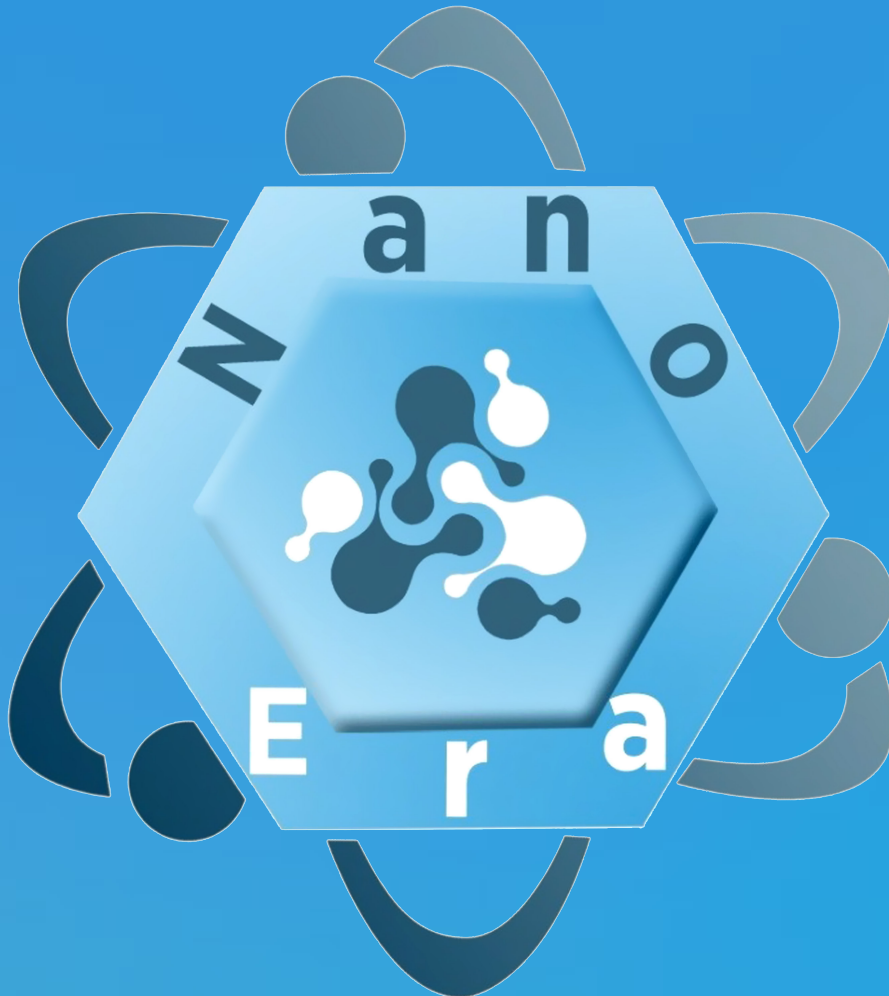




NanoEra

*Official journal of Atatürk University,
Nanoscience and Nanoengineering Research and Application Center*

Volume 3 • Issue 2 • December 2023



Editor

Hayrunnisa NADAROĞLU 

Atatürk University, Vocational School of Technical Sciences & Nanoscience and Nanoengineering Research and Application Center, Erzurum, Turkey

Associate Editors

Melike SEVİM 

Department of Inorganic Chemistry, Atatürk University, Faculty of Science, Erzurum, Turkey

Mustafa Tolga YURTCAN 

Department of Science Education, Atatürk University, Kazım Karabekir Faculty of Education, Erzurum, Turkey

Editorial Board

Karim ABBASIAN

Department of Biomedical Engineering, University of Tabriz, Faculty of Electrical and Computer Engineering, Tabriz, Iran

Azize ALAYLI

Sakarya University of Applied Sciences, Faculty of Health Sciences, Sakarya, Turkey

Özlem BARIŞ

Department of Nanoscience and Nanoengineering, Graduate School of Natural and Applied Sciences, Atatürk University, Erzurum, Turkey

Ayşe BAYRAKÇEKEN YURTCAN

Department of Chemical Engineering, Faculty of Engineering, Atatürk University, Erzurum, Turkey

Siti Amaniah Mohd CHACHULI

Fakulti Kejuruteraan Elektronik & Kejuruteraan Komputer, Universiti Teknikal Malaysia Melaka, Melaka, Malaysia

Meltem ÇETİN

Department of Pharmaceutical Technology, Atatürk University, Faculty of Pharmacy, Erzurum, Turkey

Mehmet ERTUĞRUL

Department of Metallurgical and Materials Engineering, Karadeniz Teknik University, Faculty of Engineering, Trabzon, Turkey

Emre GÜR

Department of Physics, Faculty of Science, Eskişehir Osmangazi University, Eskişehir, Turkey

Ahmet HACİMÜFTÜOĞLU

Department of Medical Pharmacology, Atatürk University, Faculty of Medicine, Erzurum, Turkey

Mohd Nizar HAMIDON

Department of Electrical And Electronic Engineering, Universiti Putra Malaysia, Faculty of Engineering, Selangor, Malaysia

Bouchaib HARTITI

FST de Mohammédia; Departement de Physique BP146, Université Hassan II de Casablanca, Mohammedia, Morocco

Pegah JAVADPOUR

Shahid Beheshti University of Medical Sciences, Iran

Ismayadi ISMAIL

Institute of Advanced Technology, Universiti Putra Malaysia, Selangor, Malaysia

Asgar LESANI

Department of Applied Chemistry, Faculty of Chemistry, Tabriz University, Tabriz, Iran

Hilal Kübra SAĞLAM

Department of Electrical And Electronics Engineering, Atatürk University, Faculty of Engineering, Erzurum, Turkey

Melike SEVİM

Department of Inorganic Chemistry, Atatürk University, Faculty of Science, Erzurum, Turkey

Zainab YUNUSA

Department of Electrical Engineering, University of Hafr Al Batin, Saudi Arabia

M. Tolga YURTCAN

Department of Science Education, Atatürk University, Kazım Karabekir Faculty of Education, Erzurum, Turkey



Founder

İbrahim KARA

General Manager

Ali ŞAHİN

Finance Coordinator

Sinem Fehime İLHAN

Journal Managers

Deniz KAYA
Irmak BERBEROĞLU
Arzu ARI

Publications Coordinators

Alara ERGİN
İrem ÖZMEN
Derya AZER
Beril TEKAY
Nisanur ATICI
Şeref Mert GÜCÜN
Simge AKKAŞ

Web Specialists

Erdem Ercivan
Doğan Oruç

Project Assistant

Batuhan Kara

Contact

Publisher: Atatürk University
Address: Atatürk University, Yakutiye,
Erzurum, Türkiye

Publishing Service: AVES
Address: Büyükdere Cad. 199/6, 34394, Şişli,
İstanbul, Türkiye
Phone: +90 212 217 17 00
E-mail: info@avesyayincilik.com
Webpage: www.avesyayincilik.com

AIMS AND SCOPE

NanoEra is a peer reviewed, open access, online-only journal published by the Atatürk University, Nanoscience and Nanoengineering Research and Application Center.

NanoEra is a biannually journal that is published in English in June, and December.

Aims, Scope, and Audience

NanoEra aims to contribute to the literature by publishing manuscripts at the highest scientific level in the fields of nanoscience and nanoengineering. The NanoEra journal publishes international scientific Research and Review articles in English (US).

Scope of the journal is all fields that are directly or indirectly related to research on the design, characterization, fabrication, and applications of structures, devices, and systems involving the manipulation or control of atomic, molecular, and nanoscale materials, and events.

NanoEra is currently indexed in EBSCO.

Research areas covered in the journal:

- 2D Materials
- Biomaterials & Nanobiotechnology
- Computational Nanotechnology
- Energy Storage & Applications
- Nanoelectronic Systems, Components & Devices
- Nanofabrication, Nanoprocessing & Nanomanufacturing
- Nanomaterials, Their Applications & Characterization
- Nanomedicine, Toxicology, Drug Delivery Systems & Biopharmaceutical
- Nanotechnology in Construction Industry
- Nanotechnology for Green Energy & Environment Sciences
- Organic and Inorganic Nanocomposites, Polymers
- Smart Textiles & Apparels

The target audience of the journal includes researchers and specialists who are interested or working in all fields of scope of the journal.

Disclaimer

The statements or opinions expressed in the manuscripts published in the journal reflect the views of the author(s) and not the views of the editors, editorial board, and/or publisher. The editors, editorial board, and publisher are not responsible for the content of the manuscripts and do not necessarily endorse the views expressed in them. It is the responsibility of the authors to ensure that their work is accurate and well-researched, and the views expressed in their manuscripts are their own. The editors, editorial board, and publisher simply provide a platform for the authors to share their work with the scientific community.

Open Access Statement

NanoEra is an open access publication.

All content published in the journal is licensed under the Creative Commons Attribution-NonCommercial-NoDerivatives 4.0 International License (CC BY-NC-ND) which allows third parties to read and share the material immediately upon publication for only non-commercial purposes by giving the appropriate credit to the original work. Adaptation and modification of the material are not permitted.

All published content is available online, free of charge at <https://nanoera-ataunipress.org/EN>.

You can find the current version of the Instructions to Authors at <https://nanoera-ataunipress.org/en/instructions-to-authors-107>

Editor in Chief: Hayrunnisa NADAROĞLU

Address: Atatürk University, Vocational School of Technical Sciences & Nanoscience and Nanoengineering Research and Application Center, Erzurum, Türkiye

E-mail: hnisa25@atauni.edu.tr

Publisher: Atatürk University

Address: Atatürk University, Yakutiye, Erzurum, Türkiye

Publishing Service: AVES

Address: Büyükdere Cad., 199/6, 34394 Şişli, İstanbul, Türkiye

Phone: +90 212 217 17 00

E-mail: info@avesyayincilik.com

Webpage: www.avesyayincilik.com

CONTENTS

Research Articles

- 28** Numerical Analysis of Heat Transfer of Polyethylene Nanocomposites with Carbon Nanotubes
Mansur MUSTAFAOĞLU
- 34** Polyvinyl Alcohol/Titanium dioxide Fibers Prepared Via Electrospinning Methods for Potential Application of Water Treatment
Cik Rohaida Che HAK
- 40** Experimental Investigation of Conical Spring Inserts on In-Tube Heat Transfer and Pressure Drop
Muhammet Kaan YEŞİLYURT, Ömer ÇOMAKLI
- 53** Nonporous Carbon-Supported Platinum Catalyst for Polymer Electrolyte Membrane Fuel Cell
Ayşenur ÖZTÜRK AYDIN, Ayşe BAYRAKÇEKEN YURTCAN
- 61** Nano-Clean: Titanium Dioxide Nanoparticles Via Sol–Gel for Effective Pollutant Removal
Bachir YAOU BALARABE, Irédon ADJAMA, Moumouni Wagé ABDOUL RAZAK, Hassimi MOUSSA, Abdoul Bari IDI AWALI, Maman Nasser ILLIASSOU OUMAROU



Numerical Analysis of Heat Transfer of Polyethylene Nanocomposites with Carbon Nanotubes

Mansur MUSTAFAOĞLU 

Independent Researcher

ABSTRACT

Nanotechnology, with its gigantic nature, has broken the boundaries of different branches of science and provided the basis for using the results and possibilities in many areas to improve the quality of life. This approach will help you systematically investigate the impact of volume percentage and aspect ratio on the thermal conductivity coefficient of carbon nanotube nanoparticles within a Representative Volume Elements (RVE) using Monte Carlo simulations in MATLAB. The aim of this study was to model the thermal conductivity of polyethylene-based composite reinforced with helical carbon nanotubes using the finite element method. It shows that the heat conduction coefficient value increases with the increase in the volume percentage, aspect ratio, and radius of helical nanoparticles, and this increase is the most effective factor for the volume percentage between 0.73% and 9.5%.

Keywords: Finite elements, helical carbon nanotubes, nano, nanocomposite

INTRODUCTION

The findings regarding the thermal behavior of nanocomposite materials with carbon nanotubes (CCNTs) have broader implications that significantly contribute to the field of nanocomposite materials and various related areas. Here are some of the broader implications:

Advanced Material Design

The research findings enable the development of advanced nanocomposite materials with tailored thermal properties. This contributes to the field by expanding the toolkit for material scientists and engineers, allowing them to design materials with enhanced thermal performance for specific applications.

Improved Thermal Management

Nanocomposite materials with optimized thermal behavior can be used to address thermal management challenges in a wide range of industries, including electronics, aerospace, automotive, and energy storage. This has the potential to improve the efficiency, reliability, and life span of various devices and systems.

Energy Efficiency and Sustainability

The ability to create nanocomposites with improved thermal properties can lead to more energy-efficient technologies, reducing energy consumption and greenhouse gas emissions. This aligns with global sustainability goals and contributes to the development of environmentally friendly solutions.

Materials for Emerging Technologies

Emerging technologies, such as 5G, electric vehicles, and renewable energy systems, often require advanced thermal management solutions. The findings offer insights into developing materials that can meet the demanding requirements of these technologies.

Phonon Engineering

Understanding how parameters like defects and functionalization impact phonon behavior in nanocomposites provides a foundation for phonon engineering. This is critical for the development of materials that can control and manipulate heat conduction, not only in nanocomposites but also in other materials and devices.

Multidisciplinary Collaboration

Research in the field of nanocomposite materials involves collaboration between materials scientists, physicists, chemists, and engineers. The findings encourage multidisciplinary efforts to address complex challenges and develop innovative solutions.



Received: 10.11.2023

Accepted: 29.11.2023

Publication Date: 31.12.2023

Corresponding author:

Mansur MUSTAFAOĞLU

Email: mansur.mustafaoglu@
morecycle.com.tr

Cite this article as: Mustafaoğlu M. Numerical analysis of heat transfer of polyethylene nanocomposites with carbon nanotubes. *NanoEra* 2023;3(2):28-33.



Content of this journal is licensed under a Creative Commons Attribution-NonCommercial-NoDerivatives 4.0 International License.

Nanotechnology Advancements

The research contributes to the broader field of nanotechnology by expanding our understanding of how nanoscale materials like CCNTs can be harnessed to improve the properties of macroscopic materials. This knowledge can be applied to other nanomaterials and nanostructures.

Economic and Industrial Impact

Industries and companies involved in the production and application of nanocomposite materials can benefit from the development of more efficient and effective products. This can lead to economic growth and competitiveness in various markets.

In summary, the findings regarding the thermal behavior of nanocomposite materials with CCNTs have far-reaching implications, not only in the field of materials science but also in addressing real-world challenges related to energy efficiency, sustainability, and the advancement of emerging technologies. This research contributes to the development of innovative solutions and has the potential to positively impact multiple industries and sectors.

Nano comes from the Greek root "nance," meaning dwarf.¹ Nanotechnology, the fourth wave of the industrial revolution, is a huge phenomenon that has entered all scientific trends to the extent that the superiority of processes will be revealed in the next decade and will depend on this development.² The nature of nanotechnology is the ability to work at atomic, molecular, and beyond levels, using the arrangement of atoms or molecules to arrange and manipulate atoms or molecules in sizes between 1 and 100 nanometers. Replacing these structures with materials, devices, and systems with new capabilities and ensuring the higher efficiency of materials. Nanotechnology is the process of producing materials and tools by manipulating materials at the atomic scale and controlling them at the atomic and molecular level. In fact, if all materials and systems organize their basic structures at the nanoscale, then all reactions will be carried out faster and more optimally, and sustainable development will be realized.¹ Among the many achievements of this technology, the use of energy with high efficiency in its production, transmission, consumption, and storage will also be created, leading to a tremendous transformation in this field.² Practitioners and researchers of nanoscience are therefore trying to use this technology to provide greater comfort and well-being inside and outside the building by finding a new class of high-performance building materials, saving money on costs, especially the consumption of energy resources, and finally ensuring sustainable development. Nanotechnology will lead to dramatic changes in the use of natural resources, energy and water, and reducing waste and pollution.

Adding nanoparticles such as graphene nanosheets, CCNTs, helical CCNTs, clay nanoparticles, and metal oxide nanoparticles to the matrix generally increases the electrical, mechanical, material, magnetic, and optical properties. Due to its special geometric shape, significant surface-to-volume ratio, and high mechanical and thermal properties, the use of CCNT nanoparticles will increase the nanocomposite's resistance to destruction and fracture, as well as its thermal and mechanical properties.³⁻⁶ Among carbon nanotubes, helical carbon nanotubes, which have the mechanical, thermal, and electrical properties of carbon nanotubes, have recently become the focus of researchers' attention due to their geometric structure. Carbon nanotubes were predicted by Dunlap in 1990.^{7,8} Carbon nanotubes and helical carbon

nanotubes are anisotropic materials, but they are assumed to be isotropic in many studies^{9,10} and in this study as well. Based on this brief description of CCNTs, the following provides an overview of previous research. Using the finite element method, the elastic properties of CCNT polymeric nanocomposite, as well as the effect of CCNT geometric parameters, number, aspect ratio, volume fraction, and interphase, were investigated and obtained by Koc et al.¹¹

Mehrdad Shokrieh et al.¹² showed that mechanical loading improved the effective thermal resonance coefficient and increased the elastic modulus of the nanocomposite. Mehrdad Shokrieh et al.¹² numerically examined how the length of the RVE affected the mechanical properties of the nanocomposite they produced. Their findings showed that, at a fixed volume percentage, the length or width of the RVE has a big impact on the nanocomposite's longitudinal elastic modulus.

In an analytical study, Tran¹³ has a simple approach to obtain the effective heat conduction coefficient. They presented a two- and three-dimensional multiphase composite that envisions even high-volume percentages of nanoparticles. Finally, the theoretical results of his model had good agreement with the laboratory and finite element results of others.

Lu¹⁴ conducted one of the first studies examining the elastic properties of single-walled and multiwalled CNTs using binary harmonic potentials. In this study, the interaction between tubes in MNCNTs was taken into account with van der Waals forces.

Yetgin et al.¹⁵ examined the tribological and mechanical properties of graphite-added polypropylene composites in their study. For their studies, they added 1%, 3%, 5%, and 10% graphite by weight to the polypropylene polymer.

Sever et al.¹⁶ stated in their study that a large amount of agricultural waste is generated in the world as a result of agricultural harvests and pruning. They mentioned that very few of these wastes were converted and used as agricultural fertilizer and fuel, and the remaining were not utilized. In this regard, many studies have recently been carried out to combine fullerenes and CNTs.¹⁷⁻²³

According to a review of previous studies, so far no study has been reported in the sources that investigates the effect of CCNT nanoparticles on the effective thermal conductivity coefficient of nanocomposites. Ethylene's effective thermal conductivity coefficient is obtained by the two-dimensional finite element method. In this study, the assumption of a complete connection between the nanoparticles and the polymer was taken into account, and the electrical resistance between the nanoparticles and the matrix was also ignored. First of all, using a program written in MATLAB software, CCNT nanoparticles spread isotropically in the RVE with the Monte Carlo algorithm. After obtaining the appropriate RVE length, a parametric study is carried out; the effect of volume percentage and aspect ratio on the thermal conductivity coefficient of CCNT nanoparticles is investigated.

MATERIAL AND METHODS

Nowadays, composite materials are replacing metal materials, especially in the aviation industry. Carbon fiber composite materials are becoming increasingly popular due to their high strength-to-density ratio and high stiffness. In addition to the aviation industry, where strength-to-density and hardness ratios are of great importance, there are now vehicles produced entirely from carbon fiber in the maritime and automotive sectors. Boeing

787 Dreamliner and Airbus A350 are prime examples of next-generation aircraft made from carbon fiber materials.

Considering an isotropic substance in which heat transfer depends on temperature, the basic equation of heat transfer is as follows:

$$Q = \rho C \frac{\partial T}{\partial t} - \left(\frac{\partial q_x}{\partial x} + \frac{\partial q_y}{\partial y} \right) Q \quad (1)$$

where q_x and q_y (W/m^2) are the components of heat flow per surface area, (W/m^3) is the internal heat production rate per unit volume, ρ (kg/m^3) is the material density, ($kJ/kg K^{-1}$) is the heat capacity, T (K) is the temperature, and t (s) is the time. According to Fourier's law, the components of the heat flow can be written by substituting them into equation 1:

$$\frac{\partial}{\partial x} \left(k \frac{\partial T}{\partial x} \right) + \frac{\partial}{\partial y} \left(k \frac{\partial T}{\partial y} \right) + Q = \rho C \frac{\partial T}{\partial t} \quad (2)$$

where k ($W/m K^{-1}$) is the heat conduction coefficient. In this study, it is assumed that there is no heat production ($Q=0$), the heat transfer is stable, that is, $dT/dt=0$, and there is also a constant boundary condition. Temperature is applied to one side of the RVE, and heat flux is applied to the other side. Considering that the RVE in question contains CCNT helical nanoparticles of the polyethylene nanocomposite, equation 3 is used to calculate the effective conduction coefficient of the RVE:²⁴

$$k_{eff} \frac{T}{L} = q_{eff} Q_i \quad (3)$$

where T (ΔK) is the temperature difference between the 2 surfaces of the RVE after analysis, L is the length of the RVE after analysis, and (W/m^2) is the equivalent flux passing between the 2 desired surfaces of the RVE. The effective heat flux value is obtained from the following relationship:

$$q_{ff} = \left(\sum_{i=1}^N q_i v_i \right) / V \quad (4)$$

Here, V (m^3) is the total volume of the RVE, the flux passing through each element, and the volume of each element, and N is the number of elements. It can also be said that thermal resistance is assumed in this study. The gap between the nanoparticles and the matrix is 0. It is explained in the next section that the element represents volume.

In this section, the RVE is restructured in two dimensions by scattering nanoparticles into it. Then, the optimum RVE size is obtained by determining the characteristics and mechanical and thermal properties of the matrix and nanoparticles. In this study, RVE was considered a two-dimensional cubic element. By using the Monte Carlo algorithm to distribute the CCNT nanoparticles in the mentioned RVE, the coordinates of the nanoparticles were first created in a text file with a MATLAB program. To calculate the orientation of nanoparticles, the angles of the global coordinate system of the longitudinal vector of nanoparticles are defined by the Monte Carlo algorithm in the following equation:²⁵

$$\begin{cases} \theta = 2\pi a \\ \varphi = \cos^{-1}(2b-1) \end{cases} \quad (5)$$

In equation 5, θ and φ are the angles of the spherical coordinate device of the longitudinal vector of nanoparticles, as shown in Figure 1, and the coefficients a and b are 2 random numbers between 0 and 1. As an example of the distribution of CCNT nanoparticles in RVE with a volume percentage of 0.420%, the ratio of RVE length to CCNT is equal to 5.5 and 64 CCNT particles.

To make the RVE as a representative of the homogeneous volume of a heterogeneous material, after the optimal distribution of nanoparticles in it, its size also needs to be determined accurately; that is, the effective properties of the material do not depend on the size of the material. For this purpose, two different sizes of RVE with a volume percentage of 0.42% were created from nanoparticles of sizes 900 and 100 (with equal aspect ratio and volume percentage), according to Figure 2. Moreover, considering that the Monte Carlo algorithm is a random algorithm, each of the analyses was repeated 3 times, and the values presented in this study are the average of 3 heat transfer coefficients repeated so that the resulting value has less error. It is noteworthy that network growth is also used to increase the accuracy of the numerical solution and reduce the computational volume. Areas far from where the CCNT nanoparticles are located have a coarser network, but areas near the CCNT nanoparticles have a much finer network, with the total minimum number of RVE network elements being 500 000 and the number of CCNT nanoparticles being 50 000.

RESULTS AND DISCUSSION

The thermal conductivity coefficient was measured for both models, and according to the results reported in Figure 3, it can be seen that the responses for RVE at sizes 900 and 1000 are independent of the size of RVE.

The effects of different parameters, such as volume percentage of nanoparticles, their size, and diffusion direction, on the thermal

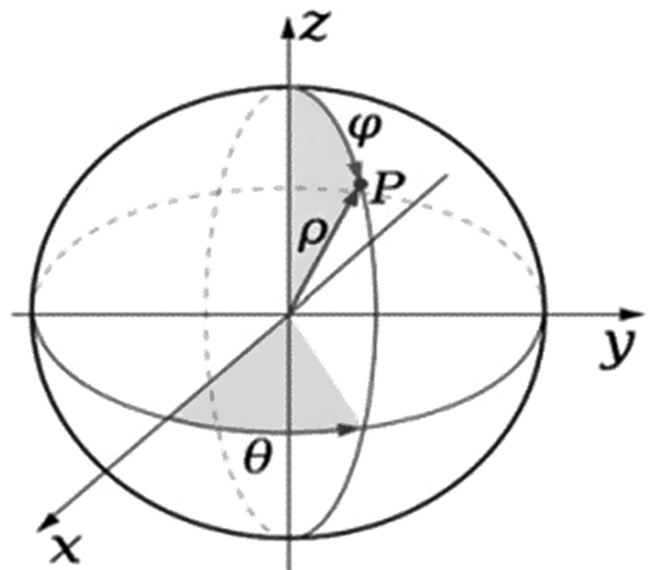


Figure 1. Spherical coordinates of the longitudinal vector of nanoparticles.²⁶

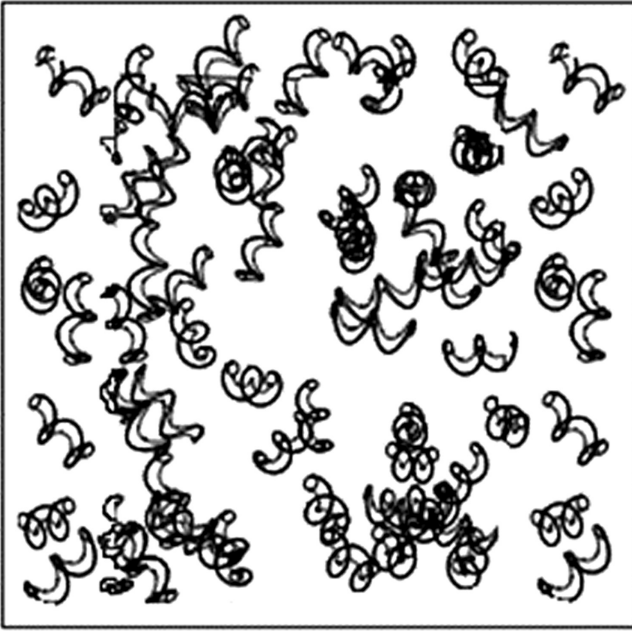


Figure 2. An example of the RVE structure containing 0.42% carbon nanotube by volume and the ratio of Representative Volume Elements (RVE) to carbon nanotube.

conductivity coefficient of the nanocomposite are discussed. The properties of nanoparticles are available in Table 1.

In order to observe the effect of the volume percentage of CCNT nanoparticles on the thermal conductivity coefficient of the nanocomposite, 4 different volume percentages of CCNT1-type CCNT nanoparticles were made, and then the resulting diagram of the finite element results was obtained as shown in Figure 4. As can be seen, the volume percentage of nanoparticles increased, and the amount of heat conduction coefficient increased continuously.

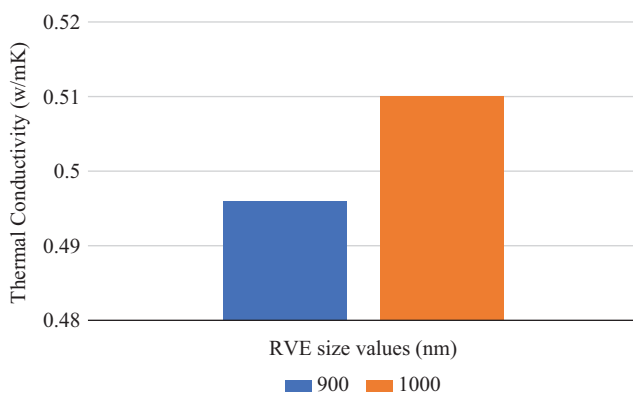


Figure 3. Thermal conduction coefficient graph of the nanocomposite for different RVE size values.

Table 1. Geometric Properties and Nomenclature of Nanoparticles

Type of Nanoparticles	Inner Diameter (nm)	Radius (nm)	Length (nm)
CCNT1	15	10	150
CCNT2	20	10	60-450
CCNT3	30-50	10	150
CCNT4	25	15	150

CCNT, carbon nanotube.

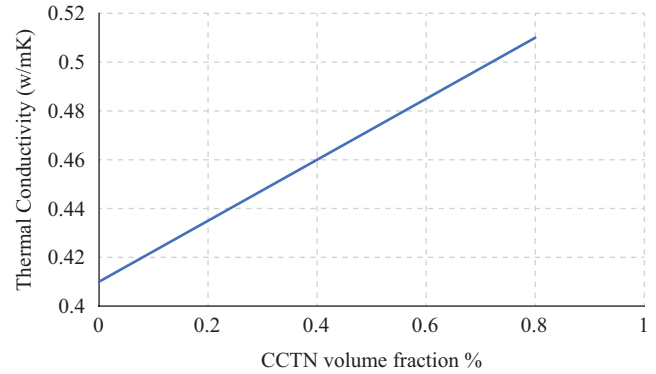


Figure 4. Graph of changes in thermal conductivity coefficient according to volume percentage of nanoparticles

The results obtained from studying the impact of various parameters on the thermal behavior of nanocomposites with CCNTs contribute to a better understanding of how these materials function and can be optimized for various applications. Here is how the results enhance our understanding:

Improved Material Design: Understanding how the volume percentage, aspect ratio, radius, and chirality of CCNTs affect thermal conductivity helps in designing nanocomposite materials with tailored thermal properties. This knowledge enables engineers and researchers to create materials with enhanced heat-transfer capabilities for specific applications, like thermal management in electronics.

Optimal Use of CCNTs: By knowing how these parameters influence thermal behavior, it becomes possible to optimize the use of CCNTs in composite materials. This can lead to more efficient and cost-effective solutions for improving heat dissipation in electronic devices, aerospace components, and other industries.

Insights into Phonon Behavior: The study of how defects and functionalization affect thermal properties sheds light on the role of phonons in heat conduction within CCNTs. This understanding can be used to control and manipulate phonon scattering, thereby enabling better control of thermal conductivity in nanocomposites.

Temperature-Dependent Behavior: Recognizing how temperature affects the thermal properties of CCNT-based nanocomposites is crucial for applications where materials operate under varying temperature conditions. This information can guide the design of materials that perform optimally at specific temperature ranges.

Practical Applications: The research results can lead to the development of advanced thermal interface materials, heat sinks, and other components that are essential for efficient heat management in electronic devices, advanced materials, and energy storage systems. This knowledge can result in more effective and durable products.

Sustainability and Energy Efficiency: Understanding how CCNT parameters impact thermal behavior can contribute to the development of materials that improve energy efficiency in various industries. This is particularly important for reducing energy consumption and carbon emissions in a range of applications. In conclusion, the results of studying the influence of parameters on the thermal behavior of nanocomposites with CCNTs provide

valuable insights into material design and optimization, as well as a deeper understanding of phonon behavior and temperature-dependent characteristics. This knowledge can be harnessed to develop more efficient and sustainable materials for a variety of applications, ultimately contributing to advancements in technology and energy management.

In this study, the effect of adding nanoparticles of helical carbon tubes to polyethylene and obtaining the thermal properties (thermal conductivity coefficient) of the resulting nanocomposite was investigated. The research method was carried out with the help of a finite element numerical solution and also by dispersing the nanoparticles using the MATLAB program with the help of the Monte Carlo algorithm. After making the desired RVEs and performing thermal analyses on them, the results showed that the thermal conductivity coefficient increased with the increase of the volume percentage, arc length, and outer or inner radius of the nanoparticles. The thermal conductivity coefficient was obtained depending on the changes in the ratio of the free length of the CCNT to its diameter, and it was observed that the value increased as this ratio increased. It is different with the increase of each of these parameters so that the volume percentage parameter has the most effect on increasing the thermal conductivity coefficient of nanocomposite by 12.5%, and the external or internal diameter of nanoparticles and also the spring length of nanoparticles have the least effect on increasing the coefficient of conductivity.

The thermal conductivity of a nanotube is influenced by several parameters, including volume percentage, aspect ratio, radius, and more. Here is a concise summary of how each of these parameters can affect the thermal conductivity coefficient of nanotubes:

Volume Percentage

Higher volume percentages of nanotubes in a composite material generally lead to increased thermal conductivity. This is because a larger volume of nanotubes provides more pathways for heat conduction through the material.

Aspect Ratio

Nanotubes with higher aspect ratios (length-to-diameter ratio) tend to have better thermal conductivity. Longer nanotubes facilitate efficient phonon (vibrational heat carrier) transport, improving overall thermal conductivity.

Radius

The radius of a nanotube can influence its thermal properties. Nanotubes of smaller diameter may exhibit better thermal conductivity due to reduced phonon scattering, allowing heat to be conducted more efficiently.

Chirality

The chirality of a nanotube, which determines its atomic arrangement, can impact thermal conductivity. Some chiralities have inherently better thermal properties due to their electronic band structure, which affects phonon behavior.

Defects and Functionalization: The presence of defects or functional groups on the nanotube surface can hinder thermal conductivity by scattering phonons. However, controlled functionalization can be used to tune thermal properties for specific applications.

Temperature

Thermal conductivity often increases with rising temperature due to increased phonon mean free path. However, at extremely

high temperatures, phonon–phonon scattering can reduce thermal conductivity.

Interactions with Surrounding Material: The thermal properties of nanotubes can be influenced by their interactions with the surrounding matrix material in composite systems. Strong nanotube–matrix interfaces can enhance thermal conductivity by promoting efficient heat transfer.

In summary, the thermal conductivity of nanotubes is influenced by a combination of intrinsic factors such as aspect ratio, radius, chirality, and defects, as well as extrinsic factors such as volume percentage and temperature. Understanding and manipulating these parameters is crucial for tailoring nanotube-based materials for specific thermal management applications.

Peer-review: Externally peer-reviewed.

Declaration of Interests: The author has no conflicts of interest to declare.

Funding: The author declared that this study has received no financial support.

REFERENCES

- Drexler KE. *Nanosystems: Molecular Machinery, Manufacturing, and Computation*. Chichester, UK: John Wiley & Sons, Inc.; 1992.
- Vasir JK, Reddy MK, Labhsetwar V. Nanosystems in drug targeting: opportunities and challenges. *Curr Nanosci*. 2005;1(1):47-64. [\[CrossRef\]](#)
- Raghubanshi H, Dikio ED, Naidoo EB. The properties and applications of helical carbon fibers and related materials: a review. *J Ind Eng Chem*. 2016;44:23-42. [\[CrossRef\]](#)
- Yousefi E, Sheidaei A, Mahdavi M, Baniassadi M, Baghani M, Faraji G. Effect of nanofiller geometry on the energy absorption capability of coiled carbon nanotube composite material. *Compos Sci Technol*. 2017;153:222-231. [\[CrossRef\]](#)
- Sharma R, Yadav AK, Panwar V, Kar KK. Viscoelastic properties of coil carbon nanotube-coated carbon fiber-reinforced polymer nanocomposites. *J Reinf Plast Compos*. 2015;34(12):941-950. [\[CrossRef\]](#)
- Gertsman VY, Hoffmann M, Gleiter H, Birringer R. The study of grain size dependence of yield stress of copper for a wide grain size range. *Acta Metall Mater*. 1994;42(10):3539-3544. [\[CrossRef\]](#)
- Itoh S, Ihara S. Toroidal forms of graphitic carbon. II. Elongated tori. *Phys Rev B Condens Matter*. 1993;48(11):8323-8328. [\[CrossRef\]](#)
- Dunlap BI. Connecting carbon tubules. *Phys Rev B Condens Matter*. 1992;46(3):1933-1936. [\[CrossRef\]](#)
- Ju SP, Lin JS, Chen HL, et al. A Molecular Dynamics study of the mechanical properties of a double-walled carbon nanocoil. *Comp Mater Sci*. 2014;82:92-99. [\[CrossRef\]](#)
- Volodin A, Ahlskog M, Seynaeve E, Van Haesendonck C, Fonseca A, Nagy JB. Imaging the elastic properties of coiled carbon nanotubes with atomic force microscopy. *Phys Rev Lett*. 2000;84(15):3342-3345. [\[CrossRef\]](#)
- Khani N, Yildiz M, Koc B. Elastic properties of coiled carbon nanotube reinforced nanocomposite: A finite element study. *Mater Des*. 2016;109:123-132. [\[CrossRef\]](#)
- Mehrdad Shokrieh M, Mosalmani R, Soveity S. An investigation on effects of aspect ratio of representative volume element on elastic modulus of a carbon nanotubes reinforced polymer. *Modares Mech Eng*. 2014;14(9):107-116.
- Tran BV. A simple model to predict effective conductivity of multicomponent matrix-based composite materials with high volume concentration of particles. *Compos B Eng*. 2019;173:106997. [\[CrossRef\]](#)

14. Lu X, Hu Z. Mechanical property evaluation of single-walled carbon nanotubes by finite element modeling. *Compos B Eng*. 2012;43(4):1902-1913. [\[CrossRef\]](#)
15. Yetgin S, Çolak M. "Grafıt katkılı polipropilen kompozitlerin mekanik ve tribolojik özelliklerinin incelenmesi." *El-Cezeri*. 2020;7(2):649-658.
16. Sever K, Yasar A. The effects of agro-waste reinforcing fillers as single and hybrid on mechanical and thermal properties of polypropylene. *Dokuz Eylül Univ Mühendislik Fak Fen Mühendislik Derg*. 2019; 21(62):395-408.
17. Wu T, Li X, Xu W, Du Y, Xie H, Qu J. Scalable fabrication of high-enthalpy polyethylene/carbon nanotubes/paraffin wax nanocomposite with flexibility and superhydrophobicity for efficient thermal management. *Compos A*. 2022;159:107006. [\[CrossRef\]](#)
18. Bleija M, Platnieks O, Macutkevič J, et al. Poly (butylene succinate) hybrid multi-walled carbon nanotube/iron oxide nanocomposites: electromagnetic shielding and thermal properties. *Polymers*. 2023;15(3):515. [\[CrossRef\]](#)
19. Sadek EM, Ahmed SM, Mansour NA, Abd-El-Messieh SL, El-Komy D. Synthesis, characterization and properties of nanocomposites based on poly (vinyl chloride)/carbon nanotubes–silver nanoparticles. *Bull Mater Sci*. 2023;46(1):30. [\[CrossRef\]](#)
20. Mi D, Zhao Z, Bai H. Improved yield and electrical properties of poly (lactic acid)/carbon nanotube composites by shear and anneal. *Materials (Base)*. 2023;16(11):4012. [\[CrossRef\]](#)
21. Jiang Z, Zhu Z, Zhao M, Chen H, Sue H. Well-dispersed poly (ether-ether-ketone)/multi-walled carbon nanotubes nanocomposite for harsh environment applications. *J Appl Polym Sci* 2022;139(33):e52784. [\[CrossRef\]](#)
22. Shchegolkov AV, Nachtane M, Stanishevskiy YM, Dodina EP, Rejepov DT, Vetcher AA. The effect of multi-walled carbon nanotubes on the heat-release properties of elastic nanocomposites. *J Compos Sci*. 2022;6(11):333. [\[CrossRef\]](#)
23. Ge F-F, Wan N, Tsou C, et al. Thermal properties and hydrophilicity of antibacterial poly (phenylene sulfide) nanocomposites reinforced with zinc oxide-doped multiwall carbon nanotubes. *J Polym Res*. 2022;29(3):29.3, 83. [\[CrossRef\]](#)
24. Mahdavi M, Yousefi E, Baniassadi M, Karimpour M, Baghani M. Effective thermal and mechanical properties of short carbon fiber/natural rubber composites as a function of mechanical loading. *Appl Therm Eng*. 2017;117:8-16. [\[CrossRef\]](#)
25. Yves R, Ahzi S, Baniassadi M, Garmestani H. *Applied RVE Reconstruction and Homogenization of Heterogeneous Materials*. Chichester, UK: John Wiley & Sons; 2016.
26. Mortazavi B, Bardon J, Ahzi S. Interphase effect on the elastic and thermal conductivity response of polymer nanocomposite materials: 3D finite element study. *Comp Mater Sci*. 2013;69:100-106. [\[CrossRef\]](#)

Polyvinyl Alcohol/Titanium dioxide Fibers Prepared Via Electrospinning Methods for Potential Application of Water Treatment

Cik Rohaida Che HAK 

Department of Industrial Technology, Materials Technology Group, Malaysian Nuclear Agency, Selangor, Malaysia

ABSTRACT

Titanium dioxide (TiO₂) is an ideal photocatalyst because of its stability in terms of chemical and optical properties. The performance of TiO₂ as fiber incorporated in a membrane may be better than in bulk form, especially in applications of water treatment. There are many methods for fabrication of TiO₂ in a composite membrane, such as freeze-drying, thermal evaporation, and physical and chemical vapor deposition. Unfortunately, these methods are not favorable because they require multiple steps, which may produce impurities. Electrospinning is a simple and versatile technique to produce a composite membrane comprised of TiO₂. In this study, we propose the fabrication of PVA/TiO₂ composite membrane using the electrospinning method for its potential in water treatment. We studied 2 parameters, which are polymer loading and sonication time, to investigate the quality of the electrospun fibers. Morphology and x-ray diffraction analysis showed that the TiO₂ particles were well incorporated into the PVA fibers. The ability of these electrospun composite fibers to degrade methylene blue dye under UV exposure confirmed that the PVA/TiO₂ fibers can be used in water treatment applications.

Keywords: TiO₂, electrospinning, fiber, photodegradation, membrane

INTRODUCTION

Titanium dioxide (TiO₂) becomes the most promising photocatalyst due to its advantages of being stable as catalyst, reasonably inexpensive, and relatively easy to produce and use.¹ It is human and environmentally friendly and can be used to treat polluted air and split the water to generate hydrogen.² Photocatalysis occurs when nano-TiO₂ is dispersed in an aqueous solution exposed to ultraviolet (UV) light, which causes a hydroxylation reaction that is initiated by hydroxyl radicals (*OH).³⁻⁹ Under UV light illumination, TiO₂ as a catalyst forms an electron hole, whereby holes are positively charged. When this hole is in contact with water molecules, it breaks down into *OH and H⁺ ions. Electrons will react with dissolved oxygen and form O²⁻, which then reacts with water molecules to produce OH⁻ and radical *OOH. The *OOH will combine with H⁺ ions to form *OH and OH⁻, while hole oxidized OH⁻ to form *OH. Hydroxyl radicals are radicals that attack the contaminants that are present in aqueous solution.¹⁰

Most previous studies on the photocatalysis of TiO₂ used a 1-dimensional (1-D) coating on a surface. However, dimension becomes a crucial factor in determining the properties of nanomaterials including surface area.¹¹ The interest of Electrospinning (ES) in fabricating ceramic nanofibers has grown exponentially since 2002.¹² and recently, it has become a popular technique to produce 2-D composite materials. This technology uses electric field to convert polymer solution (matrix) or melt it into a fiber form. The principle of ES is a syringe loaded with a polymer solution that is pumped at a constant flow rate. A specific voltage applied will induce an electric field between the needle tip and the collector. The solution will be charged, and the charge will accumulate at the surface of the liquid. As the voltage increases, the electrostatic repulsion of the solution will increase. The liquid is retained by surface tension. When the electrostatic repulsion is higher than the surface tension, a liquid meniscus with a conical shape is formed at the tip of the needle. The electric field and surface tension of the solution interact with each other, leading to stretching in the solution jet, which allows fibers to be formed. The whipping motion of the jets leads to the evaporation of the solvent and solidifies the fiber.¹³

In general, the quality of the electrospun fibers depends on 3 processing parameters: the ES experiment setup (voltage supply, flow rate, needle size, and needle tip-to-collector distance), sol-gel parameters, and the selection of precursors. The viscosity of the ES solution depends on the molecular



Received: 29.10.2023

Accepted: 29.11.2023

Publication Date: 31.12.2023

Corresponding author:

Cik Rohaida Che HAK

Email: rohaida@nm.gov.my

Cite this article as: Hak CRC. PVA/TiO₂ fibers prepared via electrospinning methods for potential application of water treatment. *NanoEra* 2023;3(2):34-39.



Content of this journal is licensed under a Creative Commons Attribution-NonCommercial-NoDerivatives 4.0 International License.

weight of the polymer and the concentration of the mixture (polymer, solvent, and precursor). The polymer concentration will determine the fiber diameter,¹⁴ and the diameter increases with the increase of TiO₂ precursor solution.¹⁵ The advantage of ES is that it can produce nanofibers with diameters ranging from 50 to 500 nm. These small-size fibers improved the photocatalytic performance of nanomaterials. By using the ES technique, the mechanical, biological, and kinetic properties of electrospun fibers are easily manipulated by altering the matrix composition and processing parameters.¹⁶

Commonly, the electrospinning method is combine with sol-gel technique to synthesize the nanoparticles. The usual precursor used for TiO₂ was titanium isopropoxide (TIP), the matrix used was polyvinylpyrrolidone (PVP) due to its high molecular weight (130,000 g/mol), and the solvent used to dissolve PVP was ethanol. The anatase phase of TiO₂ was obtained by calcination of the fibers.

In our study, we introduced a new method to produce fibers using ES by avoiding the sol-gel and calcination process. We used TiO₂ powder that was synthesized earlier via hydrothermal method, and it was calcined to obtain the anatase phase. These nanoparticles were then incorporated into polyvinyl alcohol (PVA) as the matrix.

Literature Review

The use of electrospun TiO₂ fibers has become an interest in various applications, such as energy storage, health-care, biotechnology, environmental engineering, defense, and security.¹⁷ Specifically for environmental engineering applications, the nanofibers require high porosity meshes, microscale interstitial space, large high surface area-to-volume ratio, and flexibility of structures, and mechanical performance, which enable them to be an excellent material for membrane fabrication.^{17,18} Nowadays, the use of electrospun TiO₂ has become an interest for various applications as the nanofibers have significantly improved photocatalytic performance due to the small fibers. This has led to quick charge transfer to the dynamics of electron-hole recombination on a large specific surface area of TiO₂ nanofibers.¹⁹ Alves et al²⁰ reported that the photocatalytic activity of TIP/PVP electrospun fibers was reduced due to the increase of heating temperature during calcination that resulted in decrease in fraction of anatase phase and surface area of the fibers. The photo-oxidative decomposition of methylene blue (MB) was compared to TiO₂ powder Degussa P-25. Li et al¹⁵ have developed the ES technique without combining with sol-gel by using tetrabutyltitanate as the precursor, PVP as the matrix, and ethanol as the solvent. Mesoporous TiO₂ nanofibers with anatase were successfully produced after calcination at 500°C. This PVP/TiO₂ showed that the photodegradation rate of rhodamine B in aqueous solution was 99% under UV light. Hong et al²¹ reported the removal of 99% acetone and 90% of particulate with size larger than 200 nm under UV irradiation (254 nm) by a non-woven membrane of PVA/TiO₂ (Degussa P25) prepared using electrospinning. There are many previous studies report on the technique to enhance the photocatalysis of electrospun TiO₂ fiber. Jeun et al²² use electron beam irradiation on (PAN)/TiO₂ electrospun fibers to show an increase of about 24% in the photodegradation of MB. Mishra et al²³ studied the PVP/TiO₂ electrospun nanofibers functionalized with silver (Ag) nanoparticles to enhance the electronic and catalytic properties of TiO₂. Photocatalytic reaction using methyl red under UV light showed that the PVP/TiO₂/Ag composite degraded 30% of methyl red compared to 24% degradation for pure TiO₂ in a span of 265 minutes.

MATERIAL AND METHODS

Titanium dioxide powder was synthesized using hydrothermal method and was sintered at high temperature to obtain the anatase phase. For preparing the electrospinning solution, the deionized water was used as dispersant, polyvinyl alcohol (PVA) as the media for the fibers, a surfactant to stabilize the nanoparticles in the solution, and MB dye for photodegradation experiment.

Experimental

The fabrication of PVA/TiO₂ fibers using the ES technique was reported in 2021.²⁴ In this study the fabrication methods for PVA/TiO₂ fibers are similar to the one reported in 2021. However, in the current study, we focus on the optimization of the fabrication parameters: the first parameter is to vary the amount of PVA from 10-16 wt% and the second parameter is sonication time which was altered from 1-4 hours. The ratio of the PVA : TiO₂ mixture was 4 : 1, and the TiO₂ : SDS mixture was 10 : 1. The morphology of the electrospun fibers was characterized using field emission scanning electron microscope (GeminiSEM 500, Carl Zeiss) and the titanium (Ti) element was determined using energy-dispersive x-ray (X-Max 80, Oxford Instrument). The anatase phase was determined using an x-ray diffractometer (X'Pert Pro, Panalytical). The electrospun fibers were then removed from the aluminum foil and immersed in MB dye solution for photodegradation

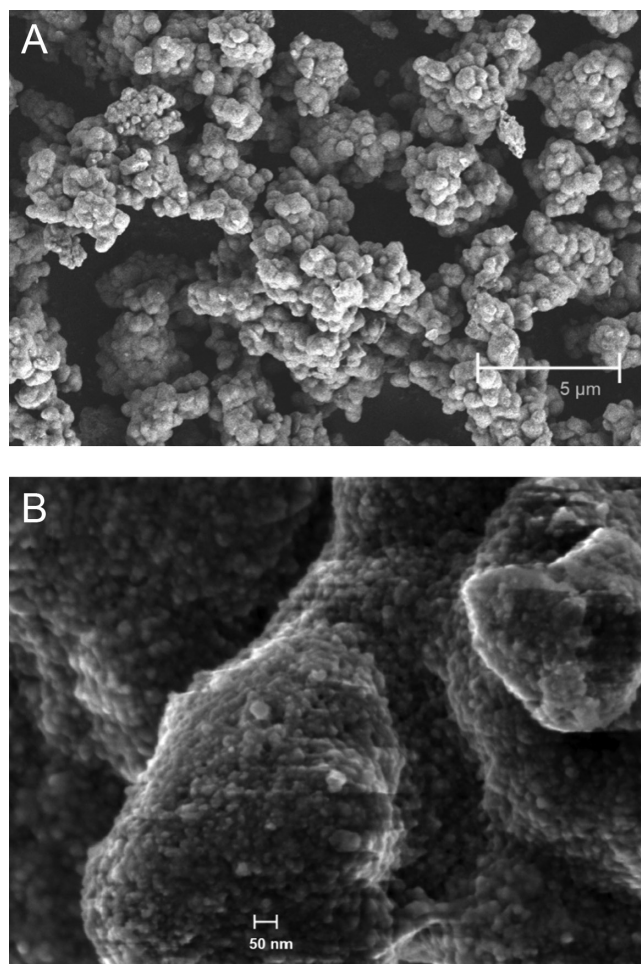


Figure 1. Electron images of titanium dioxide particles observed using field emission scanning electron microscopy at magnification of (A) 25 kx, and (B) 70 kx.

experiment using 400W UV light for 5 hours of exposure time. The degradation was determined based on the absorbance value at an interval of 1 hour obtained using a ultraviolet-visible spectrometer (Lambda 35, Perkin Elmer).

RESULTS AND DISCUSSION

The TiO₂ powder used in this study was characterized earlier using field emission scanning electron microscopy and x-ray diffraction analysis (XRD). Figure 1 shows the electron images for TiO₂ particles at 2 different magnifications. It was observed that at 25 kx magnification, the particles are heavily agglomerated. However, at 75 kx, the particles were observed as spherical and homogeneous, and the size was able to be determined at less than 50 nm.

The TiO₂ powder used in this study was characterized using XRD analysis. Figure 2A shows that the peaks are identified at $2\theta = 25.8^\circ$, 38.15° , 48.53° , and 55.13° , which are identified as the anatase phase (ICSD: 01-070-6826). The differences between XRD spectra were compared to characterize the crystalline structure of PVA

and PVA/TiO₂ fibers, as shown in Figure 2B. It is found that there are 2 peaks that only appear on the PVA/TiO₂ spectrum at $2\theta = 17^\circ$ and 19° , indicating that the crystallinity of PVA fibers was affected by the presence of TiO₂ nanoparticles. The same results were also reported previously by Khan et al.²⁵ The broad peak at $2\theta = 25.8^\circ$ is only observed on the pristine PVA fibers, which indicates that texturization occurred during the electrospinning process.²⁶ Texturization is a mechanism by which PVA changes its crystal structure to a preferred orientation to accommodate the presence of TiO₂ and surfactant during the electrospinning process.²⁷

The XRD spectrum for PVA/TiO₂ fibers was further refined to determine the association of TiO₂ with the fiber, as shown in Figure 2C. It confirms that TiO₂ was associated with the fibers at $2\theta = 9.33^\circ$, 13.23° , 17.16° , 19.31° , 21.86° , 24.51° , and 25.69° . These peaks are defined as anatase TiO₂ (ICSD: 98-009-4635). Furthermore, the degree of crystallinity determined by the under-the-curve measurement shows that PVA/TiO₂ fiber has a higher crystallinity (75.21%) compared to pristine PVA fiber (27.7%). The

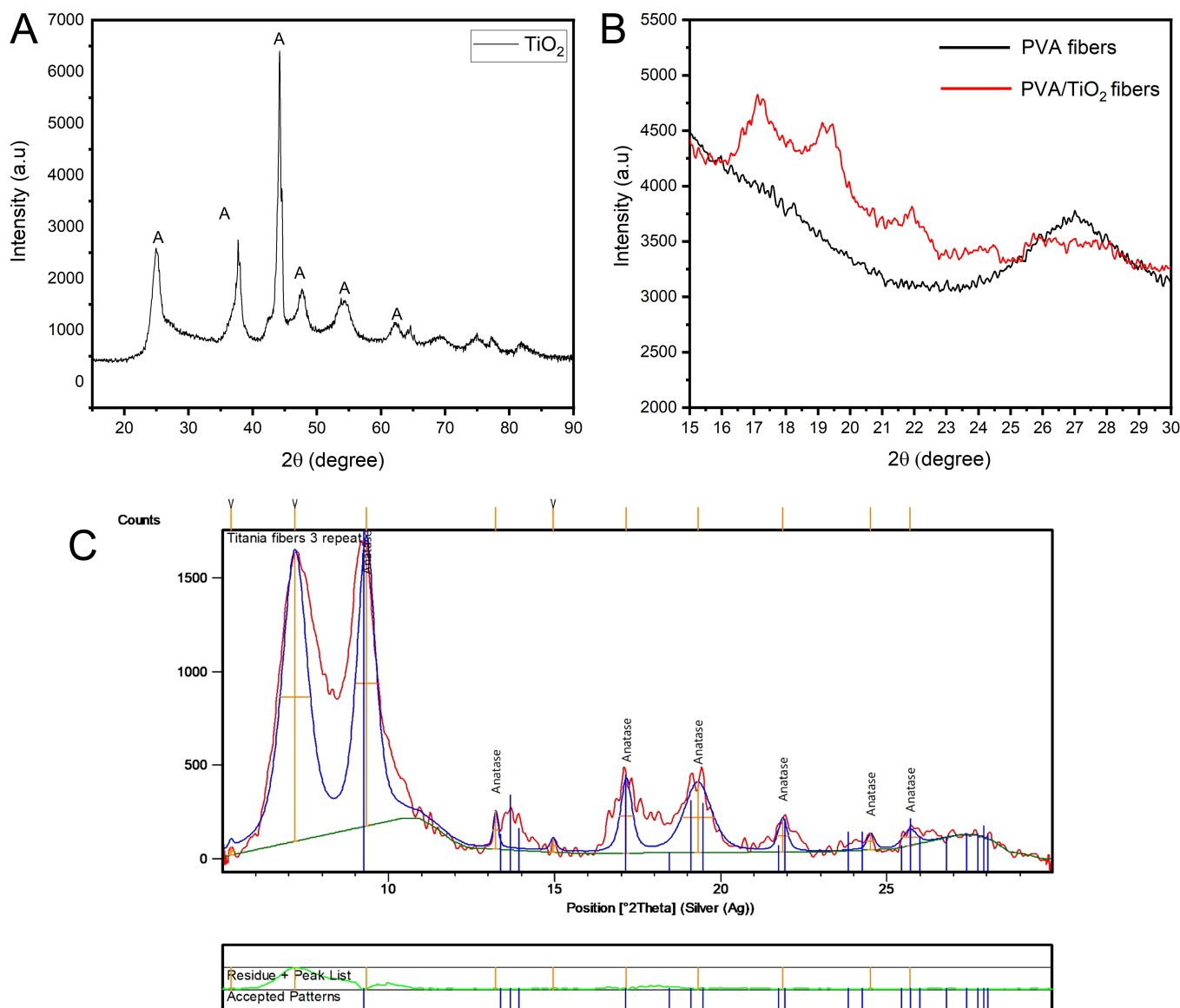


Figure 2. X-ray diffraction analysis spectra of (A) titanium dioxide (TiO₂) powder, (B) pristine polyvinyl alcohol (PVA) and PVA/TiO₂ fibers, and (C) PVA/TiO₂ fibers indicate refined peaks for anatase identification and area under curve measurement for degree of crystallinity.

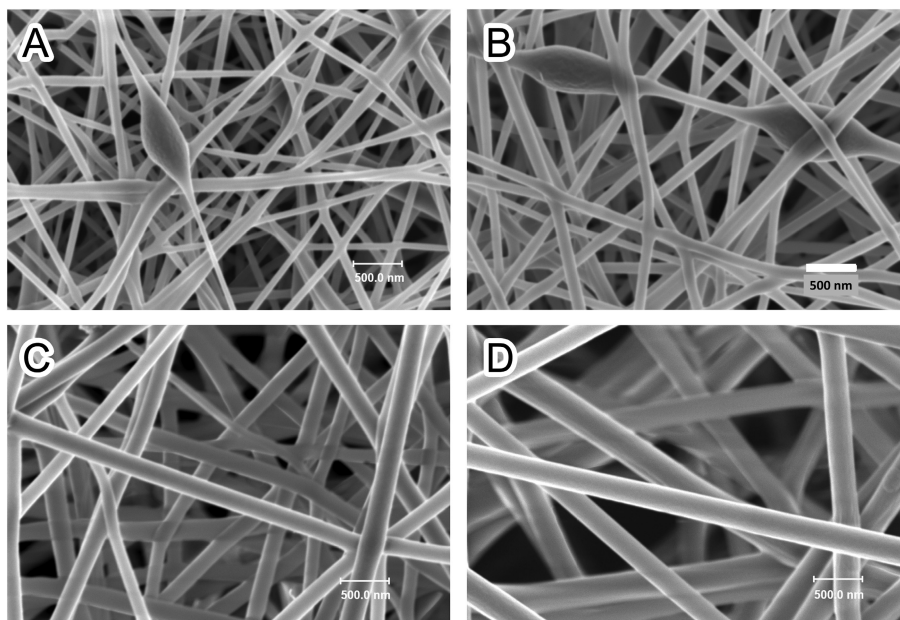


Figure 3. Electron images of polyvinyl alcohol (PVA)/titanium dioxide electrospun fibers with increasing PVA loading from (A) 10 wt%, (B) 12 wt%, (C) 14 wt%, and (D) 16 wt% observed at 25 k \times magnification.

incorporation of TiO₂ into PVA interfered with the polymer chain through the steric effect and hydrogen bonding between PVA and TiO₂ nanoparticles (NPs). The hydroxyl group became more

terminally extended, which made the crystalline structure rigid, resulting in reduced crystallinity of the pristine PVA fiber.²⁸

Figure 3 shows the electron images of PVA/TiO₂ fibers with different amount of PVA added. It is observed that as the wt% of PVA increases from 10 to 16 wt%, the fiber diameter also increases, and the spherical shape beads were formed at low wt%. This is related to the viscosity of the polymer solution. This is supported by the previous studies which showed the number of beads decreases as the viscosity increased.²⁹

The fiber diameter of fibers prepared at 16 wt% in Figure 3 was measured and found that the size increases with sonication time.

Table 1. The Diameter of Polyvinyl Alcohol/Titanium Dioxide Fibers as a Function of Sonication Time

Sonication Time (hours)	Fiber Diameter (nm)
1	222
2	228
3	393
4	795

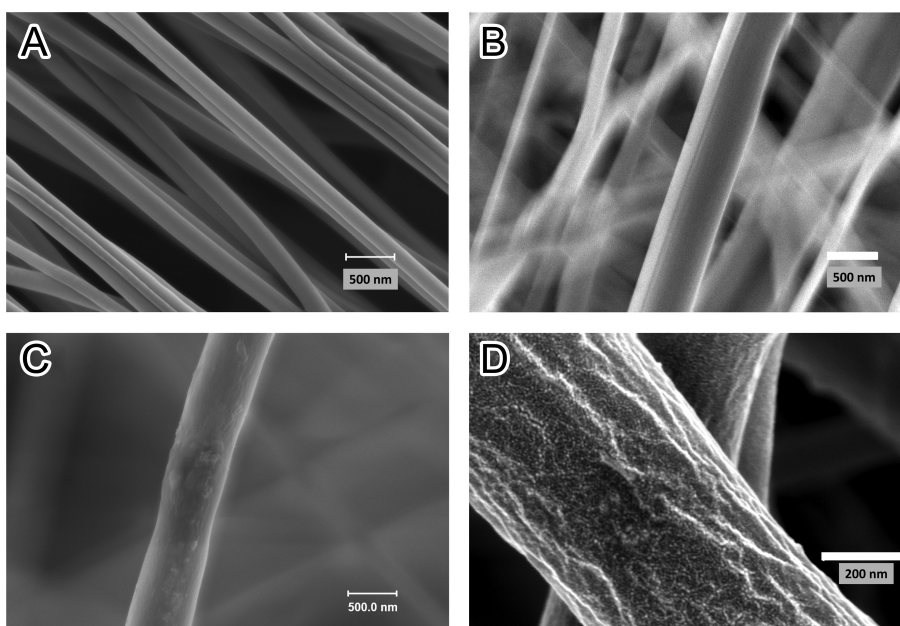


Figure 4. Electron images of fibers prepared at different sonication time; (A) pristine polyvinyl alcohol (PVA) fibers sonicated for 2 hours; (B) PVA/titanium dioxide (TiO₂) fibers sonicated for 2 hours; (C) PVA/TiO₂ fibers sonicated for 4 hours; and (D) PVA/TiO₂ fibers sonicated for 4 hours and magnified at 100 k \times . Magnification for (A)–(C) is 25 k \times .

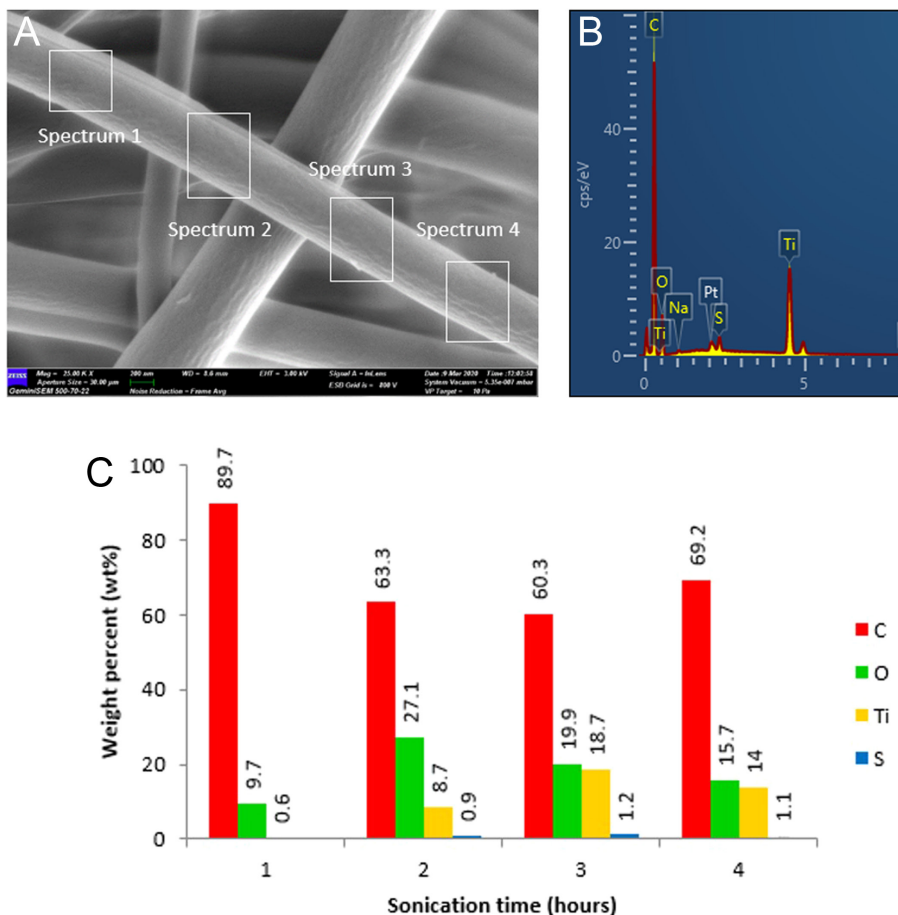


Figure 5. The field emission scanning electron microscopy/energy dispersive X-ray (EDX) elemental analysis of (A) 4 different spots on the polyvinyl alcohol/titanium dioxide fibers to detect the presence of titanium (Ti). (B) EDX spectrum indicates the presence of Ti and (C) the concentration of Ti (wt%) at different sonication times. C, carbon; O, oxygen; S, sulfur.

The diameter increases from 222 nm when sonicated at 1 hour and increases to 795 nm after 4 hours as shown in Table 1.

Sonication time is important to reduce the particle size of titania aggregates as smaller aggregates promote better incorporation of titania particles with PVA and thus form fibers with a larger diameter. Figure 4 shows that fibers produced with 4 hours of sonication time have a rougher surface, attributed to the titania aggregates appearing on the surface of the fibers as compared to fibers produced with 2 hours of sonication time and PVA-pristine fibers. The distribution of TiO₂ particles on the fibers' surface can be seen clearly at a magnification of 100 kx.

Figure 5A shows the FESEM/EDX elemental analysis measured at 4 different spots on the PVA/TiO₂ fibers' surface. Figure 5B shows the presence of titanium (Ti) element besides carbon (C), oxygen (O), and sulfur (S). The existence of Ti and O on the fibers' surface confirmed that TiO₂ nanoparticles are distributed on the fiber surfaces, while sulfur is attributed to the surfactant. The concentration (wt%) of Ti was measured as a function of different sonication times. It is found that the wt% of Ti increases with the increasing sonication time, as shown in the graph in Figure 5C.

The distribution of TiO₂ on the fiber is crucial, as it can affect the efficiency of the catalyst when used in wastewater treatment application. To study the catalysis effect of PVA/TiO₂ fibers, photodegradation is calculated from the UV-Vis absorbance measurement. The percentage of MB degraded in the solution is 60.5%

for pristine PVA fibers and 75.7% for PVA/TiO₂ fibers. The rate of photodegradation is calculated as 0.081/min and 0.127/min for pristine PVA and PVA/TiO₂ fibers, respectively.

The fabrication process of PVA/TiO₂ fibers using the ES method was successfully developed. The amount of PVA required to give the best fibers with the least numbers of beads was 16 wt%. The appropriate sonication time, which led to a homogenous distribution of TiO₂ particles on the fibers' surface, was 4 hours. X-ray diffraction confirmed the existence of Ti on the polymer fiber surface. This study proved that the PVA/TiO₂ fibers were able to degrade MB under UV exposure, and the presence of anatase TiO₂ loaded onto the fibers had increased the photodegradation rate.

Peer-review: Externally peer-reviewed.

Acknowledgements: I would like to thank the Malaysian Nuclear Agency for giving me permission to carry out this research, to my student Nur Syaifeika from Universiti Putra Malaysia for all the experimental works, and to my colleagues Siti Aisyah Ahmad Fuzi and Nur Ubaidah Saidin for assisting me in XRD analysis.



Declaration of Interests: The author declares that they have no competing interest.

Funding: The author declared that this study has received no financial support.

REFERENCES

- Albetran H, Dong Y, Low IM. Characterization, and optimization of electrospun TiO₂/PVP nanofibers using Taguchi design of experiment method. *Journal of Asian Ceramic Societies*. 2015;3(3):292-300. [\[CrossRef\]](#)
- Hanaor DAH, Sorrell CC. Review of the anatase to rutile phase transformation. *J Mater Sci*. 2011;46(4):855-874. [\[CrossRef\]](#)
- Medana C, Calza P, Dal Bello F, Raso E, Minero C, Baiocchi C. Multiple unknown degradants generated from the insect repellent deet by photoinduced processes on TiO₂. *J Mass Spectrom*. 2011;46(1):24-40. [\[CrossRef\]](#)
- Sirtori C, Zapata A, Malato S, Gernjak W, Fernández-Alba AR, Agüera A. Solar photocatalytic treatment of quinolones: intermediates and toxicity evaluation. *Photochem Photobiol Sci*. 2009;8(5):644-651. [\[CrossRef\]](#)
- Lopez-Alvarez B, Torres-Palma RA, Peñuela G. Solar photocatalytic treatment of carbofuran at lab and pilot scale: effect of classical parameters, evaluation of the toxicity and analysis of organic by-products. *J Hazard Mater*. 2011;191(1-3):196-203. [\[CrossRef\]](#)
- Lu CS, Chen CC, Mai FD, Li HK. Identification of the degradation pathways of alkanolamines with TiO₂ photocatalysis. *J Hazard Mater*. 2009;165(1-3):306-316. [\[CrossRef\]](#)
- Stapleton DR, Konstantinou IK, Mantzavinos D, Hela D, Papadaki M. On the kinetics and mechanisms of photolytic/TiO₂-photocatalytic degradation of substituted pyridines in aqueous solutions. *Appl Cat B*. 2010;95(1-2):100-109. [\[CrossRef\]](#)
- An TC, An JB, Yang H, Li G, Feng H, Nie X. Photocatalytic degradation kinetics and mechanism of antiviral drug-lamivudine in TiO₂ dispersion. *J Hazard Mater*. 2011;197:229-236. [\[CrossRef\]](#)
- Lin Y, Ferronato C, Deng N, Wu F, Chovelon J. Photocatalytic degradation of methylparaben by TiO₂: multivariable experimental design and mechanism. *Appl Cat B*. 2009;88(1-2):32-41. [\[CrossRef\]](#)
- Lazar M, Varghese S, Nair S. Photocatalytic water treatment by titanium dioxide: recent updates. *Catalysts*. 2012;2(4):572-601. [\[CrossRef\]](#)
- Madhugiri S, Sun B, Smirniotis PG, Ferraris JP, Balkus KJ. Electrospun mesoporous titanium dioxide fibers. *Micropor Mesopor Mater*. 2004;69(1-2):77-83. [\[CrossRef\]](#)
- Chronakis IS. Novel nanocomposites and nanoceramics based on polymer nanofibers using elec-trospinning process-A review. *J Mater Process Technol*. 2005;167(2-3):283-293. [\[CrossRef\]](#)
- Bera B. Literature review on electrospinning process (A fascinating fiber fabrication technique). *Imperial J Interdiscip Res*. 2016;8(2):972.
- Fridrikh SV, Yu JH, Brenner MP, Rutledge GC. Controlling the fiber diameter during electrospinning. *Phys Rev Lett*. 2003;90(14):144502. [\[CrossRef\]](#)
- Li Q, Satur DJG, Kim H, Kim HG. Preparation of sol-gel modified electrospun TiO₂ nanofibers for improved photocatalytic decomposition of ethylene. *Mater Lett*. 2012;76:169-172. [\[CrossRef\]](#)
- Guarino V, Cruz M, Iriczalili A, et al. Electrospun polycaprolactone nanofibers decorated by drug loaded chitosan nanoparticles reservoirs for antibacterial treatments. *Nanotechnology*. 2017;28.
- Ramakrishna S, Fujihara K, Teo W, Yong T, Ma Z, Ramaseshan R. Electrospun nanofibers: solving global issues. *Mater Today*. 2006;9(3):40-50. [\[CrossRef\]](#)
- Ramaseshan R, Sundarrajan S, Jose R, Ramakrishna S. Nanostructured ceramics by electrospinning. *J Appl Phys*. 2007;102(11):111101. [\[CrossRef\]](#)
- Wu H, Pan W, Lin D, Li H. Electrospinning of ceramic nanofibers: fabrication, assembly, and applications. *J Adv Ceram*. 2012;1(1):2-23. [\[CrossRef\]](#)
- Alves AK, Berutti FA, Clemens FJ, Graule T, Bergmann CP. Photocatalytic activity of titania fibers obtained by electrospinning. *Mater Res Bull*. 2009;44(2):312-317. [\[CrossRef\]](#)
- Chuang Y, Hong G, Chang C. Study on particulate and volatile organic compounds removal with TiO₂ non-woven filler prepared by electrospinning. *J Air Waste Manag Assoc*. 2014;64(6):738-742. [\[CrossRef\]](#)
- Jeun JP, Park DW, Seo DK, et al. Enhancement of photocatalytic activity of PAN-Based nanofibers containing sol-gel derived TiO₂ nanoparticles by e-beam irradiation. *Rev Adv Mater Sci*. 2011;28:26.
- Mishra S, Ahrenkiel P, Shankar R, Whites KW. Synthesis and characterization of electrospun TiO₂/Ag composite nanofibers for photocatalysis applications. *Microsc Microanal*. 2011;17(S2)(suppl 2):1710-1711. [\[CrossRef\]](#)
- Cik Rohaida CH, Syafeika R, Siti SZA, Nur Ubaidah S, Siti AAF. Effect of electron irradiation to the photocatalytic activity of the titanium oxide fibers. *IOP Conf S Mater Sci Eng*. 2020;1106012016.
- Khan MQ, Kharaghani D, Ullah S, et al. Self-cleaning properties of electrospun PVA/TiO₂ and PVA/ZnO nanofibers composites. *Nanomaterials (Basel)*. 2018;8(9):644. [\[CrossRef\]](#)
- Costa RGF, Ribeiro C, Mattoso LHC. Morphological and photocatalytic properties of PVA/TiO₂ nanocomposite fibers produced by electrospinning. *J Nanosci Nanotechnol*. 2010;10(8):5144-5152. [\[CrossRef\]](#)
- Ojha S. Structure-property relationship of electrospun fibers. In *Electrospun Nanofibers* Afshari M., ed. 2017:239.
- Sakarkar S, Muthukumaran S, Jegatheesan V. Evaluation of polyvinyl alcohol (PVA) loading in the PVA/titanium dioxide (TiO₂) thin film coating on polyvinylidene fluoride (PVDF) membrane for the removal of textile dyes. *Chemosphere*. 2020;257:127144. [\[CrossRef\]](#)
- Al-Hazem NZ. Nanofibers and electrospinning method. In: Kyzas G. K., Mitropoulos A. C., eds. *Novel Nanomaterials - Synthesis and Applications*. 1st ed. London: IntechOpen; 2018:116.

Experimental Investigation of Conical Spring Inserts on In-Tube Heat Transfer and Pressure Drop

Muhammet Kaan
YEŞİLYURT¹
Ömer ÇOMAKLI²

¹Department of Machine and Metal Technologies, Atatürk University, Vocational School of Technical Sciences, Erzurum, Turkey

²Department of Mechanical Engineering, Atatürk University, Faculty of Engineering, Erzurum, Turkey

ABSTRACT

Two-phase flow is preferred in many industrial applications where high heat flux is present and/or required because of its higher heat transfer coefficient compared to single-phase flows. However, there are some adverse effects that will reduce the life of the system and its components, as well as risk the safe operation and its benefits. In this study, the effects of conical coiled springs as an in-tube element aimed at the elimination, or actually minimization, of said adverse effects are investigated experimentally. In this study, a 2-phase flow system was used, with the test section comprised of a straight horizontal tube with forced convection boiling. The effects of equally spaced conical spring arrays having different pitches as an in-tube heat transfer enhancement element on heat transfer and pressure drop in 2-phase flow were investigated. Fluid supply flow rate and pitches of conical springs inserted into the tube were selected as study parameters, and experiments were made under constant operating pressure, constant inlet temperature, constant heat input, and fixed outlet restrictions to investigate the effects of conical springs. Four different heat transfer surface configurations are used. Experiments showed that the minimum point shifted to the right on the curve with the increase in heat input, and the mass flow rate at a given pressure drop observed is directly proportional to the thermal power. The highest pressure drop in the 2-phase flow region is observed with tube 4 (10 mm pitch) and tube 3 (20 mm pitch), while the lowest pressure drop is with tube 1.

Keywords: Conical spring insert, heat transfer, pressure drop, 2-phase flow

INTRODUCTION

Nuclear reactors, cooling systems, steam generators, processing facilities, and similar industrial operations commonly involve 2-phase flows.¹ These flows occur in various natural phenomena, from the formation of raindrops within clouds to the behavior of water during ice formation. The higher heat transfer coefficients of 2-phase flows compared to single-phase flows, coupled with the increasing industrial demand for high heat flux applications, have led to a rapid growth in interest and research in this field.

In many industrial systems where heat transfer occurs through boiling, flow instabilities due to fluctuations in system pressure and fluid flow can result in disruptions and failures, significantly reducing the economic lifespan of these systems. These flow instabilities can lead to issues such as thermal fatigue, boiling crises, mechanical vibrations, difficulty in control due to high transient temperatures, and burn-out events on the heat transfer surfaces.²

The economic design, optimization, and safe operation of these systems are directly linked to their ability to predict the thermal characteristics and hydrodynamic instabilities of 2-phase flows. Two-phase flows involve the formation of interfaces between phases, and the shapes these interfaces take are fundamental in defining the characteristics of the 2-phase flow. The flow direction significantly influences the shapes of these interfaces, categorizing 2-phase flows into inclined, vertical, and horizontal based on flow direction. Each of these flow directions exhibits distinct flow regimes and characteristics. The influence of gravity, according to the flow direction, leads to a fundamental categorization, with horizontal flow systems experiencing phase separation due to the perpendicular effect of gravity. In these systems, lower-density vapor is found in the upper portion of the tube, and higher-density liquid is in the lower section. The lower heat transfer coefficient in the vapor phase compared to the liquid phase in the carrying systems results in the occurrence of a phenomenon known as “burn-out” in the upper regions.³

Received: 02.11.2023

Accepted: 04.12.2023

Publication Date: 31.12.2023

Corresponding author:
Muhammet Kaan YEŞİLYURT
E-mail: kaan.yesilyurt@atauni.edu.tr

Cite this article as: Yeşilyurt MK, Çomaklı Ö. Experimental investigation of conical spring inserts on in-tube heat transfer and pressure drop. *NanoEra* 2023;3(2):40-52.



Content of this journal is licensed under a Creative Commons Attribution-NonCommercial-NoDerivatives 4.0 International License.

Naturally, the effect of gravity on flow systems in vertical and inclined flows results in fewer variations in the shapes of the interfaces compared to horizontal flows. Hence, the factors influencing flow regimes are the absolute and relative flow rates of the 2 phases, system geometry, and the forces acting on each phase. Two types of instability are identified in 2-phase flow systems: “static” and “dynamic.” “Static instabilities” refer to a situation where a small change in flow conditions in a stable state leads to an asymptotic shift in the working regime, illustrated by phenomena such as boiling crises and flow excursions. “Dynamic instabilities” occur when the process is significantly influenced by inertia and other feedback effects. These instabilities happen because the flow’s inertia and the 2-phase mixture’s ability to be compressed do not interact well enough. There are also many feedback loops that involve changes in flow rate, pressure drop, and density in the channel where boiling happens. Dynamic instabilities are classified into 4 main categories: (i) pressure drop oscillations (PDO), (ii) thermal oscillations in tubes causing thermal fatigue due to significant temperature changes on the tube wall, (iii) density-wave oscillations, which have amplitudes smaller than pressure drop oscillations and equal to the transit time of the fluid, and (iv) high-frequency acoustic oscillations.^{4,5}

In an effort to enhance heat transfer, options are using active systems, which require external power sources, and passive systems, which leverage geometric changes, arrangements, or modifications (e.g., treated surfaces, rough surfaces, swirling flow devices) without external power.⁶ One commonly explored approach is manipulating the flow regime within the system to improve heat transfer. Enhanced heat transfer, in turn, boosts the operational efficiency of these systems, leading to the development of more compact systems, reduced installation space requirements,⁷ decreased initial costs, and shorter payback periods.

Methods for manipulating the flow regime and enhancing heat transfer characteristics vary depending on the system and its structural design. These methods encompass inserting devices within tubes or channels and attaching components at the inlet, outlet, or along the flow path. Studies typically employ numerical and experimental methods, often using a circular single tube as the test section with an insert (such as a swirl/vortex generator or turbulator) to induce turbulent flow.^{8–16}

A review of the literature on 2-phase flow systems reveals numerous studies that have investigated heat transfer improvement using inserts, turbulators, and swirl/vortex generators. These turbulators can take various forms, including blades,¹⁷ rods,^{18,19} rings,^{20,21} tapes,^{13,22} strips,^{13,23} or coils.^{24,25} These turbulators enhance heat transfer by promoting flow mixing, resulting in turbulent flow induced by longitudinal vortices. Several parameters impact the enhancement rate achieved by turbulators, including their shape, geometry, placement, spacing or pitch, flow attack angle, material, effective diameter, Reynolds number, and additional modifications such as perforations or wings.²⁶

In the early 20th century, alongside the industrial revolution and the rapid development of industrial applications, research on 2-phase flows and their related issues significantly increased. Since Lorentz’s pioneering experimental investigation of the hydrodynamics of 2-phase flows in 1909, numerous studies have been conducted in this field.

Among these studies, Ledinegg’s 1938 research on flow instabilities in heated parallel steam generator channels, later known

as “Ledinegg instability,” is of particular importance. Ledinegg observed that the characteristic curve of the flow, which should always have a positive slope in single-phase flow, exhibited negative slopes in certain flow rate ranges. This observation indicated that there was not a single flow rate corresponding to a single pressure drop, leading to the system transitioning between stable states.

In 1956, Davidov²⁷ conducted experimental research by providing heat flux to test tubes using electrical power, examining oscillations. He observed that the periods of these oscillations were almost equal to the transit time of the fluid in the test tube. The research also revealed that extending the portion exposed to excessive cooling and connecting the channels increased system stability, while using restrictive elements at the outlet of the test tube reduced stability.

Stenning and Veziroğlu,²⁸ using R-11 as the working fluid, identified and defined 3 different types of dynamic instabilities in their experimental study. These included “density change oscillations” resulting from the movement of high- and low-density fluid waves along the heated channel, “pressure drop oscillations” causing large-amplitude oscillations in pressure, wall temperature, and fluid flow rate, and “thermal oscillations” related to the instability of the liquid film layer on the channel wall. The research also indicated that the presence of a compressible volume in front of the test section was necessary for pressure drop oscillations to occur. Then, Veziroğlu and Lee^{29–31} compared their experimental results on pressure drop and density change oscillations with earlier research on horizontal channels using R-11 in a vertical upflow system. They found that vertical upflow systems were more stable than horizontal flow systems.

Aritomi et al^{32–34} developed a nonlinear mathematical model for flow instability based on experimental work in a vertically upward parallel channel system with forced convection, boiling, and water as the working fluid. The model was compared to experimental data from a 2-parallel channel system and was found to be in good agreement. The model was later applied to systems with 3 and 4 parallel channels. Aritomi et al³³ also examined density change oscillations and the effects of slip ratio on stability in parallel boiling systems using both experimental and a new, more complex analytical model. They explored the factors influencing oscillations and the movement of the boiling boundary in low heat flux and high inlet subcooling conditions.

Kakac et al³⁵ did experiments and used a homogeneous 2-phase flow model to figure out how to measure thermal oscillations in an R11-based vertically upward single forced-convection channel test system. They investigated the effects of fluid inlet temperature, heat power, and heating tube dimensions on thermal oscillations. They observed density change, pressure drop, and thermal oscillations. The applied model involved one-dimensional flow equations and expressed the conditions for the emergence of thermal oscillations. The theoretical results were consistent with experimental findings in terms of oscillations, amplitudes, and period values. Thermal oscillations were observed parallel to pressure drop oscillations, but the maximum values of pressure drop oscillations shifted away from the maximum values of thermal oscillations with a phase lag.

Padki et al³⁶ developed a new integral formulation based on dynamic system theory and derived pressure drop, Ledinegg instability’s stability criteria, and mass flow characteristics from

the negative slope of the pressure drop stability region. Differences between pressure drop and Ledinegg instability reflected bifurcation-type differences.

Ding et al³⁷ observed that the amplitude of inlet pressure oscillations in a horizontal boiling tube system decreased as the mass flow rate decreased. It increased as the inlet temperature value rose or the inlet subcooling degree decreased. The periods were directly proportional to the mass flow rate and inlet subcooling degree. Density change oscillations were observed in the negative slope region, and thermal oscillations always accompanied pressure drop oscillations and were observed on the upper side of the tube wall.

Xiao et al³⁸ found that density change oscillations were more pronounced in high-pressure parallel channel systems than in single channels, both in their analytical model and experimental investigation.

Liu et al^{39,40} experimentally examined flow transition boiling, thermal oscillations, and hydrodynamic instabilities in a vertically oriented, boiling, forced-convection, vertical tube test system using R-12 as the working fluid. They observed 2 distinct oscillation models in the boiling zones of flow transition, one with high frequency and low amplitude and the other with low frequency and high amplitude. They identified the low-frequency model parameters, which included heated wall capacity, axial heat conduction gradient, and boiling characteristics.

Guo et al⁴¹ examined how 2-phase flow, pressure drop oscillations, and their boundaries affected transient heat transfer in a spiral tube with 2-phase steam–water flow. They conducted experiments using unsaturated water flow and 2-phase steam–water flow to investigate local heat transfer with non-uniform features. The study analyzed the effects of secondary flow, flow oscillations, and their interactions. Peripheral time-averaged Nusselt numbers were significantly different between local and vibrating flow. The study also discussed pressure drop oscillations and their boundaries for steam–water 2-phase flow in a spirally heated tube. The effects of parameters such as friction, heating conditions, and other variables on the pressure drop oscillations were investigated.

Çomaklı et al⁴² studied 2-phase flow instabilities in a horizontal boiling straight tube system with a fixed system pressure and constant heat flux. They observed that dynamic instabilities of all types occurred at all temperature values. The stability boundaries shifted toward lower mass flow rates as the inlet temperature decreased, indicating that system instability increased with increasing inlet temperature. The periods of pressure drop and density change oscillations changed directly with the mass flow rate and inversely with the inlet temperature value. The study emphasized the importance of channel length as a significant parameter concerning dynamic 2-phase flow instabilities.

Yu et al⁴³ investigated 2-phase pressure drop, boiling heat transfer, and critical heat flux in a horizontal tube system with a length of 0.91 m and an inner diameter of 2.98 mm. They successfully related the results of pressure drop and heat transfer coefficient to changes in existing correlations for both small channels with cooling fluids and larger channels with water. In smaller channels, the pressure drop in 2-phase flow was observed to be lower than expected for the same mass flow rates. A comparison was made with the Chisholm correlation, and differences were attributed to differences in 2-phase flow regimes between channel

sizes. The Chisholm correlation for smaller channels was modified to improve prediction accuracy, and it was observed that the heat power significantly affected boiling heat transfer in small channels.

Salman et al⁴⁴ conducted a numerical study comparing the heat transfer and friction factors of V-cut twisted tape inserts with classical twisted tape inserts at various twist ratios. They found that the heat transfer enhancement was positively related to the Reynolds number and inversely related to the twist ratio. V-cut twisted tape inserts with a twist ratio of 2.93 and a cut depth of 0.5 cm achieved the highest heat transfer rate. V-cut twisted tape inserts also offered better heat transfer performance compared to right-left helical tape inserts, resulting in an overall maximum heat transfer enhancement of 107%. Alam et al.⁴⁵ presented a comprehensive literature review of turbulators in air ducts, highlighting that perforations in ribs, chambers, and blocks, as well as a combination of rib and delta fins, demonstrated improved thermo-hydraulic performance in solar air heaters and heat exchangers.

Razzaghi et al.⁴⁶ studied heat transfer in elliptic tubes arranged in staggered bundles with aluminum foam porous media inserts. Despite higher pressure drops at higher Reynolds numbers, they found that the use of aluminum foams significantly improved heat transfer. Altering pitch arrangements in laminar flow regimes effectively increased overall efficiency.

Zheng et al¹⁸ numerically studied the effect of rod-type vortex generator inserts in a heat exchanger tube. Parameters such as rod inclination angle, diameter ratio, and Reynolds number significantly influenced heat transfer and friction factor. Multi-objective optimization with artificial neural networks indicated that the 0.058-diameter and 57.057°-inclined vortex rod at 426767 Reynolds number provided the best heat transfer enhancement against pressure drop.

Li et al⁴⁷ explored the heat transfer and turbulent flow performance in a tube fitted with drainage inserts. They found that a 3.3 pitch ratio and a 45° inclination angle yielded the highest performance evaluation criterion, resulting in better heat transfer and flow performance.

Karagoz et al¹⁷ conducted experimental and numerical studies to enhance heat transfer rates using cylindrical turbulators in heat exchanger tubes. The effects of blade geometry and various turbulator configurations were explored. Experiments were performed with different turbulator ranges and angles, adjusting water flow rates to achieve the desired Reynolds numbers. The results revealed a significant increase in the Nusselt number due to the tube inserts, leading to energy savings. The study concluded that tube inserts significantly improve the Nusselt number, with the highest enhancement observed in the case of Sy1, which was 24% higher than in a straight tube. This research was also simulated using ANSYS Fluent 16 software to analyze flow behavior and heat transfer properties.

In the realm of horizontal components, 2-component gas–liquid slug flow is common in industrial applications, posing challenges for flow and heat transfer due to intermittent structures. The study aimed to estimate heat transfer properties for slug flow, developing a semi-theoretical heat transfer correlation based on Reynolds and Chilton–Colburn analogies. The research collected and analyzed 500 experimental data points and 8 heat transfer correlations, ultimately developing a new correlation.

This semi-theoretical correlation effectively estimated 91.5% of the data within a $\pm 30\%$ error margin. The study's applicability to other 2-phase flow regimes was also discussed.⁴⁸

Xin-Cheng et al⁴⁹ experimentally examined 2-phase flow distribution at the header of a single-plate heat exchanger, focusing on the liquification of natural gas with small liquid mass fractions. They used optical methods like Particle Image Velocimetry (PIV), Particle Tracking Velocimetry (PTV), and Laser-Induced Fluorescence (LIF) to measure liquid and gas flow rates. The research quantified and discussed the distribution of liquid and gas flows, specifically addressing the challenges and modifications required for porous deflectors or input nozzle configurations.

Karuppasamy et al⁵⁰ examined the turbulent forced convection of nanofluids in a circular tube with cone-shaped inserts. They used various nanofluid compositions and reported varying heat transfer enhancements. Different models were compared, with 2-phase mixture models proving more accurate.

Yadav and Sahu⁵¹ reported the impact of helical surface disc turbulators on heat transfer and pressure drop properties in a double-tube heat exchanger. They found that the lowest diameter ratio and increased helix angle led to higher Nusselt numbers and friction factors.

Xiong et al⁵² discussed the impact of conical and fusiform turbulators in a double-tube heat exchanger with circular inner tubes and varying configurations. They found that using a circular inner tube with a 12-mm fusiform turbulator resulted in the best thermal performance.

Mousa et al⁷ conducted a comprehensive review of single-phase heat transfer enhancement techniques. They classified methods into active and passive techniques, highlighting the advantages and challenges of each. Bashtani et al⁵³ numerically investigated the effects of adding aluminum oxide nanoparticles in a heat exchanger with turbulators. They found that turbulators significantly increased thermal effects, and the addition of nanofluid further improved heat transfer.

Khetib⁵⁴ conducted a numerical study to assess the effect of curved turbulators on the exergy efficiency of a solar collector using a 2-phase hybrid nanofluid. The study modeled the Multi-Wall Carbon NanoTubes (MWCNT)-TiO₂-water hybrid nanofluid and found that increasing Re and ϕ improved exergy efficiency. However, increasing the lateral ratio of the curved turbulators resulted in a decrease in exergy efficiency.

All the studies cited above focus on various methods and configurations to enhance heat transfer and reduce friction in heat exchangers and tubes, providing valuable insights for improving energy efficiency in different industries. Several methods, as well as modifications to turbulators or inserts, were investigated to achieve better heat transfer performance. Each study considered different parameters and geometries to optimize heat transfer and thermal efficiency.

Aim and Scope

Due to increased industrial needs and improved living standards, energy consumption has risen, making energy production more expensive. Therefore, there is a growing focus on researching, finding, and promoting alternative energy sources. Additionally, conserving and efficiently using energy has become a top priority worldwide. One crucial aspect of achieving energy efficiency and energy economy is enhancing heat transfer, which involves

the development of methods broadly categorized as "passive," "active," and "hybrid" methods.

In the context of 2-phase flows, the ideal state is characterized by stable flow, minimizing hydrodynamic and thermal fluctuations. Stable flow occurs when flow conditions within a channel change minimally, allowing the flow to asymptotically approach another stable state. In contrast, unstable flows do not asymptotically approach another state, exhibiting periodic oscillations in hydrodynamic and thermal properties such as flow rate, pressure, and temperature.

Unstable flows are common in 2-phase flow systems, such as cooling systems, steam generators, heat exchangers, steam boilers, and nuclear reactors. These flow instabilities, resulting from pressure and flow rate fluctuations, can lead to malfunctions and disruptions in the heat transfer components, significantly reducing the economic lifespan of these systems. Issues related to these fluctuations include thermal fatigue, boiling crises, mechanical vibrations, control difficulties due to transient high temperatures, and burn-out on the heat transfer surface, especially in nuclear power plant fuel elements.

Unstable 2-phase flows can manifest in various forms influenced by different factors and conditions. Understanding the mechanisms behind the formation of these instabilities is crucial for devising effective control and mitigation strategies. These instabilities are broadly classified into 2 categories: "static" and "dynamic" instabilities. Factors such as channel geometry, pressure, flow rate, and temperature play a significant role in influencing these instabilities.

Regarding steady-state characteristics, it was noticed that all improved surfaces exhibited a unique characteristic curve with a distinctive "S" shape. The onset of the 2-phase flow region typically occurred in the vicinity of the local minimum on this characteristic curve. Furthermore, there was a correlation between a decrease in inlet temperature and a subsequent reduction in pressure drop, with the pressure drops on the enhanced surfaces being consistently higher than those on conventional straight tubes.

In terms of stability boundaries, specific trends emerged. As the inlet temperature decreased, the point at which PDO (boundary of disturbance onset) occurred shifted toward lower mass flow rates. On improved surfaces, oscillations covered a broader section of the characteristic curve compared to their counterparts in straight tubes. The extent of this region was directly related to the duration of the oscillations. It is worth noting that the increased stability, particularly in cases where a helical spring element was used as an embedded enhancement device, may not be applicable universally to all improved surfaces.

Pressure drop oscillations revealed noteworthy patterns. As mass flow rates decreased, both the period and amplitude of PDO increased. Similarly, a reduction in the inlet temperature led to an upward trend in the period and amplitude of PDO. Furthermore, the improved surfaces consistently outperformed straight tubes in terms of both period and amplitude. The analysis extended to density fluctuation oscillations (DFO). It was observed that when mass flow rates decreased, the period and amplitude of DFO decreased as well. Conversely, a decrease in the inlet temperature resulted in an increase in the period and amplitude of DFO. Furthermore, improved surfaces consistently exhibited higher values for the period and amplitude of DFO when compared to

straight tubes. Lastly, the examination of thermal oscillations revealed consistent trends. Wall temperatures on improved surfaces consistently registered higher values than those seen in straight tubes. Moreover, the periods and amplitudes of these thermal oscillations were notably greater on improved surfaces. These thermal oscillations exhibited an increasing trend in both period and amplitude as the inlet temperature decreased and as mass flow rates decreased.

Given that experimental studies on 2-phase flow instabilities have predominantly focused on vertical tubes and channels, this thesis aims to investigate the impact of heat transfer improvements in horizontal tubes on 2-phase flow regimes and instabilities Table 1. To achieve this, experiments were conducted using a specially prepared test tube with an intermediate effective diameter. Various configurations with different pitch distances of helical wire inserts were used to assess their effects on flow stratification, amplitude, and oscillation periods.

This present study is aimed at contributing to scientific knowledge in the following ways:

- Designing 2-phase flow evaporators and heat exchangers with consideration of potential instabilities, preventing burnout, thermal fatigue, vibrations, and malfunctions, is important. The burnout phenomenon is influenced by geometry, operational conditions, and boundary conditions, such as axial heat flux distribution.
- Determining the effects and consequences of 2-phase flow instabilities on tube effective diameters and exploring the boundaries of oscillations and flow patterns.
- Despite the existing body of literature on 2-phase flow instabilities, research on the impact of heat transfer enhancement on these instabilities is limited. Therefore, this study, coupled with subsequent numerical modeling, is expected to make a significant contribution to this field.

MATERIAL AND METHODS

Experimental Setup

The experiments were conducted within the heat transfer laboratory of the Mechanical Engineering Department, utilizing a horizontal tubular test system. This setup was configured to obtain 2-phase flow and facilitate the investigation of pressure

Table 1. Effect of Heat Transfer Improvement on 2-Phase Flow Instabilities⁵⁵

Parameters	Characteristics
Steady state characteristics	<ol style="list-style-type: none"> 1. The characteristic curve on all treated surfaces is slanted S-shaped. 2. The 2-phase flow region starts around the local minimum of the characteristic curve. 3. As the inlet temperature decreases on improved surfaces, the pressure drop decreases. 4. Pressure drops on improved surfaces are higher than in straight Tubes.
Stability limits	<ol style="list-style-type: none"> 1. As the inlet temperature decreases, the starting point of PDO shifts to a lower flow rate. 2. With improved surfaces, oscillations cover a larger region in the characteristic curve than in a plain Tube. The larger this region, the longer the oscillations last. 3. When using a spring element as a built-in recovery device, stability increases as the effective diameter decreases. However, this result cannot be generalized to other improved surfaces.
Pressure drop oscillations	<ol style="list-style-type: none"> 1. As the mass flow rate decreases, the period and amplitudes of the PDO increase. 2. As the inlet temperature decreases, the periods and amplitudes of the PDO increase. 3. The periods and amplitudes of PDO with improved surfaces are higher than those in plain tube.
Density change oscillations	<ol style="list-style-type: none"> 1. As the mass flow rate decreases, the period and amplitudes of the DFOs decrease. 2. As the inlet temperature decreases, the periods and amplitudes of the DFO increase. 3. The periods and amplitudes of DFO with improved surfaces are higher than those in plain tubes.
Thermal oscillations	<ol style="list-style-type: none"> 1. Wall temperatures of improved surfaces are higher than those of straight Tubes. 2. The periods and amplitudes of wall temperatures with improved surfaces are higher than those in plain tubes. 3. The periods and amplitudes of thermal oscillations increase with decreasing inlet temperature. 4. The periods and amplitudes of thermal oscillations increase with decreasing mass flow rate.

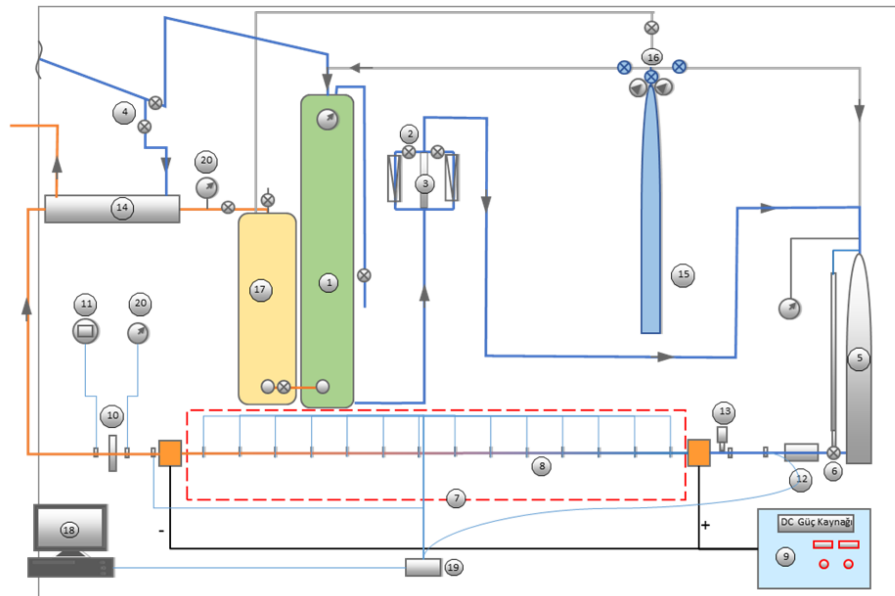
drop-type oscillations, density change-type oscillations, and thermal oscillations. The study focused on the effects of heat flux, flow rate, and tube internal elements consisting of differently stepped tapered coil arrays on the 2-phase stable and unstable flow characteristics in horizontal tubes.

As illustrated in Figure 1, the experimental setup consists of 3 main sections: fluid supply, test section, and storage section.

Fluid Supply Section

The fluid supply section, responsible for delivering water under specified conditions to the test tube, includes the main supply





Fluid Supply Section	Test Section	Fluid Discharge Section
1- Main supply tank	8- Test tube	15- Nitrogen tank
2- Flow rate arrangement valve	9- DC power supply	16- Regulator
3- Flowmeter (2 pcs)	10- Orifice	17- Storage tank
4- Valve	11- Digital manometer	18- Computer
5- Balancing tank	12- Flow transducer	19- Data acquisition card
6- Inlet control valve	13- Pressure transducer	20- Needle manometer
7- Test chamber	14- Condenser	

Figure 1. Photographic and schematic views of the experimental setup.

tank, a flow control valve, 2 flowmeters (one with a 0-400 L/h range and the other with a 0-1000 L/h range), a digital flow transducer, and a nitrogen tank with a pressure regulator.

The cylindrical main supply tank, which has a volume of 0.7 m³ and stands vertically at a height of 3 meters, is designed to store the required water for the duration of the experiment. It is capable of withstanding an operating pressure of up to 50 bar (Figure 1). The flow rate of the fluid in the supply line is controlled using a control valve. Two flowmeters and a digital flow transducer are employed to measure and adjust the flow rate. These flowmeters have a maximum operating pressure of 40 bar and a maximum operating temperature of 100°C, all of which are constructed from steel.

Test Section

The test section is the primary area of interest in the study where the targeted parameters are effective. It comprises nine elements, including a balance tank (5), an inlet flow control valve (6), a test chamber (7), a test tube (8), a DC power supply (9), an orifice (10), a digital manometer (11), turbine-type flow meters (12), and a pressure transducer (13).

In the event that the test tube's length is insufficient, a balance tank with a volume of 0.05 m³ is utilized to create a compressible volume. Additionally, to observe variations in fluid levels and compressible volume levels, a transparent plastic level gauge and a pressure gauge capable of withstanding 30 bars are connected to the balance tank, as depicted in Figure 1.

Between the balance tank and the test tube, components such as a turbine-type flow meter, Bourdon-type manometer, pressure transducer, and temperature measurement device are installed, as shown in Figure 1. A turbine-type flow meter is used to measure fluctuations in fluid flow; the Bourdon-type manometer measures fluid pressure at the test tube's inlet; and the pressure transducer is employed to measure fluctuations in fluid pressure at the inlet of the test tube. The fluid's inlet temperature is measured using a T-type thermocouple, and experiments are conducted within a mass flow rate range of 22 to 80 g/s.

A DC power supply with an approximate power rating of 40 kW is connected to the test chamber's inlet and outlet sections via its positive and negative terminals to transfer thermal power to the test tube. The heat power values supplied to the test tube are read from the digital voltage and current indicators on the DC power supply (Figure 2).

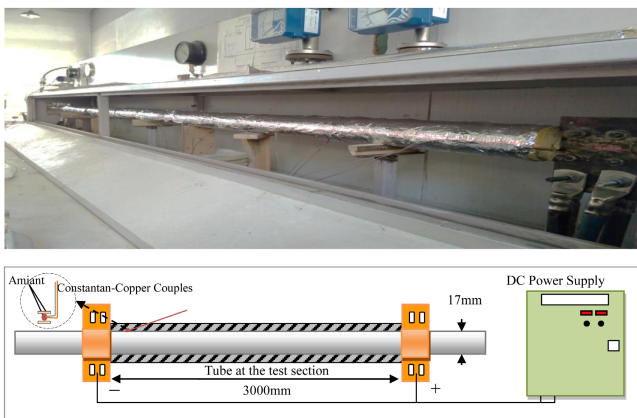


Figure 2. Test section with connections and instruments.

To achieve the desired pressure drop and determine the effects of the outlet restrictor on flow oscillations, an orifice plate is attached at the test tube's outlet, as shown in Figure 1. The pressure at the inlet side of the orifice plate is measured using a Bourdon-type manometer, and the pressure at the outlet side is measured using a Bourdon-type digital manometer.

Fluid Storage Section

The fluid storage section is composed of 2 primary elements: the condenser (14) and the fluid storage tank (17). This section is where the fluid is directed after leaving the test section. Typically, the fluid exits the test tube in a vapor phase and is then condensed in a water-cooled condenser to return it to its starting conditions. The condensed fluid is subsequently pumped into the storage tank. When needed, it can be pressurized using high-pressure nitrogen gas and fed back into the main supply tank or discharged.

The condenser, a horizontal body-tube heat exchanger, is employed to convert the fluid from the vapor phase to the liquid phase. The condenser body is constructed from a seamless black tube with a diameter of 0.16 m and a length of 1.45 m. Inside it, a 0.02-m-diameter copper tube is spirally placed, allowing the fluid from the test section to pass through from the outside while cooling water flows through the inside.

In the condenser, the fluid undergoes a phase change and is then sent to a vertical storage tank with a diameter of 0.75 m, a height of 1.75 m, and a wall thickness of 1 cm. From this storage tank, the fluid is pressurized using high-pressure nitrogen gas and pumped into the main supply tank when needed, or it can be discharged by opening the relief valve.

Uncertainty Analysis

Uncertainty analysis is a crucial aspect of any experimental study, as it quantifies the reliability and precision of measurements. Understanding and evaluating the uncertainty in measurements is essential for drawing meaningful conclusions and ensuring the validity of experimental results.

The experimental measurements were conducted in various aspects, including temperature, pressure, flow rate, and heat power. Each of these measurements was taken with a certain degree of precision, and their relative uncertainties were assessed (Table 2). Here is a reorganized summary of the measurements and their associated uncertainty:

Temperature Measurements

- Temperature measurements were made at 30 points along the experimental system using T-type copper-constantan thermocouples with a 0.25 mm diameter.
- A precision of $\pm 0.5^\circ\text{C}$ was achieved in these temperature measurements.
- In the test tube, temperature readings were taken using thermocouples attached to the tube wall, placed between 2 asbestos plates.
- At the inlet and outlet of the test tube, temperature measurements were carried out with thermocouples placed inside 5-mm-diameter closed-ended copper tubes.
- A total of 28 T-type thermocouples were installed along the length of the test tube at equal intervals (as shown in Figure 1).
- To minimize electrical interference and reduce noise, the thermocouple junctions were electrically insulated but had good thermal conductivity between the asbestos plates.

Table 2. Uncertainties in measurements

Measurement Type	Relative Uncertainty
Temperature	0.1°C to 0.5°C
Pressure	0.1%
Flow rate	0.4%
Heat power	0.2%

- Data was collected using an analog/digital Advantech Data Acquisition card and VisiDAQ 3.1 software.
- The total error in temperature measurements ranged from 0.1°C to 0.5°C, depending on the selected gain value of the control card.

Pressure Measurements

- Pressure measurements were conducted at several points in the system, including the main tank, balance tank, nitrogen tank, and before and after the orifice.
- Bourdon-type analog manometers with a precision of ± 0.1 bar were used to measure pressure in the main tank, balance tank, nitrogen tank, and the inlet of the orifice.
- The pressure after the orifice was measured using a digital manometer with a 0.5 bar resolution.
- The analog signals from the Bourdon-type manometers and pressure transducers were processed using a data acquisition card (as seen in Figure 1).
- The total error in the pressure measurements was 0.1%.

Flow Rate Measurements

- Precise mass flow rate measurements were essential for determining the oscillation limits and stability boundaries of flow regimes.
- Flow rate adjustment was facilitated by a control valve in the system.
- Two flowmeters were used to measure and adjust the flow rate, with a total error of 0.4%. These flowmeters had measurement ranges of 0-400 L/h and 0-1000 L/h.
- Experiments were conducted within a mass flow rate range of 25 to 140 g/s.
- A turbine-type flow meter was installed between the balance tank and the test tube to measure flow rate oscillations.
- The total error in flow rate measurements was 0.05%.

Heat Power Measurements

- Approximately 40 kW of DC power supply was used in the experimental setup.
- The voltage and current values could be adjusted and read independently on the power supply.
- The total error in electrical power measurements was determined to be 0.2%.

Experimental Method

Experimental studies were carried out in 2 stages: stable experiments, in which steady-state characteristics were determined, and unstable experiments, in which 2-phase flow dynamic instabilities were investigated. The experiments were carried out at constant thermal power, constant fluid inlet temperature, constant outlet orifice diameter, and 4 different types of tubes.

The heat transfer surfaces and characteristics of the heat transfer improvement elements whose photographs are shown in Figure 4 are given in Figure 3. The plain tube without a surface-increasing element is named tube 1, and the tubes with surface-increasing elements consisting of conical wound spring arrays with different spring steps are named tube 2, tube 3, and tube 4. As shown in

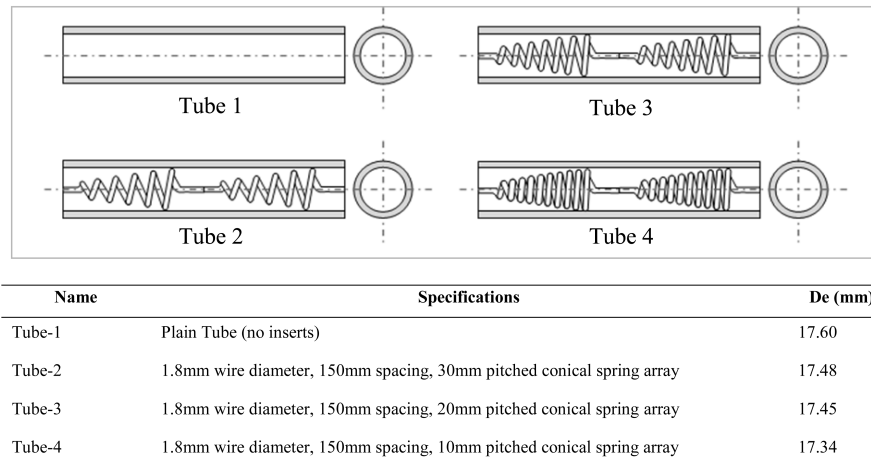


Figure 3. Insert configurations and their specifications.

Figure 3, heat transfer surfaces are characterized by the effective diameter calculated using the following equation:

$$d_e = \sqrt{\frac{4V'}{\pi L}} \quad (1)$$

where V' is the internal volume and L is the length of the tube.

Experiments were conducted to determine steady-state characteristics, starting with a plain tube and a constant outlet orifice restriction. These experiments were performed at an inlet temperature (T_i) of 20°C and a heat power (Q) of 22 kW. Subsequently, unstable experiments were conducted under the same experimental parameters. The tests included tube 1, followed by tube 2, tube 3, and tube 4.

The following parameters were measured for each experiment:

- Surface temperatures of the test tube (14 readings at the bottom and 14 at the top, totaling 28 readings).
- Inlet and outlet temperatures of the fluid in the test tube.
- Static pressure at the inlet and outlet of the test tube.
- Inlet mass flow rate of the test tube.
- Mass flow rate oscillations at the inlet of the test tube.
- Pressure oscillations at the inlet of the test tube.
- Pressure at the inlet and outlet of the orifice.

Steady-state characteristic experiments aim to determine the pressure drop as a function of mass flow rate and are represented graphically. This pressure drop is the difference between

the equilibrium tank pressure and the fluid pressure after the orifice plate. The experiments commenced with a mass flow rate (\dot{m}) of 80 g/s and were then reduced at intervals of approximately 8-10 g/s to establish the characteristic curve. To fully understand the characteristics of steam flow, the mass flow rate was reduced to very low values. The lowest mass flow rate was set at 22 g/s due to burnout concerns. Observations of wall temperatures and fluid outlet temperatures were made to detect burnout conditions.

The experimental process to determine steady-state characteristics followed these steps:

- The main tank was pressurized to the system pressure using nitrogen gas, adjusting the system pressure with a pressure regulator valve on the nitrogen cylinder.
- To ensure that there was no compressible volume in the unused balancing tank during steady-state experiments, the nitrogen gas inside the balancing tank was vented by monitoring the level indicator.
- The mass flow rate was adjusted to the maximum value determined in the experimental work by using a control valve.
- The digital thermostat was used to set the inlet temperature of the water from the main tank to the test tube.
- The cooling water circuit of the heat exchanger condensing the working fluid was activated.
- The system was started, and stability was awaited.
- An adjustable DC power supply was used to apply heat to the system, ensuring that the required heat power was attained.

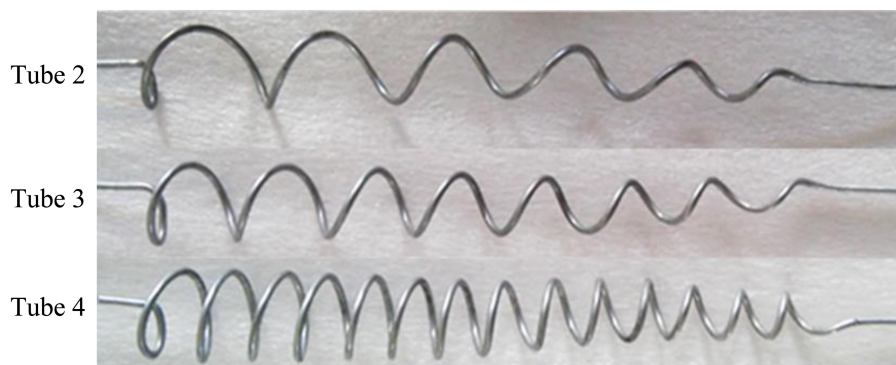


Figure 4. Conical spring inserts used in each tube for heat transfer enhancement.

- The system was allowed to reach a stable state, as confirmed by no more than a 0.5°C variation in test tube surface temperatures. When this stability was achieved, measurements were taken, and the experiment for the given mass flow rate was considered complete.
- The above steps were repeated for different mass flow rates until the inlet mass flow rate reached 22 g/s.

Unstable state characteristic experiments aimed to investigate dynamic flow instabilities, including pressure drop type, density fluctuation type, and thermal oscillations. To induce instabilities, a compressible volume was ensured in the balancing tank before the test section. The water level inside the balancing tank was maintained at a specific level using a constant gas pressure obtained from the nitrogen tank. While the compressible volume was held constant in all experiments, the magnitude of this volume varied due to oscillations in mass flow and pressure.

The steps for conducting unstable-state experiments were as follows:

- The system was pressurized with nitrogen gas from the nitrogen tank, adjusting the system pressure with a regulator.
- To allow comparisons based on the presence of a compressible volume in the balancing tank, the balancing tank was pressurized in all experiments using a pressurized nitrogen tank and regulator, and the water level in the transparent level indicator was adjusted.
- The mass flow rate was adjusted to achieve the maximum flow rate determined in the experimental work.
- The cooling water circuit of the heat exchanger was activated.
- The system was started and verified for weak yet stable operation.
- Thermal power was transferred to the system by adjusting the current and voltage through the DC power supply.
- Instantaneous temperature values were monitored via thermocouples, and the system was allowed to stabilize, as indicated by temperature changes not exceeding 0.5°C.
- Experiments continued with a gradual reduction in mass flow rate until the point of oscillation onset.
- To determine the transition from boiling-dominated oscillations (PDO) to independent vapor-dominant oscillations (DFO), small reductions in mass flow rate were made, and low oscillation periods were examined.

- Wall temperatures and flow temperatures were observed carefully as mass flow decreased, especially concerning thermal oscillations.
- When significant deviations between wall and fluid temperatures indicating the onset of burnout were observed, the heat power was cut, and the experimental work was terminated.

RESULTS AND DISCUSSION

Stable state characteristic curves, represented by an x - y plot of pressure drop versus mass flow rate, commonly used to understand flow characteristics in 2-phase flow systems, were created for each test tube, and pressure drop values were calculated using the difference between the equilibrium tank pressure and the test tube outlet pressure at various mass flow rates. The curves exhibit positively sloped sections corresponding to high mass flow rates in the single-phase liquid region, where the minimum occurs. The negatively sloped region indicates the inception of 2-phase flow with the formation of initial bubbles. As the number of bubbles increases, both the liquid and vapor phases coexist, leading to a lower fluid density compared to the liquid phase, consequently causing an increase in pressure drop. Further reduction in mass flow rates leads to the transition from the negatively sloped region to the positively sloped one as the pressure drop values decrease.

Comparison of Stable-State Curves

Characteristic state curves were generated for each test tube, comparing their values for parameter 'k'. The experiments were conducted with a constant inlet fluid temperature ($T_i=20^\circ\text{C}$) and a constant heat power ($Q=22\text{ kW}$), including measurements without power input ($Q=0$). Figure 6, 7 and 8 illustrate the temperatures of the lower and upper tube walls at no power and power conditions. The characteristic state curves are provided for each tube. A comparison of pressure drop values reveals differences among the 4 test tubes. Tube 4, equipped with surface enhancement elements composed of 10 mm pitch springs, exhibited the highest pressure drop value, whereas tube 1 had the lowest pressure drop value. When ranked based on pressure drop values, the tubes were observed to have ranked as tube 1 < tube 2 < tube 3 < tube 4. In tubes with surface enhancement elements, flow stratification and frictional pressure drops caused an even bigger drop in pressure. This was because the vapor phase caused more pressure drop as the mass flow rates dropped, which was higher than the pressure drop values in plain tubes. Increased system

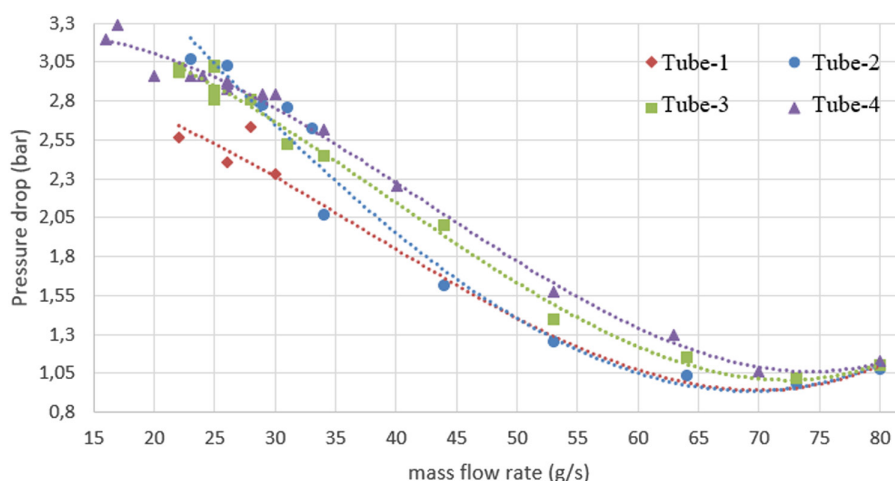


Figure 5. Pressure drop in the tubes at different mass flow rates.

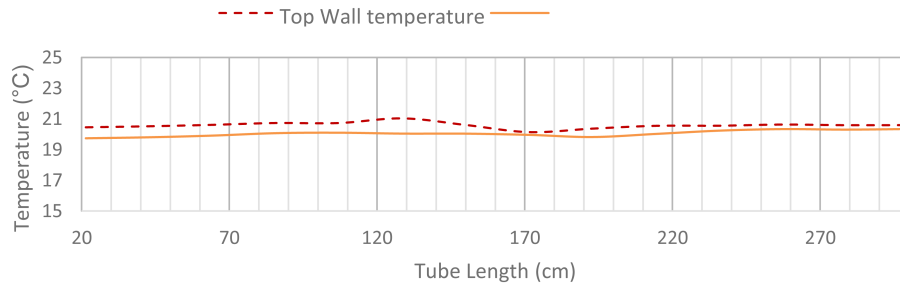


Figure 6. Top and bottom wall temperatures with tube 1 at no-power condition.

instability is associated with regions in the stable state curves where the negative slope angle becomes steeper. In such cases, plain tube curves are expected to have fewer negative slope regions compared to the curves of tubes with surface improvement elements, and the graphs confirm this expectation.

This analysis reveals how the addition of surface enhancement elements in tubes affects stable state characteristics and pressure drop values, with tube 1 having the lowest pressure drop and tube 4 the highest.

As a result of the experiments that continued by reducing the mass flow by small amounts, $m=28$ g/s, $m=26$ g/s, and $m=22$ g/s were determined as the comparison criteria of the in-Tube elements, and how each element would change this curve with the same system parameters was examined.

When all tubes are examined in themselves, it is seen that there is an increase in both lower and upper wall temperatures as the mass flow decreases. When sorted in terms of whether there is a significant separation between the lower (Figure 10) and upper

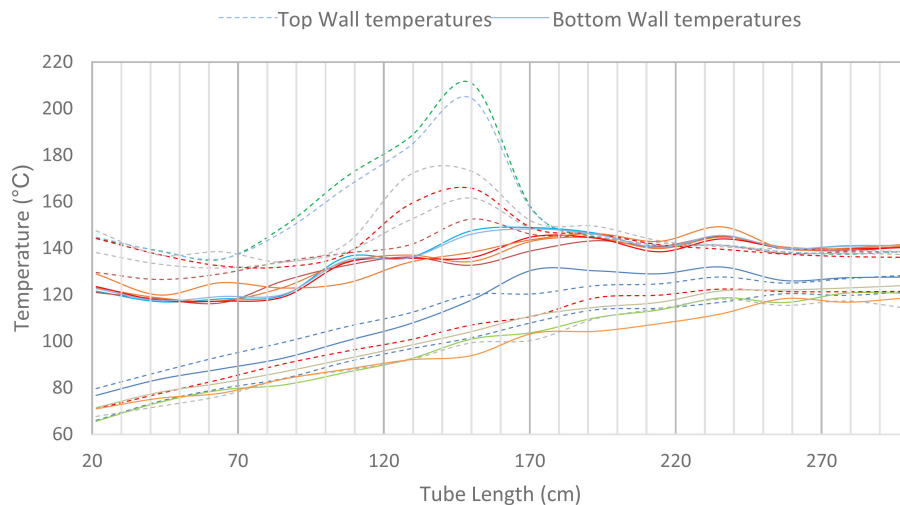


Figure 7. Top (- -) and bottom (—) Wall temperatures for all mass flow rates tested with tube 1.

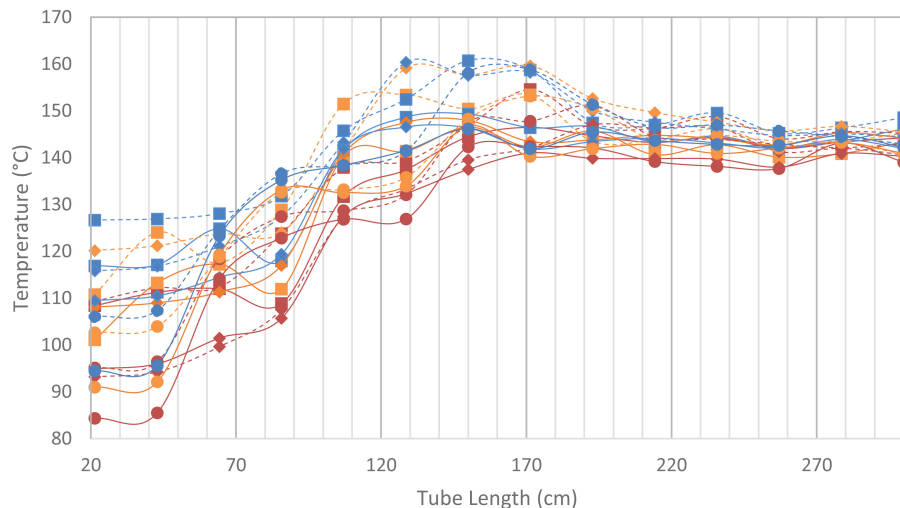


Figure 8. Top (- -) and bottom (—) Wall temperatures at 22 (blue), 26 (orange), and 28 (red) g/s mass flow rates in tube 2 (■), tube 3 (◆), and tube 4 (●).

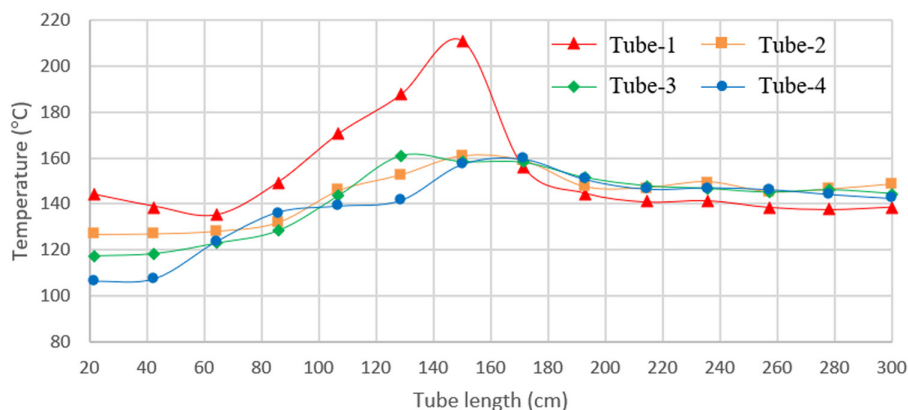


Figure 9. Top Wall temperatures at $\dot{m} = 22$ g/s in all tubes.

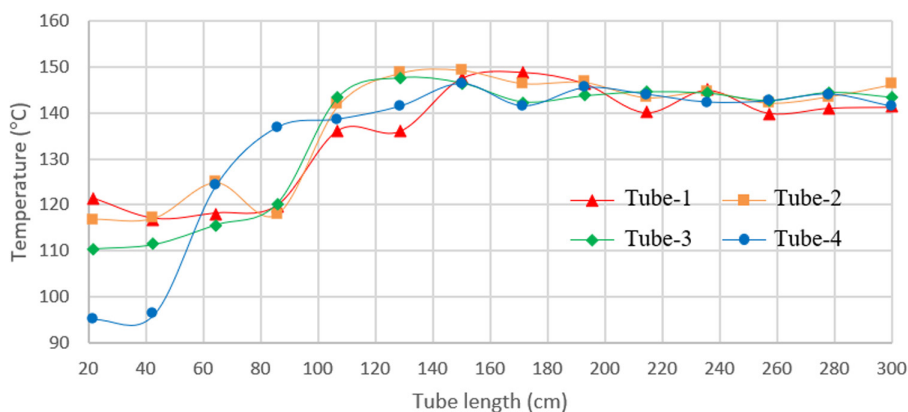


Figure 10. Bottom wall temperatures at $\dot{m} = 22$ g/s in all tubes.

(Figure 9) wall temperatures, it is seen that the most significant separation occurred at a flow rate of 22 g/s for tube 1, followed by tube 2, tube 3, and tube 4, respectively.

Although the tube diameter, wall thickness, inlet water temperature, and thermal power used in this study are unique in combination, the results obtained are consistent with the literature in terms of ensuring interphase coalescence and interaction, especially in 2-phase flow systems with stratified flow and circular flow regimes.

In this study, 2-phase flow events in forced-convection horizontal tubes were experimentally examined. The effects of heat transfer surface enhancement elements on stable and unstable flow events were investigated. Four different tubes were employed in the study: one was a plain tube, and the other 3 had surface enhancement elements consisting of helical springs with equal pitch and conicity angles, with 10 mm, 20 mm, and 30 mm pitch increments. The experiments were conducted in a 2-phase flow system with water as the working fluid under constant thermal power, outlet orifice diameter, fluid inlet temperature, and inlet pressure conditions. The experimental results can be summarized as follows:

- Characteristic curves for each tube exhibited differences in pressure drop values, indicating that the use of internal elements increased the pressure drop.
- Experiments were conducted at different mass flow rates while keeping thermal power, system pressure, fluid inlet temperature, outlet restrictor, and compressible volume constant.

The goal of this study was to find out how heat transfer and pressure drop are affected by helical spring arrays that are used as inserts in a forced-convection, boiling, horizontal, 2-phase flow tube system. For future research, the following recommendations can be made:

- The performance and effects of tube internal elements, including bent, strip, helical, and spring-like structures, should be compared under identical experimental conditions to evaluate their performance in the same experimental system.
- Geometric parameters of tube internal elements, such as the distance between each spring array, the conicity angle of springs, and the orientation of conical springs in the flow direction, should be examined and compared with the results of this study to fully determine their effects.
- An investigation of the orientation of helical springs in relation to flow instability, oscillation boundaries, and heat transfer effects should be conducted.
- Altering the distances and winding lengths of helical spring arrays with equal intervals and comparing the effects of these parameters.
- The experimental results of this entirely experimental study can be analyzed numerically and compared with experimental data to assess the consistency of the numerical and experimental results.
- The applicability of helical spring arrays in vertical or inclined systems can be compared with the findings of this study, considering the study was conducted in a horizontal tube system.

- Research can be carried out by changing parameters such as the size of the natural compressible volume, the heat transfer method, and the tube diameter in the construction and operation of the test system.
- To achieve more homogeneous energy distribution to the test tube, a different method can be employed, different from the way the heat energy was applied to the tube, which was connected to the near ends of the inlet and outlet. This change in energy application is needed to reduce uncertainties in wall temperature measurements.

Peer-review: Externally peer-reviewed.

Author Contributions: Concept – Ö.Ç.; Design – Ö.Ç., M.K.Y.; Supervision – Ö.Ç.; Resources – Ö.Ç., M.K.Y.; Materials – Ö.Ç., M.K.Y.; Data Collection and/or Processing – M.K.Y.; Analysis and/or Interpretation – M.K.Y.; Literature Search – Ö.Ç., M.K.Y.; Writing Manuscript – M.K.Y.; Critical Review – Ö.Ç., M.K.Y.

Declaration of Interests: The authors declare that they have no competing interest.



Funding: The authors declared that this study has received no financial support.

REFERENCES

- Godino DM, Corzo SF, Ramajo DE. Two-phase modeling of water-air flow of dispersed and segregated flows. *Ann Nucl Energy*. 2020;149:107766. [CrossRef]
- Wang W, Yang D, Liang Z, Qu M, Ouyang S. Experimental investigation on flow instabilities of ultra-supercritical water in parallel channels. *Applied Therm Engineering*. 2019;147:819-828. [CrossRef]
- Yeoh G. *Handbook of Multiphase Flow Science and Technology*; 2020. [CrossRef]
- Kakaç, S., A Review of Two-Phase Flow Instabilities. In *Advances in Two-Phase Flow on Heat Transfer*, Martinus, Nijhoff, Boston, vol.11, 577-668,1994.
- Bergles AE. *Review of Instabilities in Two Phase Systems. Two Phase Flows and Heat Transfer* (Kakaç S, Mayinger F, eds, vol 1). 1977:383-385.
- Cao Z, Wu Z, Luan H, Sunden B. Numerical study on heat transfer enhancement for laminar flow in a tube with mesh conical frustum inserts. *Numer Heat Transf A*. 2017;72(1):21-39. [CrossRef]
- Mousa MH, Miljkovic N, Nawaz K. Review of heat transfer enhancement techniques for single phase flows. *Renew Sustain Energy Rev*. 2021;137:110566. [CrossRef]
- Liu H, Zheng G, Man C, Jiang K, Lv X. Numerical and experimental studies on heat transfer enhancement in a circular tube inserted with twisted tape inserts. *Am J Energy Eng*. 2021;9(2):30. [CrossRef]
- Shivamallaiiah MM, Fernandes DV. Numerical investigation of heat transfer and friction factor characteristics of circular tube fitted with an array of semi-elliptical vortex generator inserts. *Cogent Eng*. 2021;8(1). [CrossRef]
- Nikoozadeh A, Behzadmehr A, Payan S. Numerical investigation of turbulent heat transfer enhancement using combined propeller-type turbulator and nanofluid in a circular tube. *J Therm Anal Calorim*. 2020;140(3):1029-1044. [CrossRef]
- Mohammed HA, Ali Abuobeida IAM, Vuthaluru HB, Liu S. Two-phase forced convection of nanofluids flow in circular tubes using convergent and divergent conical rings inserts. *Int Commun Heat Mass Transf*. 2019;101:10-20. [CrossRef]
- Chamoli S, Lu R, Xie J, Yu P. Numerical study on flow structure and heat transfer in a circular tube integrated with novel anchor shaped inserts. *Applied Therm Engineering*. 2018;135:304-324. [CrossRef]
- Liu P, Zheng N, Shan F, Liu Z, Liu W. An experimental and numerical study on the laminar heat transfer and flow characteristics of a circular tube fitted with multiple conical strips inserts. *International J Heat Mass Transf*. 2018;117:691-709. [CrossRef]
- Waghole DR. Experimental and numerical investigation on heat transfer augmentation in a circular tube under forced convection with annular differential blockages/inserts. *Heat Mass Transfer*. 2018;54(6):1841-1846. [CrossRef]
- Jinxing W, Chao W, Mingqiang W, Yanhui L, Yafei L. Numerical Simulation of Turbulent Fluid Flow and Heat Transfer in a Circular Tube with Twisted Tape Inserts. *Journal of Zhengzhou University (Engineering Science)* (2017) 38(02):10-14.
- Jassim NA, Abdul Hussin K, Abdul Abbass NY. Numerical investigation of heat transfer enhancement in circular tube using twisted tape inserts and nanotechnology. *Wasit J Eng Sci*. 2017;5(2):42-54. [CrossRef]
- Karagoz S, Afshari F, Yildirim O, Comakli O. Experimental and numerical investigation of the cylindrical blade tube inserts effect on the heat transfer enhancement in the horizontal pipe exchangers. *Heat Mass Transfer*. 2017;53(9):2769-2784. [CrossRef]
- Zheng N, Liu P, Wang X, Shan F, Liu Z, Liu W. Numerical simulation and optimization of heat transfer enhancement in a heat exchanger tube fitted with vortex rod inserts. *Appl Therm Eng*. 2017;123:471-484. [CrossRef]
- Raheemah SH, Ashham MA, Salman K. Numerical investigation on enhancement of heat transfer using rod inserts in single pipe heat exchanger. *J Mech Eng Sci*. 2019;13(4):6112-6124. [CrossRef]
- Adiguzel N, Göcücü A. Experimental investigation of the effects of ring turbulators on heat transfer in two-phase flow. *Iran J Sci Technol Trans Mech Eng*. 2021:1-10. [CrossRef]
- Anvari AR, Javaherdeh K, Emami-Meibodi M, Rashidi AM. Numerical and experimental investigation of heat transfer behavior in a round tube with the special conical ring inserts. *Energy Convers Manag*. 2014;88:214-217. [CrossRef]
- Outokesh M, Ajarostaghi SSM, Bozorgzadeh A, Sedighi K. Numerical evaluation of the effect of utilizing twisted tape with curved profile as a turbulator on heat transfer enhancement in a pipe. *J Therm Anal Calorim*. 2020;140(3):1537-1553. [CrossRef]
- Mashayekhi R, Arasteh H, Toghraie D, Motaharpour SH, Keshmiri A, Afrand M. Heat transfer enhancement of water-Al₂O₃ nanofluid in an oval channel equipped with two rows of twisted conical strip inserts in various directions: a two-phase approach. *Comput Math Appl*. 2020;79(8):2203-2215. [CrossRef]
- Agrebi S, Solano JP, Snoussi A, ben Brahim A. Numerical simulation of convective heat transfer in tube with wire coil inserts. In: 2015 World Symposium on Mechatronics Engineering & Applied Physics (WSMEAP): IEEE; 2015. [CrossRef]
- Abbas EF, Weis MM, Ridha AS. Experimental and numerical study of heat transfer enhancement in a shell and tube heat exchanger using helical coiled wire inserts. *Tikrit J Eng Sci*. 2018;25(2):74-79. [CrossRef]
- Min C, Li H, Gao X, Wang K, Xie L. Numerical investigation of convective heat transfer enhancement by a combination of vortex generator and in-tube inserts. *Int Commun Heat Mass Transf*. 2021;127:105490. [CrossRef]
- Davidov AA. *Elimination of Pulsation in Once through Boilers*, vol 3. USSR: Elektricheskies Stantzu, 1956:36-43.
- Stenning AH, Veziroğlu TN. Flow oscillation modes in forced convection boiling. In: *Proc. Heat Transfer and Fluid Mechanics Institute*. Palo Alto: Stanford Univ. Press; 1965:301-316.
- Veziroğlu TN, Lee SS. Boiling upward flow instabilities. *AEC- Oak Ridge National Laboratory Subcontract*. 1968;2975.
- Veziroğlu TN; Lee, SS, Boiling flow instabilities in a two parallel channel upflow system, Final Report to AEC-Oak Ridge National Laboratory Subcontract No. 2975, 1969.
- Veziroğlu, TN and Lee, SS. Instabilities in boiling upward flow. In *Proceedings of International Symposium On Concurrent Gas-Liquid Flow*. 1968.

32. Aritomi M, Aoki S, Inoue A. Instabilities in parallel channel of forced convection boiling upflow system. *J Nucl Sci Technol*. 1977;1-30.
33. Aritomi M, Aoki S, Inoue A. Instabilities in parallel channel of forced convection boiling upflow system (V). *J Nucl Sci Technol*. 1982;20(4):286-301.
34. Aritomi M, Aoki S, Inoue A. Instabilities in parallel channel of forced convection boiling upflow system (II). *J Nuc Sci Tech*. 1979;14(2):88-96.
35. Kakaç S, Veziroğlu TN, Padki MM, Fu LQ, Chen XJ. Investigation of thermal instabilities in a forced convection upward boiling system. *Exp Therm Fluid Sci*. 1990;3(2):191-201. [\[CrossRef\]](#)
36. Padki MM, Palmer K, Kakaç S, Veziroğlu TN. Bifurcation analysis of pressure drop oscillations and the Ledinegg instability. *Int J Heat Mass Transf*. 1992;35(2):525-532. [\[CrossRef\]](#)
37. Ding Y. *Experimental Investigation of Two Phase Flow Phenomena in Horizontal Convective in Tube Boiling System* (Ph.D. Thesis). Florida USA: University of Miami; 1993:21-65.
38. Xiao M, Chen XJ, Zhang MY, Veziroğlu TN, Kakaç S. A multivariable linear investigation of two phase flow instabilities in parallel boiling channels under high pressure. *Int J Multiphase Flow*. 1993;19(1):65-77. [\[CrossRef\]](#)
39. Liu HT, Kakaç S, Mayinger F. Characteristics of transition boiling and thermal oscillation in an upflow convective boiling system. *Exp Therm Fluid Sci*. 1994;8(3):195-205. [\[CrossRef\]](#)
40. Liu HT, Kakaç S, Mayinger F. Characteristics of transition boiling and thermal oscillations in an up flow convective boiling system. In: 29th ASME/ AIChE/ ANS/ AIAA, National Heat Transfer Conference. Atlanta, Georgia; 1993:8-11.
41. Guo L-J, Feng Z-P, Chen X-J. Pressure drop oscillation of steam-water two-phase flow in a helically coiled tube. *Int J Heat Mass Transf*. 2001;44(8):1555-1564. [\[CrossRef\]](#)
42. Çomaklı Ö, Karslı S, Yılmaz M. Experimental investigation of two phase flow instabilities in A horizontal in-tube boiling system. *Energy Convers Manag*. 2002;43(2):249-268. [\[CrossRef\]](#)
43. Yu W, France DM, Wambsganss MW, Hull JR. Two-phase pressure drop, boiling heat transfer, and critical heat flux to water in a small-diameter horizontal tube. *Int J Multiphase Flow*. 2002;28(6):927-941. [\[CrossRef\]](#)
44. Salman SD, Kadhum AAH, Takriff MS, Mohamad AB. Numerical investigation of heat transfer and friction factor characteristics in a circular tube fitted with V-cut twisted tape inserts. *ScientificWorldJournal*. 2013;2013:492762. [\[CrossRef\]](#)
45. Alam T, Saini RP, Saini JS. Heat and flow characteristics of air heater ducts provided with turbulators—A review. *Renewable and Sustainable Energy Reviews* (2014) 31:289–304. doi:[\[CrossRef\]](#)
45. Razzaghi H, Layeghi M, Goodarzi S, Lotfizadeh H. Numerical analysis of the effects of changeable transverse and longitudinal pitches and porous media inserts on heat transfer from an elliptic tube bundle. *Journal of Theoretical and Applied Mechanics* (2014) 52(3):767-780.
47. Li P, Liu P, Liu Z, Liu W. Experimental and numerical study on the heat transfer and flow performance for the circular tube fitted with drainage inserts. *International J Heat Mass Transf*. 2017;107:686-696. [\[CrossRef\]](#)
48. Dong C, Hibiki T. Heat transfer correlation for two-component two-phase slug flow in horizontal pipes. *Applied Therm Engineering*. 2018;141:866-876. [\[CrossRef\]](#)
49. Tu X-C, Wu Y, Kim H-B. Improvement of two-phase flow distribution in the header of a plate-fin heat exchanger. *International J Heat Mass Transf*. 2018;123:523-533. [\[CrossRef\]](#)
50. Karuppasamy M, Saravanan R, Chandrasekaran M, Muthuraman V. Numerical exploration of heat transfer in a heat exchanger tube with cone shape inserts and Al₂O₃ and CuO nanofluids. *Mater Today Proc*. 2020;21:940-947. [\[CrossRef\]](#)
51. Yadav S, Sahu SK. Heat transfer augmentation in double pipe water to air counter flow heat exchanger with helical surface disc turbulators. *Chem Eng Process Process Intensif*. 2019;135:120-132. [\[CrossRef\]](#)
52. Xiong Q, Izadi M, Shokri rad M, Shehzad SA, Mohammed HA. 3D numerical study of conical and fusiform turbulators for heat transfer improvement in a double-pipe heat exchanger. *International J Heat Mass Transf*. 2021;170:120995. [\[CrossRef\]](#)
53. Bashtani I, Esfahani JA, Kim KC. Effects of water-aluminum oxide nanofluid on double pipe heat exchanger with gear disc turbulators: A numerical investigation. *J Taiwan Inst Chem Eng*. 2021;124:63-74. [\[CrossRef\]](#)
54. Khetib Y, Sedraoui K, Melaibari AA, Alsulami R. The numerical investigation of spherical grooves on thermal-hydraulic behavior and exergy efficiency of two-phase hybrid MWCNT-Al₂O₃/water nanofluid in a parabolic solar collector. *Sustain Energy Technol Assess*. 2021;47:101530. [\[CrossRef\]](#)
55. Boure JA, Bergles AE, Tong LS. Review of two-phase flow instability. *Nucl Eng Des*. 1973;25(2):165-192. [\[CrossRef\]](#)

Nonporous Carbon-Supported Platinum Catalyst for Polymer Electrolyte Membrane Fuel Cell

Ayşenur ÖZTÜRK AYDIN¹
Ayşe BAYRAKÇEKEN
YURTCAN^{1,2}

¹Department of Chemical Engineering, Atatürk University, Faculty of Engineering, Erzurum, Turkey

²Nanoscience and Nanoengineering Research and Application Center, Atatürk University, Erzurum, Turkey

ABSTRACT

In this study, a commercial, nonporous carbon black was used as catalyst support for the dispersion of platinum (Pt) nanoparticles (NPs) in a polymer electrolyte membrane (PEM) fuel cell. The microstructure of nonporous carbon black was determined by Brunauer–Emmett–Teller analysis and crystal structure by x-ray diffraction (XRD) analysis. The surface area of carbon black is 72.6 m²/g, and the micropore volume has low fraction in the total volume. The fact that the $d_{(002)}$ value determined according to XRD analysis is 0.377 nm indicates the amorphous structure of nonporous carbon. Inductively coupled plasma mass spectrometry (ICP-MS) analysis determined the Pt loading on nonporous carbon as 15 wt.%. Catalyst support was also investigated electrochemically by cyclic voltammetry (CV) and electrochemical impedance spectroscopy (EIS). In CV analysis, as the scan rate increases, capacitive property increases. Furthermore, the low current density of the quinone–hydroquinone (Q–HQ) redox peak suggests nonporous carbon black's corrosion resistance. Nonporous carbon black, whose charge transfer resistance is 454.5 Ω based on EIS analysis, facilitates the mass transfer of species due to its low porosity. Nonporous carbon is preferred to alleviate the water flooding that occurs at the cathode electrode of PEM fuel cells. Platinum NPs supported with nonporous carbon provided 15 and 40 mW/cm² maximum power densities in PEM fuel cell performance tests at 60°C and 70°C, respectively. As the sustainable energy conversion technology of the future, PEM fuel cells can produce enough power to operate everything from mW-scale portable applications to kW–MW-scale transportation and residential uses. In this study, the performance of the nonporous carbon-supported Pt catalyst can be suitable for mW scale applications.

Keywords: Nonporous carbon black, Pt catalyst, support material, ORR, PEM fuel cell

INTRODUCTION

Solar, wind, marine, nuclear, hydro, biofuels, and geothermal fuels are renewable energy sources that can be alternatives to traditional fossil fuels to meet the increasing energy demand of the world population. Another alternative, which has gained importance in recent years due to its enormous energy content, is hydrogen. Chemical energy is directly and cleanly converted to electricity in fuel cells by using hydrogen as fuel. Efforts continue to meet the energy needs of the transportation sector, which constitutes 60% of total energy consumption, with hydrogen-based energy systems.¹ A polymer electrolyte membrane (PEM) fuel cell is a kind of fuel cell in which a thin, solid membrane that is permeable to hydrogen ions but not electrons is used as an electrolyte.²

The kinetics of the oxygen reduction reaction (ORR) taking place at the cathode electrode of a PEM fuel cell are quite slow. Thus, highly active and stable platinum (Pt) catalysts are often used to catalyze this reaction.³ Expensive and rare Pt metals are dispersed on conductive carbon materials to increase catalyst utilization. The preference for carbon-based materials in PEM fuel cell catalysts is due to their nano-sized morphology, pore structure, high surface area, good electrical conductivity, and corrosion resistance. The electrical conductivity, active surface area, and stability of the support material are effective in determining the performance of the carbon-supported Pt catalyst in the PEM fuel cell. Excluding the most widely used carbon black,⁴ carbon nanotubes (CNTs) and graphene are also frequently used carbon-based support materials.⁵

Microstructure in carbon black refers to three types of pore structures. These are micro-, meso-, and macropores, respectively. The micropores represent the pores within the primary carbon particles, while the meso- and macropores represent the pores within the aggregates formed by these primary carbon particles.⁶ Generally, as a result of the exposure of carbon structures to various activation processes, the micropore (<2 nm) fraction increases, and the Brunauer–Emmett–Teller (BET) surface area

Received: 05.12.2023

Accepted: 06.12.2023

Publication Date: 31.12.2023

Corresponding author:

Ayşe BAYRAKÇEKEN YURTCAN
Email: ayse.bayrakceken@gmail.com

Cite this article as: Öztürk Aydın A, Bayrakçeken Yurtcan A. Nonporous Carbon-Supported Platinum Catalyst for Polymer Electrolyte Membrane Fuel Cell. *NanoEra* 2023;3(2):53–60.



Content of this journal is licensed under a Creative Commons Attribution-NonCommercial-NoDerivatives 4.0 International License.

varies between 800–1200 m²/g according to the degree of activation. Activated carbon materials can be preferred as catalyst support materials in different fuel cell types due to their large surface areas.⁷ However, the abundance of meso- and macropores in the total area instead of micropores provides a more effective distribution of metal catalyst nanoparticles (NPs) on the support.⁸ Although the use of carbon black as a support material in fuel cells is common, the intense microporosity of some types reduces the activity of the catalyst because it traps metal NPs.⁹ Microporosity directly affects the catalyst and ionomer interaction, so it is proper to have accessible pores in the support.^{9,10}

In recent years, studies on the utilization of nonporous carbons in electrochemical applications have appeared in the literature. Han et al¹¹ obtained nonporous graphite from low-cost coal for use as material in the anode electrodes of lithium-ion batteries. They intended to eliminate the side reactions with the electrolyte in large surface areas and porous carbon materials by using a nonporous and less defective carbon structure. The authors attained a high reversible capacity value of 347 mAh/g for the storage of lithium ions with this new carbon structure. Additionally, nonporous carbon provided better electrical conductivity and facile ion transfer. Mizutani et al¹² developed a nonporous carbon as an alternative to the conventional mesoporous carbon as the catalyst support material for the PtCo NPs in PEM fuel cells. While the catalyst utilization rate (%) in the mesoporous carbon-supported PtCo catalyst was poor below 60% relative humidity (RH), the catalyst utilization rate (%) in the nonporous carbon-supported PtCo catalyst was around 80% under all RH conditions. The authors observed that the majority of PtCo NPs in the mesoporous carbon structure remained in the pores of the carbon, while the PtCo NPs in the nonporous carbon were located on the outer surface of the carbon by using the 3D TEM imaging technique. The PEM fuel cell performance of the PtCo catalyst under low humidity and high current density conditions was improved via facilitated mass transfer by the nonporous carbon. In another study,¹³ three carbon blacks with different textural structures (Ketjen black (KB), Acetylene black (AB), and Vulcan (V)) with a micropore density order of KB>AB>V exhibited the opposite ranking in terms of PEM fuel cell performance. The poorest performance of KB is attributable to those Pt catalysts trapped within the micropores that are no longer accessible.

In this study, inspired by the examples of nonporous carbon utilization in the literature, commercial nonporous carbon black was tried as a support material for Pt catalyst in the cathode electrode of a PEM fuel cell. Besides several physical analyses of nonporous carbon black, it was also electrochemically analyzed in a standard three-electrode cell system. Nonporous carbon black-supported Pt catalyst exhibited fuel cell performance in a PEM fuel cell test station.

MATERIAL AND METHODS

Materials

Conductive nonporous carbon black (purity: 99.9%, size: 24 nm, Nanografi) was used as a catalyst support for Pt NPs. Chloroplatinic acid hydrate (H₂PtCl₆ · 6H₂O, Sigma Aldrich) was used as a precursor for the Pt NPs along with the reducing agent of ethylene glycol (Sigma Aldrich). Nafion 212 polymer membrane was used as an electrolyte in the PEM fuel cell. The anode and cathode electrodes were constructed on the commercial gas diffusion layer (GDL, Sigracet 34 BC). Tanaka catalyst (67.7 wt.% Pt, Pt/C) was used at the anode electrode, while the nonporous carbon black-supported

Pt catalyst was used at the cathode electrode. Nafion solution (15 wt.%, Ion Power) and isopropanol (Sigma Aldrich) were the ingredients of both catalyst inks at the anode and cathode electrodes. 1,2-Propanediol (Sigma Aldrich) was the solvent for nonporous carbon black and Nafion solution in the standard three-electrode cell system's working electrode (WE) ink.

Catalyst Preparation

Pt catalyst on nonporous carbon black was prepared by using microwave-assisted polyol method. The certain amount of nonporous carbon was added to the beaker with 50 mL of ethylene glycol. About 2.6 mL of Pt catalyst precursor solution was added to the mixture. The ultimate solution was mixed for 30 minutes. Therefore, the solution was held on the domestic type microwave oven for 1 minute at 800 W. Pt NPs were loaded on the nonporous carbon in metallic form. At the end of the time, the solution was quickly cooled down to the room temperature. The solid catalyst sample was collected subsequent to the multiple stages of centrifugation and drying processes.¹⁴ Figure 1 shows a schematic representation of the preparation of the Pt catalyst over nonporous carbon black. The microwave technique is an energy- and time-saving technique in the synthesis of heterogeneous catalysts.¹⁵ Especially homogeneously distributed and ultrafine NPs are obtained by the microwave-assisted polyol method, in which ethylene glycol with a high dielectric constant is used as a dispersing and reducing agent.¹⁶ Platinum NPs obtained with this method are generally in the range of 3–5 nm.^{17–20}

Membrane Electrode Assembly (MEA) Preparation

A commercial Tanaka catalyst was used in the anode electrode part of the prepared MEA. Tanaka catalyst and Nafion solution were combined in a specific ratio (70:30) and dissolved in 2-propanol and distilled water. After mixing for a while, the catalyst ink was homogenized. Spraying the produced catalyst ink onto the GDL provided 0.4 mg Pt/cm² loading. To construct the cathode electrode, a Pt catalyst supported by nonporous carbon was dissolved in 2-propanol and water solvents with Nafion solution, homogenized, and sprayed on a separate GDL with a loading of 0.4 mg Pt/cm². Following the construction of the anode and cathode electrodes, a 5 × 5 cm Nafion-212 membrane was placed between the electrodes in contact with the catalyst layers. The triple structure was compressed in a hot press device at 130°C and 400 psi pressure for a certain period. The assembled structure was used as an MEA in the PEM fuel cell test station. Figure 2 shows the preparation steps for MEA.

Physical Characterizations

The physical characterizations of the nonporous carbon black were performed with BET (Micromeritics 3Flex) and X-Ray Diffraction (XRD) (PANalytical Empyrean, Cu K α radiation, operated at 45 kV). The amount of Pt amount on the nonporous carbon black support was detected by an inductively coupled plasma mass spectrometer (ICP-MS, Agilent 7800).

Electrochemical Characterization

Electrochemical characterization of the nonporous carbon black was conducted with the VersaSTAT 3 potentiostat-galvanostat electrochemical analysis instrument. Ag/AgCl, platinum wire, and glassy carbon (GC) electrodes (5 mm diameter, 0.1963 cm²) were employed as the reference electrode, counter electrode, and working electrode in a standard three-electrode cell system, respectively. The WE ink was composed of a carbon sample (70 wt.%), Nafion solution (30 wt.%), 1,2-propanediol, and distilled water. The material loading amount was set to the 28 μ g catalyst

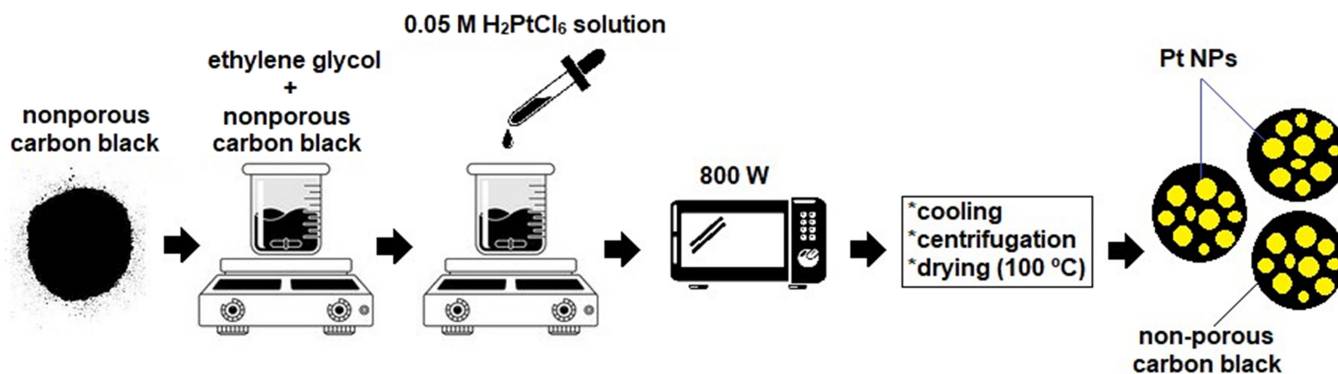


Figure 1. Preparation of a nonporous carbon-supported Pt catalyst.

sample/GC electrode area. About 5 μL of the ultimate WE ink was dropped over the GC electrode and dried at room temperature. Firstly, the potential was linearly swept between the potential range of (–0.28) and (0.92) V at different scan rates (20, 50, and 100 mV/s) through 3 cycles in a N_2 -saturated 0.5 M H_2SO_4 electrolyte solution in CV analysis. Then, CV analysis was continued at the same electrolyte conditions for 3 cycles at a constant scan rate of 50 mV/s but at different upper potential values (0.4, 0.6, 0.8, and 1.0 V). Electrochemical impedance spectroscopy tests (potentiostatic mode; 0.4, 0.65, and 0.9 V) were carried out in N_2 -saturated 0.5 M H_2SO_4 over a frequency range of 1–10⁵ Hz.

The PEM fuel cell performance of a nonporous carbon-supported Pt catalyst was measured using a test station. The prepared MEA was placed on the active region of the single-cell contacting the gas flow channels, and then the cell was closed by compressing the screws at appropriate torque pressures. The cell was swept with nitrogen gas for approximately 1 hour for cleaning and reaching the desired temperatures of the humidification tanks, gas flow lines, and fuel cell before the measurements. The humidification tank temperatures were adjusted to 60°C and 70°C, respectively, while the cell temperature was 70°C. After sweeping, hydrogen gas was fed to the anode side, and oxygen gas was fed to the cathode side. By turning on the load connected to the cell, corresponding current values were recorded starting from the open-circuit voltage and decreasing the voltage at 0.05 V intervals every 30 minutes. Finally, polarization curves were obtained with the recorded potential and current density data.²¹

RESULTS AND DISCUSSION

Brunauer–Emmett–Teller

Brunauer–Emmett–Teller analysis is an empirical technique to calculate surface area per weight or volume by performing gas adsorption experiments on porous materials. Brunauer–Emmett–Teller surface area depends strongly on pore size, structural homogeneity, and the adsorbate-adsorbent relationship.²² Table 1 shows the BET analysis results for the nonporous carbon. The micropore volume of nonporous carbon black is insignificant compared to the cumulative adsorption and desorption volumes, and the surface area was as low as 72.6 m²/g. There is hardly any difference between adsorption and desorption volumes in Figure 3(A). Nitrogen gas is reversibly adsorbed in the form of mono- or multi-layers in nonporous or macroporous solids according to the type-II isotherm.^{23,24} The Barrett–Joyner–Halenda adsorption pore size distribution of nonporous carbon black is shown in Figure 3(B). The average adsorption pore size was in the range of 30–40 nm.

Figure 4 shows the XRD pattern of the nonporous carbon black. Two distinct peaks at around 24° and 43° represent the (002) and (100) planes of graphite, respectively.^{24,25} Additionally, the peak around 80° belongs to the (110) plane of graphite.²⁰ Actually, (002) reflection is positioned at 26°, but the peak appears at smaller angles compared to the crystalline graphite in this case due to its amorphous nature. Because the shift of the (002) plane to lower angle values means there will be a larger d-spacing between the

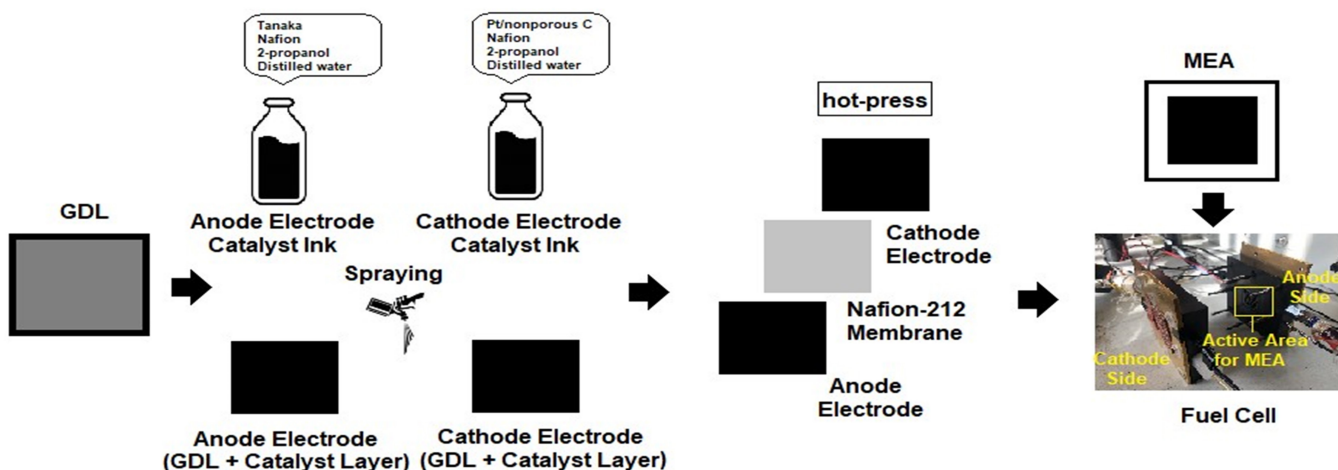


Figure 2. Preparation steps for MEA.

Table 1. Structural Properties of the Nonporous Carbon

Sample	BET Surface Area (m ² /g)	Dubinin–Astakhov Micropore Volume (cm ³ /g)	BJH Adsorption Cumulative Volume of Pores (cm ³ /g)	BJH Desorption Cumulative Volume of Pores (cm ³ /g)	BJH Adsorption Average Pore Width (nm)	BJH Desorption Average Pore Width (nm)
Nonporous carbon	72.6	0.024	0.729	0.728	37.6	31.4

BET, Brunauer–Emmett–Teller; BJH, Barrett–Joyner–Halenda.

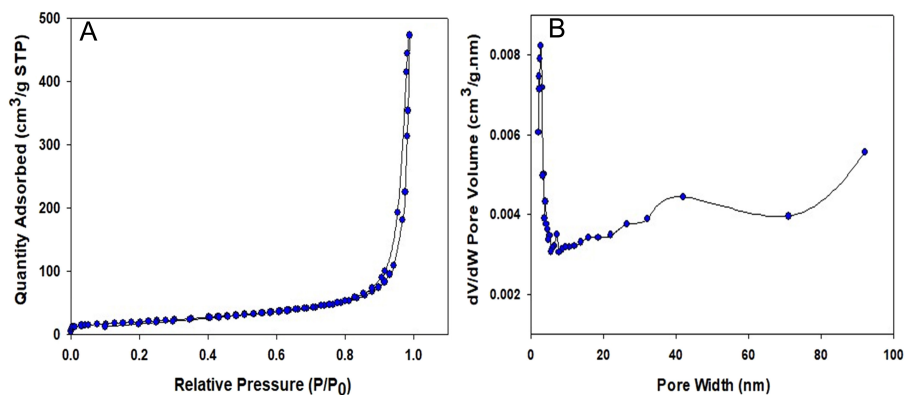


Figure 3. BET analysis of nonporous carbon: (A) adsorption-desorption isotherms; (B) BJH adsorption pore size distribution.

layers, which causes a deviation from the d-spacing (0.335 nm) of crystalline graphite.^{26,27} In reality, when the $d_{(002)}$ value of nonporous carbon black was computed using Bragg's Law,²⁸ it was found to be 0.377 nm, confirming the previous interpretation. Although the structure of carbon black is similar to that of graphite, the difference that distinguishes it from graphite is that it consists of a heterogeneous mixture of turbostratic regions rather than entirely of fine graphite crystals.²⁹ ICP-MS analysis was used to measure the amount of Pt metal loaded on nonporous carbon. As a result of the analysis, the amount of Pt was detected at 15 wt.%. The amount of Pt NPs on the support material is a parameter that affects the porosity and thickness of the catalyst layer. In the literature, the generally accepted Pt loading amount for PEM fuel cell cathode electrodes is 0.4 mg_{Pt}/cm². A lesser amount of Pt/C catalyst with a higher mass Pt% value is adequate to obtain a loading of 0.4 mg_{Pt}/cm²; however, more Pt/C catalyst with a lower mass Pt% value is required to accomplish the same loading. This case leads to an increase in the fraction of carbon and ionomer, thus increasing

the thickness and reducing the porosity of the catalyst layer.³⁰ The thickness of the catalyst layer makes it difficult to transfer the species required for electrochemical reactions to active sites by longer pathways, which causes lower PEM fuel cell performance.³¹

Figures 5(A) and (B) show CV diagrams of nonporous carbon black at different scan rates and upper potential limits, respectively. The capacitive storage feature increases in the CV curves of Figure 5(A) as the scan rate increases.³² In Figure 5(B), the capacitive field becomes more pronounced with the increase in the upper potential limit.³³ The quinone-hydroquinone (Q-HQ) redox peaks appeared at around 0.5–0.7 V in the positive sweep and 0.4–0.6 V in the negative sweep due to the change of the carbon surface with the potential cycling.^{34,35} Carbon support materials undergo electrochemical oxidation and deteriorate due to the production of surface oxides and CO₂/CO in aqueous acidic electrolyte conditions, including the PEM fuel cell. The production of oxygen-containing groups on the carbon surface is triggered, especially at potential values greater than 1 V. Since corrosion promotes carbon loss, the interaction of the support with Pt NPs weakens, and the sintering of Pt NPs accelerates. Furthermore, the decrease in electrode thickness owing to material loss increases resistance and decreases conductivity. All of these unfavorable aspects contribute to poor PEM fuel cell performance. As a result, the corrosion resistance of carbon is critical.³⁶ At scan rates of 20, 50, and 100 mV/s, the current density values obtained by the peak of the Q-HQ redox couple on nonporous carbon black were roughly 0.14, 0.31, and 0.57 mA/cm². According to the CV diagrams acquired at a scan rate of 10 mV/s for holding under 1.2 V (0 h) in Wang et al's work,³⁷ the current density values reached by the peak of the Q-HQ redox couple on Vulcan XC-72 and Black Pearls (BP) 2000 carbon blacks are approximately 1 and 1.5 mA/cm². BP-2000 carbon black is more susceptible to oxidation due to its higher micropore density. Based on the lower current density values obtained for the Q-HQ redox couple in this study, nonporous carbon black will be more resistant to oxidation in the fuel cell environment.

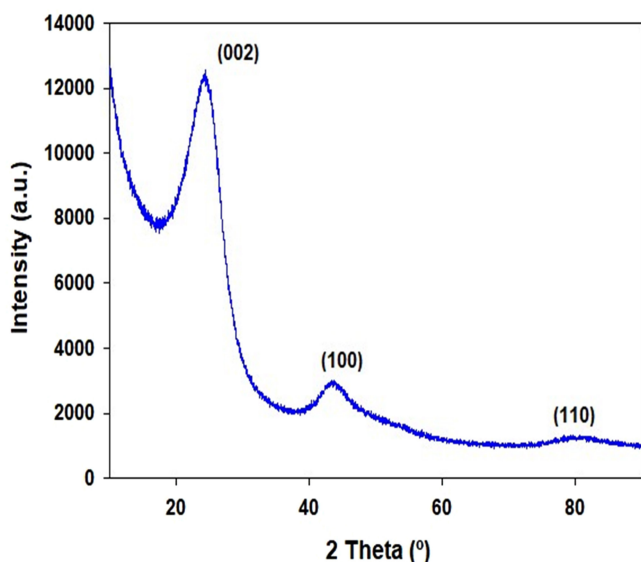


Figure 4. XRD analysis of nonporous carbon.

EIS analysis is a method that provides useful information in a short time to better understand the ORR mechanism in fuel

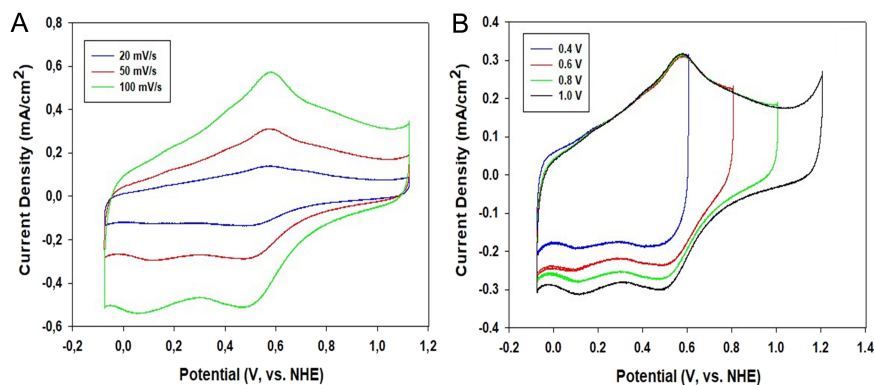


Figure 5. CV measurements of nonporous carbon: (A) different scan rates (20, 50, and 100 mV/s; potential range: -0.28 to 0.92 V); (B) different upper potentials (0.4 , 0.6 , 0.8 , and 1.0 V; scan rate: 50 mV/s).

cells, determine electrode properties, and evaluate diffusion-induced transfer losses.³⁸ Figure 6 shows the Nyquist plots of the nonporous carbon at different voltages. The Nyquist plot fits the fundamental Randles equivalent electrical circuit with membrane and electrolyte resistances (R_s) and charge transfer resistance (R_{CT}) at 0.9 V.³⁹ Table 2 gives the R_s and R_{CT} values as 34.3 Ω and 454.5 Ω , respectively. Liu et al⁴⁰ performed an EIS study on Pt catalysts produced on highly graphitic carbon black (GCB) and Vulcan XC-72 in the frequency range of 0.01 Hz– 100 kHz at 0.54 V in a 0.5 M H_2SO_4 environment. The R_{CT} values of the Pt/GCB and Pt/Vulcan XC-72 catalysts were 331.5 $\Omega \cdot cm^2$ and 443.9 $\Omega \cdot cm^2$, respectively. When we multiply the R_{CT} value we obtained for nonporous carbon black in this study by the electrode area (0.1963 cm^2), we get a value of 89.2 $\Omega \cdot cm^2$. In another study, Yan et al⁴¹ prepared nitrogen (N)/phosphorus (P) co-doped nonporous carbon nanofibers (N/P-NPCNFs) for supercapacitors by the electrospinning method. The EIS analysis (at 1 M H_2SO_4 electrolyte) of the N/P-NPCNFs-5 (63.62 m^2/g), N/P-NPCNFs-10 (33.94 m^2/g), N/P-NPCNFs-20 (12.15 m^2/g), and N/P-NPCNFs-30 (10.34 m^2/g) samples created by varying the polyacrylonitrile/phosphoric acid ratio yielded low R_{CT} values for all of them. It is clear from these examples that nonporous carbon structures can achieve lower R_{CT} values. The lower R_{CT} at the electrode/electrolyte interface means higher ORR activity in the PEM fuel cell.⁴² In the Nyquist

plot given in the inset figure of Figure 6, slope angles higher than 45° were obtained in the high-frequency region in the impedance spectroscopy taken at lower potentials. This case represents the pore structure with a wide mouth and narrowing down shape.⁴³

Figure 7 demonstrates the performances of MEAs prepared with Pt catalysts supported with nonporous carbon at 2 different humidification temperatures. The maximum current density at $60^\circ C$ was recorded as 86 mA/cm^2 and 193 mA/cm^2 at $70^\circ C$. There is a 2.25-fold increase in maximum current density at $70^\circ C$ despite excess water at the cathode electrode at a higher humidification temperature. The Pt catalyst achieved a maximum power density of 15 mW/cm^2 at $60^\circ C$ and 40 mW/cm^2 at $70^\circ C$. The performance values of the nonporous carbon-supported Pt catalyst in this study were better than the results obtained with the Pt catalyst in MEA, which was prepared by Rohendi et al⁴⁴ by the casting method with 1.5 mg/cm^2 Vulcan carbon black loading in its microporous layer. In addition, the mentioned MEA failed in water management, and a rapid decrease in current density was experienced. The nonporous carbon structure can facilitate the removal of excess water released at the cathode electrode by not trapping water in the pores. Since the mass transfer resistance is less in nonporous carbons than in porous carbons, it is easier for water to drain from the catalyst layer, thus preventing the catalyst from overflowing. In this sense, it is thought that it may be advantageous to use nonporous carbon catalyst support at the cathode electrode of a PEM fuel cell. Lefèvre et al⁴⁵ prepared iron (Fe) catalysts on different carbon blacks and used them in the PEM fuel cell. The BET surface areas and micropore areas of SRO, SR1, Vulcan XC-72R, and BP 2000 carbon blacks are ($71;29$), ($441;272$), ($213;114$), and ($1379;934$) m^2/g , respectively. Fe/SRO carbon black gives the best results in PEM fuel cell performances; however, Fe/BP 2000, which has the highest micropore area, deteriorates faster than the others in the high current density region. The authors stated that nonporous SRO carbon black is better than its porous counterparts.

Nonporous carbon structures improve catalyst utilization by ensuring that catalysts are put onto the support material and are in easily accessible locations. Takeshita et al⁴⁶ investigated the Nafion ionomer coating on the cathode electrodes of MEAs made with Pt catalysts placed on commercial nonporous carbon black

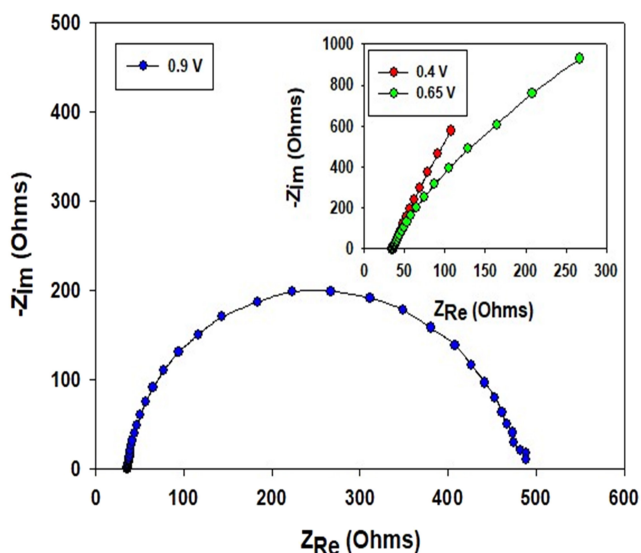


Figure 6. EIS measurements of nonporous carbon.

Table 2. Resistance values of nonporous carbon (@ 0.9 V)

Sample	R_s (Ω)	R_{CT} (Ω)
Nonporous carbon	34.3	454.5

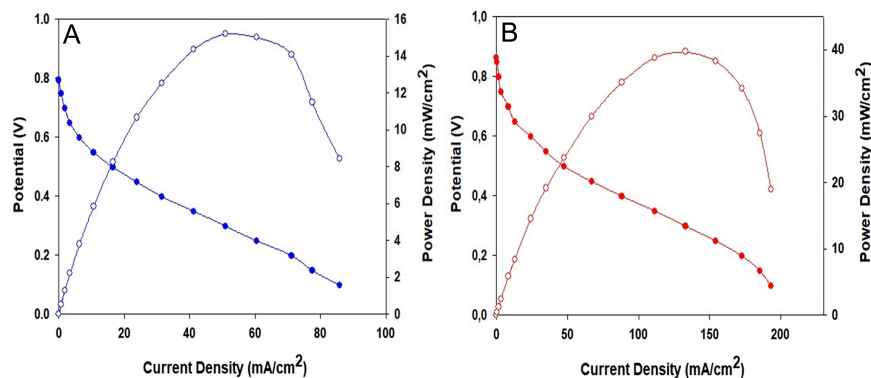


Figure 7. PEM fuel cell performance of the Pt catalyst supported with nonporous carbon at different humidification temperatures (A) 60°C and (B) 70°C.

(Vulcan, MEA-1) and porous carbon blacks (Ketjen Black, MEA-2; Cnovel, MEA-3). The researchers determined that almost all of the Pt NPs on nonporous Vulcan were coated with Nafion ionomer and positioned on the outer surface of carbon. However, they did state that a significant proportion of Pt NPs were found at the inner surface of porous Ketjen Black and Cnovel carbons, and they could not be covered with Nafion ionomer. The authors reported the estimated Nafion coverage percentages as $90 \pm 2\%$ for MEA-1, $60 \pm 7\%$ for MEA-2, and $57.4 \pm 0.3\%$ for MEA-3, respectively. Nonporous carbons also contribute to the fuel cell's durability. Some studies indicate that nonporous carbons give more stability than porous carbons within the catalytic framework. O'Brien et al⁴⁷ used 5 carbon materials (AB (524 m²/g), EA (109 m²/g), E (527 m²/g), VA (70 m²/g), and V (160 m²/g)) with different structures as the support for the PtCo catalyst and tested their durability in PEM fuel cells. In their EIS analysis for carbon materials (at 1.0 A/cm², 80°C, 100% RH), before applying accelerated stress testing (AST), the authors stated that samples with lower surface areas such as VA, EA, and V had lower mass transfer resistance, and this was also associated with the low total micropore volume. In the EIS analyses performed under the same conditions after the AST test, the mass transfer resistance of AB and E carbons with high surface areas increased significantly, while the mass transfer resistance of carbons such as VA, EA, and V did not change noticeably. Additionally, the authors stated that porous carbons such as AB and E were more prone to Co leaching. Tian et al⁴⁸ synthesized Fe/N/C catalysts using extremely microporous BP 2000 (1379 m²/g) and Ketjenblack EC-600JD (1417 m²/g) carbon blacks as well as nonporous N330 carbon black (74 m²/g) and CNT (257 m²/g). According to the normalized mass activities based on polarization curves after holding the catalysts at 0.5 V for different periods, the Fe/N/C catalysts with N330 carbon black and CNT were substantially more stable than those of BP 2000 and Ketjenblack.

Figure 8 depicts the main topics on the advantages of nonporous carbons in PEM fuel cells based on studies in the literature. In these carbons, nonporosity provides better usage of metal catalysts, facile mass transfer of the species, better water management, and long durability.

This study, unlike the examples in the literature, aimed at using a nonporous commercial carbon black as a support material for the PEM fuel cell catalyst. The nonporous structure ensures better metal loading and utilization by preventing the metal NPs from being trapped in the pores of the support material. Platinum metal was used as the catalyst. As a result of the reduction of Pt salt in the microwave, Pt metal was obtained in metallic

form on nonporous carbon. The structural properties of nonporous carbon were evaluated by BET analysis, and its surface area was found to be quite low, 72.6 m²/g. The nonporous carbon BET isotherm exhibited no hysteresis and conformed to the type-II isotherm. Through XRD analysis, it has been understood that nonporous carbon has an amorphous structure.

The nonporous carbon structure was further studied using CV and EIS analyses in a 3-electrode setup. In the CV analysis, it was observed that the capacitive property increased considerably with the increase in the scan rate. In the EIS analysis, it was found that under high potential, nonporous carbon responded appropriately to the Randles cell, and R_s (34.3 Ω) and R_{CT} (454.5 Ω) values were obtained depending on this cell type. Membrane electrode assemblies produced with a nonporous carbon-supported Pt catalyst provided maximum power densities of 15 mW/cm² and 40 mW/cm² at humidification temperatures of 60°C and 70°C, respectively. A balanced drop in fuel cell performance was observed when descending to low voltages with nonporous carbon. In addition, better performance at high humidification showed that water management is proper. Nonporous carbons as alternate catalyst support materials can be used to create

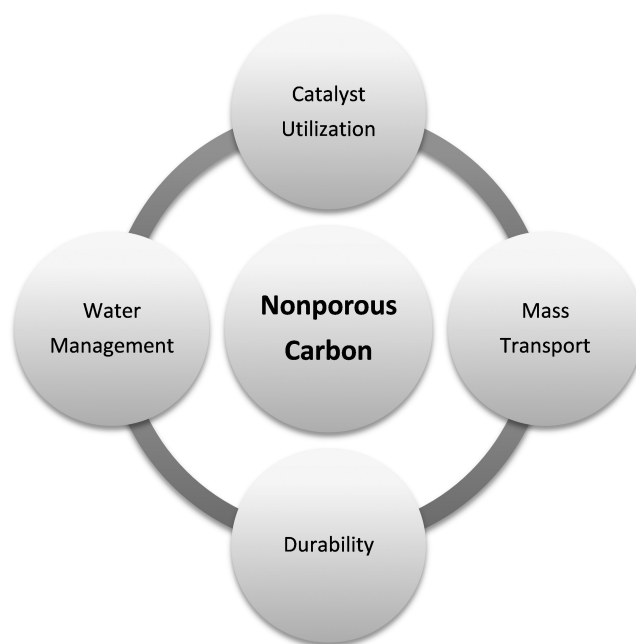


Figure 8. Advantages of nonporous carbons in PEM fuel cells.

high-performance fuel cells with facile water management and long-term durability for portable applications with mW scale.

Peer-review: Externally peer-reviewed.

Acknowledgements: The authors thank the Nanografi Nanotechnology Company for providing commercial nonporous carbon black. The authors also appreciate the East Anatolia High Technology Application and Research Center (DAYTAM) for BET, XRD, and ICP-MS analyses.

Author Contributions: Concept – A.Ö.A.; Supervision – A.B.Y.; Resources – A.B.Y.; Materials – A.Ö.A.; Data Collection and/or Processing – A.Ö.A.; Analysis and/or Interpretation – A.Ö.A.; Writing Manuscript – A.Ö.A., A.B.Y.; Critical Review – A.B.Y.

Declaration of Interests: The authors declare that they have no competing interests.

Funding: The authors declared that this study has received no financial support.

REFERENCES

- Singla MK, Nijhawan P, Oberoi AS. Hydrogen fuel and fuel cell technology for cleaner future: a review (Feb, 10.1007/s11356-020-12231-8, 2021). *Environ Sci Pollut Res*. 2021;28(15):19536-. [CrossRef]
- Öztürk A, Akay RG, Erkan S, Bayrakçeken Yurtcan A. Introduction to fuel cells. In *Direct Liquid Fuel Cells Fundamentals, Advances and Future*. Cambridge: Academic Press; 2020:1-47.
- Wu JB, Yang H. Platinum-based oxygen reduction electrocatalysts. *Acc Chem Res*. 2013;46(8):1848-1857. [CrossRef]
- Çelik P, Bayrakçeken Yurtcan A. Platinum/Vulcan XC-72R electrocatalyst doped with melamine for polymer electrolyte membrane fuel cells. *Nanoera*. 2023;3(1):16-19. [CrossRef]
- Bharti A, Cheruvally G. Influence of various carbon nano-forms as supports for Pt catalyst on proton exchange membrane fuel cell performance. *J Power Sources*. 2017;360:196-205. [CrossRef]
- Soboleva T, Zhao X, Malek K, Xie Z, Navessin T, Holdcroft S. On the micro-, Meso-, and macroporous structures of polymer electrolyte membrane fuel cell catalyst layers. *ACS Appl Mater Interfaces*. 2010;2(2):375-384. [CrossRef]
- Dicks AL. The role of carbon in fuel cells. *J Power Sources*. 2006;156(2):128-141. [CrossRef]
- Kim P, Kim HS, Joo JB, Kim WY, Song IK, Yi JH. Preparation and application of nanoporous carbon templated by silica particle for use as a catalyst support for direct methanol fuel cell. *J Power Sources*. 2005;145(2):139-146. [CrossRef]
- Shahgaldi S, Hamelin J. Improved carbon nanostructures as a novel catalyst support in the cathode side of PEMFC: a critical review. *Carbon*. 2015;94:705-728. [CrossRef]
- Tang J, Liu J, Torad NL, Kimura T, Yamauchi Y. Tailored design of functional nanoporous carbon materials toward fuel cell applications. *Nano Today*. 2014;9(3):305-323. [CrossRef]
- Han L, Zhu X, Yang F, Liu Q, Jia XL. Eco-conversion of coal into a nonporous graphite for high-performance anodes of lithium-ion batteries. *Powder Technol*. 2021;382:40-47. [CrossRef]
- Mizutani N, Ishibashi K. Enhancing PtCo electrode catalyst performance for fuel cell vehicle application. World Congress and Exhibition. SAE International; 2016. [CrossRef]
- Jayawickrama SM, Fujigaya T. Study of polymer-coating on various types of carbon supports to enhance platinum utilization efficiency in polymer electrolyte membrane fuel cell electrocatalysts. *Meet Abstr*. 2019;54:2363-2363. [CrossRef]
- Çögenli MS, Bayrakçeken Yurtcan A. Nanoparticles supported on Bi₂O₃ for direct formic acid fuel cells. *Nanoera*. 2022;2:45-48.
- Bayrakçeken A, Türker L, Eroglu I. Improvement of carbon dioxide tolerance of PEMFC electrocatalyst by using microwave irradiation technique. *Int J Hydrog Energ*. 2008;33(24):7527-7537. [CrossRef]
- Song SQ, Liu JC, Shi JY, et al. The effect of microwave operation parameters on the electrochemical performance of Pt/C catalysts. *Appl Catal B*. 2011;103(3-4):287-293. [CrossRef]
- Wang HW, Dong RX, Chang HY, Liu CL, Chen-Yang YW. Preparation and catalytic activity of Pt/C materials via microwave irradiation. *Mater Lett*. 2007;61(3):830-833. [CrossRef]
- Harish S, Baranton S, Coutanceau C, Joseph J. Microwave assisted polyol method for the preparation of Pt/C, Ru/C and PtRu/C nanoparticles and its application in electrooxidation of methanol. *J Power Sources*. 2012;214:33-39. [CrossRef]
- Knupp SL, Li WZ, Paschos O, Murray TM, Snyder J, Haldar P. The effect of experimental parameters on the synthesis of carbon nanotube/nanofiber supported platinum by polyol processing techniques. *Carbon*. 2008;46(10):1276-1284. [CrossRef]
- Öztürk A, Özçelik N, Bayrakçeken Yurtcan AB. Platinum/graphene nanoplatelets/silicone rubber composites as polymer electrolyte membrane fuel cell catalysts. *Mater Chem Phys*. 2021;260. [CrossRef]
- Özçelik N, Bayrakçeken Yurtcan A. Effect of nitrogen doping amount on the activity of commercial electrocatalyst used in PEM fuel cells. *Nanoera*. 2022;2:5-9.
- Tian Y, Wu JZ. A comprehensive analysis of the BET area for nanoporous materials. *AIChE J*. 2018;64(1):286-293. [CrossRef]
- Bardestani R, Patience GS, Kaliaguine S. Experimental methods in chemical engineering: specific surface area and pore size distribution measurements-BET, BJH, and DFT. *Can J Chem Eng*. 2019;97(11):2781-2791. [CrossRef]
- Yang YW, Hou XY, Ding CF, Lan JL, Yu YH, Yang XP. Eco-friendly fabricated nonporous carbon nanofibers with high volumetric capacitance: improving rate performance by tri-dopants of nitrogen, phosphorus, and silicon. *Inorg Chem Front*. 2017;4(12):2024-2032. [CrossRef]
- Liu C, Shi GF, Wang GY, et al. Preparation and electrochemical studies of electrospun phosphorus doped porous carbon nanofibers. *RSC Adv*. 2019;9(12):6898-6906. [CrossRef]
- Fina F, Callear SK, Carins GM, Irvine JTS. Structural investigation of graphitic carbon nitride via XRD and neutron diffraction. *Chem Mater*. 2015;27(7):2612-2618. [CrossRef]
- Honbo H, Takei K, Ishii Y, Nishida T. Electrochemical properties and Li deposition morphologies of surface modified graphite after grinding. *J Power Sources*. 2009;189(1):337-343. [CrossRef]
- Öztürk A, Bayrakçeken Yurtcan A. Alternative support material to platinum catalyst used for oxygen reduction reaction: nonporous carbon. *Gazi Univ J Sci*. 2023;36(4):1463-1478. [CrossRef]
- Jurkiewicz K, Pawlyta M, Burian A. Structure of carbon materials explored by local transmission electron microscopy and global powder diffraction probes. *C*. 2018;4(4). [CrossRef]
- Zhao J, Ozden A, Shahgaldi S, Alaefour IE, Li XG, Hamdullahpur F. Effect of Pt loading and catalyst type on the pore structure of porous electrodes in polymer electrolyte membrane (PEM) fuel cells. *Energy*. 2018;150:69-76. [CrossRef]
- Avcioglu GS, Fıcicilar B, Eroglu I. Improved PEM fuel cell performance with hydrophobic catalyst layers. *Int J Hydrog Energ*. 2018;43(40):18632-18641. [CrossRef]
- Gupta M, Singh PK, Bhattacharya B, Shulga YM, Shulga NY, Kumar Y. Progress, status and prospects of non-porous, heteroatom-doped carbons for supercapacitors and other electrochemical applications. *Appl Phys A*. 2019;125(2). [CrossRef]
- Stevens DA, Dahn JR. Electrochemical characterization of the active surface in carbon-supported platinum electrocatalysts for PEM fuel cells. *J Electrochem Soc*. 2003;150(6):A770-A775. [CrossRef]
- Macauley N, Papadias DD, Fairweather J, et al. Carbon corrosion in PEM fuel cells and the development of accelerated stress tests. *J Electrochem Soc*. 2018;165:F3148-F3160.
- Kanninen P, Eriksson B, Davodi F, et al. Carbon corrosion properties and performance of multi-walled carbon nanotube support with and without nitrogen-functionalization in fuel cell electrodes. *Electrochim Acta*. 2020;332. [CrossRef]

36. Avasarala B, Moore R, Haldar P. Surface oxidation of carbon supports due to potential cycling under PEM fuel cell conditions. *Electrochim Acta*. 2010;55(16):4765-4771. [\[CrossRef\]](#)
37. Wang JJ, Yin GP, Shao YY, Zhang S, Wang ZB, Gao YZ. Effect of carbon black support corrosion on the durability of Pt/C catalyst. *J Power Sources*. 2007;171(2):331-339. [\[CrossRef\]](#)
38. Wu JF, Yuan XZ, Wang HJ, Blanco M, Martin JJ, Zhang JJ. Diagnostic tools in PEM fuel cell research: Part I - Electrochemical techniques. *Int J Hydrog Energ*. 2008;33(6):1735-1746. [\[CrossRef\]](#)
39. Darowicki K, Gawel L. Impedance measurement and selection of electrochemical equivalent circuit of a working PEM fuel cell cathode. *Electrocatalysis*. 2017;8(3):235-244. [\[CrossRef\]](#)
40. Liu HJ, Li J, Xu XH, et al. Highly graphitic carbon black-supported platinum nanoparticle catalyst and its enhanced electrocatalytic activity for the oxygen reduction reaction in acidic medium. *Electrochim Acta*. 2013;93:25-31. [\[CrossRef\]](#)
41. Yan XD, Liu Y, Fan XR, Jia XL, Yu YH, Yang XP. Nitrogen/phosphorus co-doped nonporous carbon nanofibers for high-performance supercapacitors. *J Power Sources*. 2014;248:745-751. [\[CrossRef\]](#)
42. Chakraborty I, Ghosh N, Ghosh D, Dubey BK, Pradhan D, Ghangrekar MM. Application of synthesized porous graphitic carbon nitride and its composite as excellent electrocatalysts in microbial fuel cell. *Int J Hydrog Energ*. 2020;45(55):31056-31069. [\[CrossRef\]](#)
43. Malko D, Lopes T, Ticianelli EA, Kucernak A. A catalyst layer optimisation approach using electrochemical impedance spectroscopy for PEM fuel cells operated with pyrolysed transition metal-N-C catalysts. *J Power Sources*. 2016;323:189-200. [\[CrossRef\]](#)
44. Rohendi D, Majlan EH, Mohamad AB, Shyuan LK, Raharjo J. Comparison of the performance of proton exchange membrane fuel cell (PEMFC) electrodes with different carbon powder content and methods of manufacture. *Indonesian J Fundam Appl Chem*. 2016;1(3):61-66. [\[CrossRef\]](#)
45. Lefèvre M, Dodelet JP. Fe-based electrocatalysts made with microporous pristine carbon black supports for the reduction of oxygen in PEM fuel cells. *Electrochim Acta*. 2008;53(28):8269-8276. [\[CrossRef\]](#)
46. Takeshita T, Kamitaka Y, Shinozaki K, Kodama K, Morimoto Y. Evaluation of ionomer coverage on Pt catalysts in polymer electrolyte membrane fuel cells by CO stripping voltammetry and its effect on oxygen reduction reaction activity. *J Electroanal Chem*. 2020;871. [\[CrossRef\]](#)
47. O'Brien TE, Herrera S, Langlois DA, et al. Impact of carbon support structure on the durability of PtCo electrocatalysts. *J Electrochem Soc*. 2021;168.
48. Tian J, Birry L, Jaouen F, Dodelet JP. Fe-based catalysts for oxygen reduction in proton exchange membrane fuel cells with cyanamide as nitrogen precursor and/or pore-filler. *Electrochim Acta*. 2011;56(9):3276-3285. [\[CrossRef\]](#)


Nano-Clean: Titanium Dioxide Nanoparticles Via Sol-Gel for Effective Pollutant Removal


Bachir YAOU BALARABE¹ 

Irédon ADJAMA² 

Moumouni Wagé ABDOUL
RAZAK³ 

Hassimi MOUSSA⁴ 

Abdoul Bari IDI AWALI⁵ 

Maman Nasser ILLIASSOU
OUMAROU² 

¹School of Engineering and Technology, National Forensic Sciences University, Gandhinagar, India

²School of Pharmacy, National Forensic Sciences University, Gandhinagar, India

³Department of Exact Sciences, University Andre Salifou, Faculty of Science and Technology, Zinder, Niger

⁴Department of Environmental Sciences, Boubakar Ba University of Tillaberi, Faculty of Agronomic Sciences, Tillaberi, Niger

⁵Department of Chemistry, Abdou Moumouni University, Faculty of Science and Technology, Niamey, Niger

ABSTRACT

The research focused on the hydrothermal synthesis of titanium dioxide (TiO₂) nanoparticles, with a detailed analysis of their chemical attributes through Fourier transform infrared and ultraviolet-visible diffuse reflectance spectroscopy, emphasizing the optical features. The nanoparticles' high purity was further affirmed by energy-dispersive X-ray analysis. Transmission electron microscopy revealed spherical particles measuring ≥ 80 nm. Furthermore, X-ray diffraction and Raman analyses show the anatase structure of the nanomaterial. Under exposure to ultraviolet light, the photocatalytic assessment of 100 mg of the as-synthesized TiO₂ nanoparticles exhibited an impressive efficiency of 77%-90%, successfully removing 30 ppm each of rhodamine B, nonylphenol, roxarsone, and ciprofloxacin within a 105-minute timeframe.

Keywords: Nanoparticles, Pollutant, Removal, TiO₂, UV light

INTRODUCTION

Industrial wastewater discharges, especially from the textile industry, constitute a significant source of environmental pollution and pose a serious threat to life on Earth.¹⁻⁴ In addition to textile effluents, nonylphenol, an endocrine disruptor and a toxic intermediate degradation product of nonylphenol ethoxylates surfactants, poses a significant threat to the environment.^{5,6} The presence of antibiotics in various aquatic environments, including surface water, groundwater, and sewage treatment plant effluents, indicates another emerging environmental problem.⁷⁻⁹ Roxarsone, a commonly used animal feed additive, is excreted into fertilizer without modifications.^{10,11} This fertilizer, frequently used on soil, releases significant quantities of roxarsone, an antimicrobial agent, into the surrounding environment.^{12,13} In addition to the contamination of groundwater and surface water, these pollutants possess the capacity to potentially compromise water bodies through the processes of leaching and runoff.¹⁴⁻¹⁶ To address this risk, the timely removal of pollutants from contaminated wastewater is imperative. Commonly utilized methods for pollution remediation include adsorption, coagulation, membrane filtration, and sedimentation.¹⁷ While these technologies have proven to be effective, the target pollutant is often transferred from one medium to another rather than being completely eliminated.¹⁸ To effectively manage sludge or waste streams, secondary processes are necessary. One potential solution is the utilization of advanced oxidation processes. These processes generate highly oxidizing free radicals capable of mineralizing organic compounds, thereby preventing the formation of waste products.^{7,19} Advanced oxidation processes have garnered considerable attention for their economic viability at a commercial scale. Due to its affordability, chemical stability, and high efficiency in degrading pollutants when exposed to ultraviolet (UV) light, titanium oxide has become the preferred photocatalyst.²⁰ Titanium dioxide has 3 natural polymorphs: anatase, rutile, and brookite. Both anatase and rutile share a tetragonal crystal structure due to their chemical stability. Brookite, less common, possesses an orthorhombic crystal structure. In the remediation of organic pollutants, these variations in crystal structure and particle morphology play a crucial role in influencing the photocatalytic effectiveness of semiconductor catalysts.²¹ In this study, we assess the photocatalytic efficiency of anatase-phase TiO₂ in degrading 4 distinct pollutants.²² Providing precise control over material properties and reducing hydrolysis, sol-gel synthesis is considered ideal for tailored materials. However, its appropriateness relies on the specific material and the desired characteristics.²³⁻²⁵ Using heterogeneous TiO₂ photocatalysis, we discuss the non-aqueous synthesis of TiO₂ nanoparticles for the removal of 4 persistent pollutants, including roxarsone, nonylphenol, rhodamine B, and ciprofloxacin from aquatic systems.

Received: 11.09.2023

Accepted: 21.12.2023

Publication Date: 31.12.2023

Corresponding author:

Bachir YAOU BALARABE

E-mail: bachir.phdnt21@nfsu.ac.in

Cite this article as: Yaou Balarabe B, Adjama I, Wagé Abdoul Razak M, Moussa H, Bari Idi Awali A, Nasser Illiassou Oumarou M. Nano-clean: TiO₂ nanoparticles via sol-gel for effective pollutant removal. *NanoEra* 2023;3(2):61-66.



Content of this journal is licensed under a Creative Commons Attribution-NonCommercial-NoDerivatives 4.0 International License.

MATERIAL AND METHODS

Materials

Analysis of the sample involved employing various spectroscopic and analytical techniques. The JASCO-670 UV/visible (Vis)/near-infrared (IR) spectroscopy captured optical absorbance spectra, while Fourier transform (FT) IR spectra were recorded with the FT-4700 spectroscopy. Transmission electron microscopy (TEM) images were obtained using a Talos F200i S/TEM electron microscope (HRTEM-200KV). Raman spectra were recorded via InVia Raman spectroscopy, and X-ray diffraction (XRD) patterns were acquired with GNR APD 2000 PRO's Cu-K light source. X-ray photoelectron spectra (XPS) were meticulously measured utilizing a Thermo Scientific K-Alpha instrument with an Al K α radiation source.

For the synthesis of sol-gel anatase TiO₂ and the assessment of the nanomaterial's removal potential, reagents were procured from Sigma-Aldrich. These included ethanol (High-performance liquid chromatography) HPLC gradient grade, 99.9%, titanium (IV) butoxide (reagent grade, 97%), and acetic acid (glacial, \geq 99%). Figure 1 illustrates the chemical structures obtained from Sigma-Aldrich for the 4 persistent contaminants used in the study, each indicating

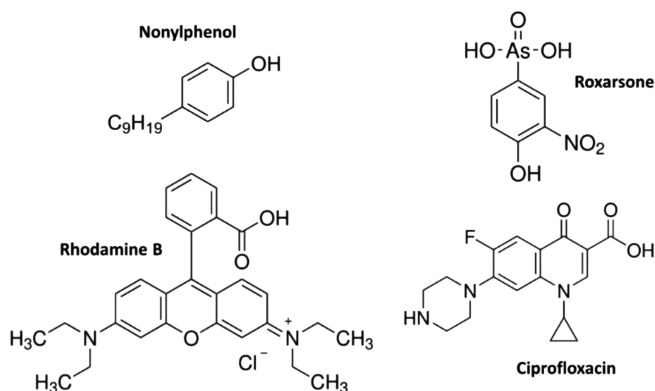


Figure 1. Chemical structure of the pollutants used for the study.

its respective purity: nonylphenol (99% purity), roxarsone (98% purity), ciprofloxacin (98.0% purity), and rhodamine B (95% purity).

Methods

Synthesis of Titanium Dioxide Nanoparticles

The synthesis of TiO₂ nanoparticles followed a procedure derived from our previous method.²⁶ In summary, 30 mL of ethanol were mixed with 20 mL of titanium butoxide and 10 mL of acetic acid. The mixture underwent stirring for 15 hours to facilitate the proper formation of nanoparticles. Subsequently, the resulting gel was matured at 80°C for 9 hours, followed by a 3-hour calcination process at 450°C to produce the nanoparticles. After completing the calcination, the particles were collected and subjected to multiple ethanol washes to eliminate impurities, and finally air-dried at room temperature.

Photocatalytic Activity Measurements

The photocatalytic experiment mirrors our previous research (referenced as Figure 2). Employing a photocatalytic reactor paired with a 125-watt high-pressure mercury UV light source operating at room temperature, we aimed to remove nonylphenol, roxarsone, rhodamine B, and ciprofloxacin in the presence of TiO₂ nanoparticles. In a reactor containing 250 mL of an aqueous solution, each pollutant was present at 30 ppm along with 100 mg of TiO₂ nanoparticles for the photodegradation process.

Before exposing the mixture to irradiation, the stirring process lasted for 20 minutes in the dark using a magnetic stirrer to establish adsorption-desorption equilibrium. Throughout the photoreaction process, the absorbance of 1 mL of solution was measured at regular intervals using a UV-Vis spectrometer. As the concentration of the target substance decreased over time, the absorbance peak also decreased, indicating a reduction in pollutant concentration.

Equation 1, presented below, is typically used to calculate the degradation efficiency of the photocatalyst:

$$\text{Degradation efficiency (\%)} = \frac{\text{Conc.}_0 - \text{Conc.}_t}{\text{Conc.}_0} \times 100 \quad (1)$$

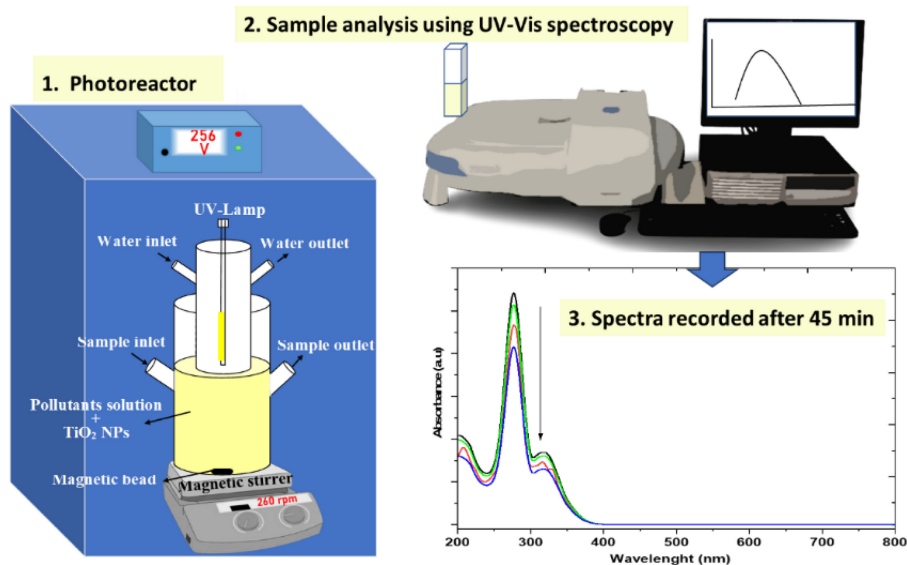


Figure 2. Photocatalytic experiment. UV-Vis, ultraviolet-visible.

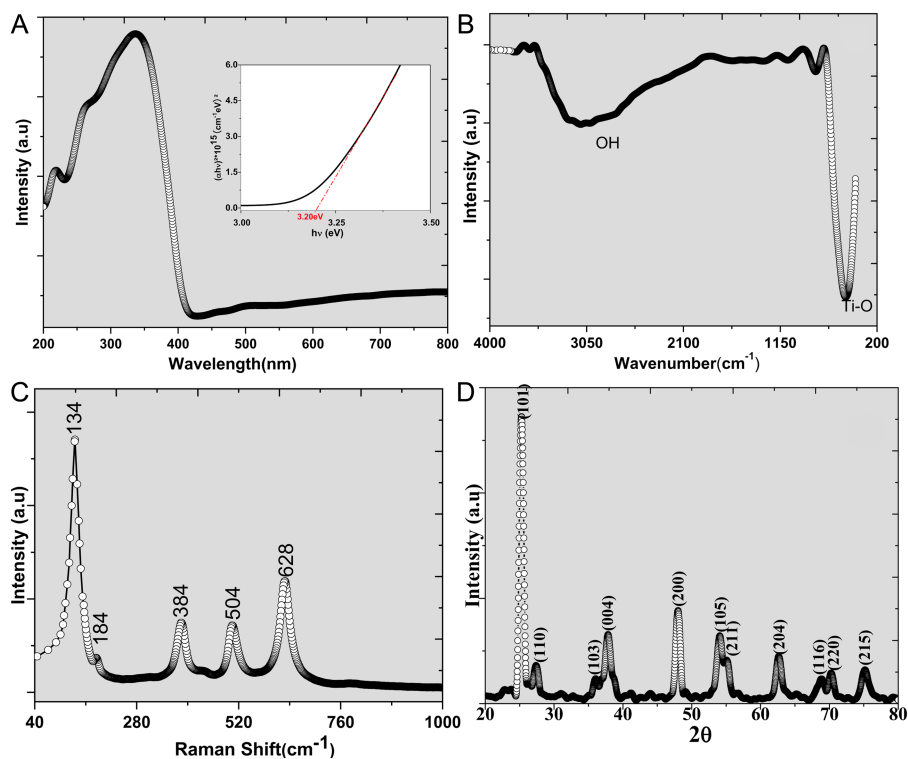


Figure 3. A) Ultraviolet–visible diffuse reflectance spectra, B) the calculated bandgap, C) Raman, and D) X-ray diffraction spectra of TiO₂ nanoparticles.

The variable **Conc.**₀ signifies the initial concentration of the specific pollutant present at equilibrium before the commencement of the experiment. On the other hand, **Conc.**_t represents the concentration of the said pollutant that remains after a duration of *t* during the photocatalytic degradation process.^{27–29}

RESULTS AND DISCUSSION

Within the 200–400 nm range, the characteristics of absorption peaks of TiO₂ nanoparticles are illustrated in Figure 3A, with the primary peak recorded at 350 nm. The inset of Figure 2A reveals

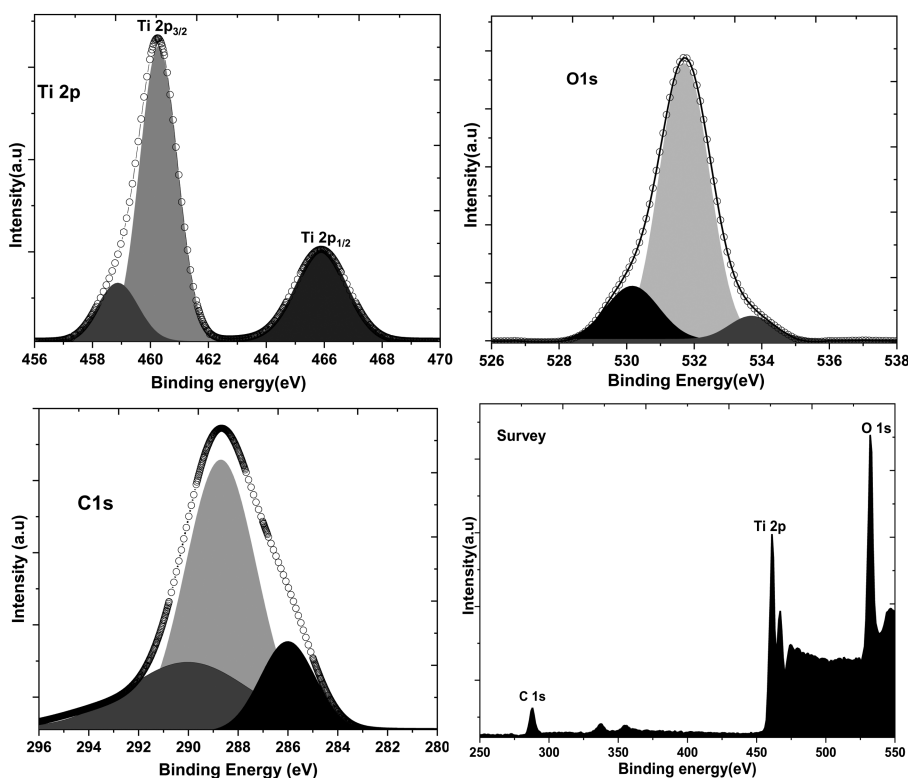


Figure 4. X-ray photoelectron spectra of TiO₂ nanoparticles.

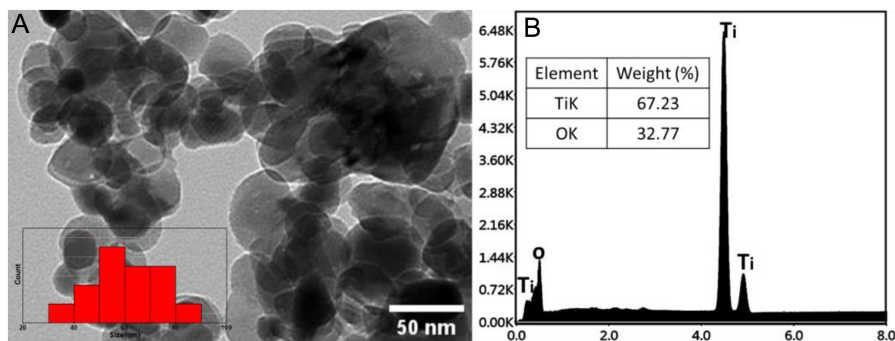


Figure 5. (A) Transmission electron microscopy image (inset), particle size, and (B) Energy-dispersive X-ray spectroscopy (EDS) graph of TiO_2 nanoparticles.

the calculated band gap of the TiO_2 nanoparticles, determined to be 3.2 eV. This band gap aligns with the value reported for TiO_2 anatase.³⁰

The FTIR spectrum provides essential information about the organic molecules that envelop the surfaces of nanoparticles. Vibrations at a wavenumber of 3151 cm^{-1} (refer to Figure 3B) confirm the presence of OH groups on the TiO_2 nanoparticles. Furthermore, the vibration at 521 cm^{-1} indicates the Ti-O group vibration.³¹

Peaks at positions $134, 384, 504,$ and 628 cm^{-1} , corresponding to Eg, B1g, A1g/B1g, and A1g modes, respectively, are indicated by the Raman results of TiO_2 nanoparticles (Figure 3C). These modes align with typical TiO_2 anatase modes as reported in previous studies on TiO_2 nanoparticles.¹⁷ Distinctive peaks associated with anatase titanium dioxide are observable in the XRD pattern of the synthesized TiO_2 nanoparticles (refer to Figure 3D). The anatase

phase of titania is identified by its characteristic peaks located at $25.3^\circ, 37.8^\circ, 48.1^\circ, 54.0^\circ, 55.0^\circ, 62.7^\circ,$ and 68.8° (JCPDS #21-1272).

The XPS analysis conducted on the TiO_2 nanoparticles uncovers the presence of titanium (Ti) and oxygen (O) elements, along with indications of air contamination (refer to Figure 4). Within the Ti2p spectrum, 2 prominent peaks emerge at 458.4 eV and 464.0 eV, corresponding to $\text{Ti}2p_{3/2}$ and $\text{Ti}2p_{1/2}$, respectively. These peak positions align with the reported binding energies for Ti in TiO_2 , affirming that the Ti within the TiO_2 nanoparticles exists in both +4 and +2 oxidation states.^{17,32,33} A distinct peak at approximately 530 eV is observed within the O1s spectrum of the TiO_2 nanoparticles, precisely aligning with the characteristic binding energy of oxygen in TiO_2 .³⁴ A peak is detected at 284.6 eV in the C1s spectrum, corresponding to the binding energy of carbon typically found in hydrocarbons. This observed peak is likely attributed to surface contamination resulting from exposure to air.³⁵

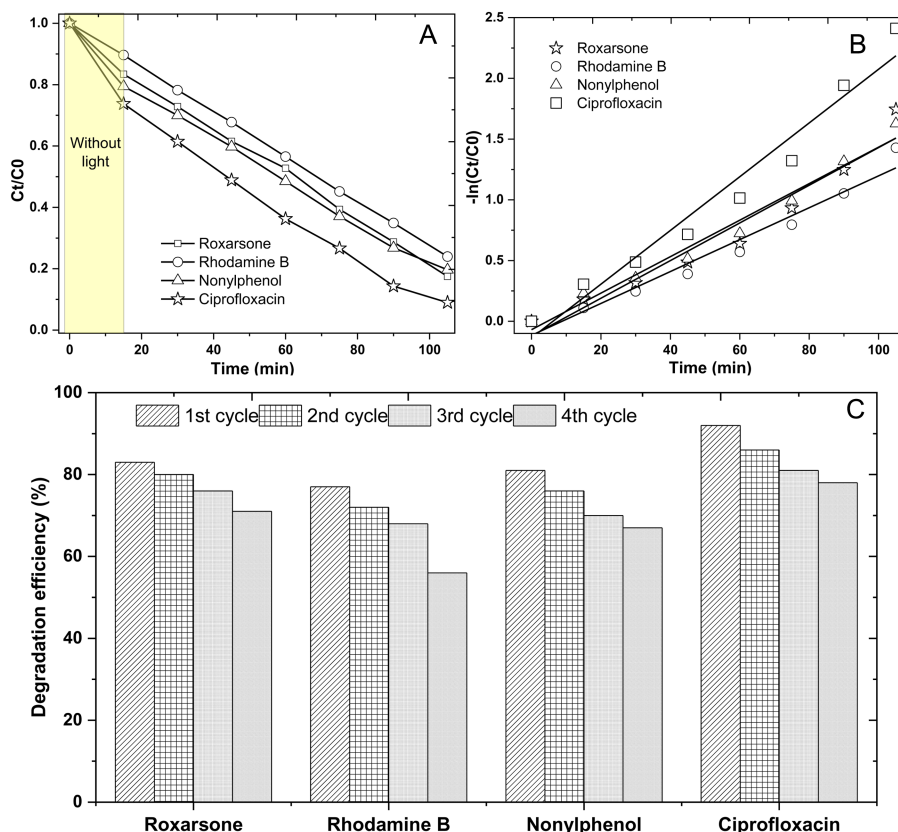


Figure 6. A) Roxarsone, B) Rhodamine B, C) Ciprofloxacin and D) Nonylphenol degradation efficiency using TiO_2 nanoparticles.

The spherical shape of the TiO₂ nanoparticles, with a size of ≥80 nm (depicted in the inset of Figure 5A), is evident in the TEM image (Figure 5A). Additionally, the TiO₂ nanoparticles exhibit high purity, as confirmed by the presence of both titanium (Ti) and oxygen (O) elements (Figure 5B). Specifically, the nanoparticle composition comprises 67.23% titanium (Ti) and 32.77% oxygen (O).

PHOTOCATALYTIC EFFICIENCY

After 105 minutes, the UV absorbance readings demonstrate degradation efficiencies of 83% for roxarsone, 77% for rhodamine B, 81% for nonylphenol, and 92% for ciprofloxacin (refer to Figure 6A). To calculate the kinetic rate constant using equation 2, a pseudo-first-order kinetic equation was applied to quantify these degradation rates. Utilizing this mathematical approach offers a comprehensive insight into degradation kinetics, emphasizing the dynamics of the reaction over time.^{36,37}

$$-\ln \frac{\text{Conc}_0}{\text{Conc}_t} = k_t \quad (2)$$

Upon examining the linear logarithmic plot against irradiation time, it becomes apparent that the photodegradation reaction closely adheres to first-order kinetics, displaying an almost linear pattern. In this study, the rate constants (k) for this reaction have been calculated as 0.012, 0.011, 0.015, and 0.02 min⁻¹ for roxarsone, rhodamine B, nonylphenol, and ciprofloxacin, respectively. Figure 5B effectively illustrates the remarkable photocatalytic efficacy of TiO₂ nanoparticles based on the derived “ k ” values.

The particles were reused for 4 cycles of treatment. Following each treatment, the particles were collected and subjected to multiple washes with distilled water and ethanol. As depicted in Figure 6C, the photocatalytic degradation of pollutants after the fourth cycle treatment shows no significant change, confirming the stability of the particles.

This study successfully demonstrated a single-step sol-gel synthesis of TiO₂ nanoparticles. The photocatalytic experiments underscored the effectiveness of TiO₂ nanoparticles in removing several pollutants under UV light. Notably, remarkable degradation efficiencies ranging from 77% to 92% were achieved for rhodamine B, nonylphenol, roxarsone, and ciprofloxacin after 105 minutes of irradiation. Spectroscopic and microscopic analyses unveiled the nanoparticles' anatase structure and uniform distribution, indicating their promising suitability for practical applications. This study makes a significant contribution to advancing environmentally friendly technologies and practices by effectively addressing the challenge of eliminating these persistent pollutants.

Peer-review: Externally peer-reviewed.

Author Contributions: Concept – I.A., A.R.M.W., H.M., A.B.I.A., M.N.I.O.; Supervision – I.A., A.R.M.W., H.M., A.B.I.A., M.N.I.O.; Resources – I.A., A.R.M.W., H.M., A.B.I.A., M.N.I.O.; Materials – I.A., A.R.M.W., H.M., A.B.I.A., M.N.I.O.; Data Collection and/or Processing – I.A., A.R.M.W., H.M., A.B.I.A., M.N.I.O.; Analysis and/or Interpretation – I.A., A.R.M.W., H.M., A.B.I.A., M.N.I.O.; Writing Manuscript – I.A., A.R.M.W., H.M., A.B.I.A., M.N.I.O.; Critical Review – I.A., A.R.M.W., H.M., A.B.I.A., M.N.I.O.

Acknowledgments: We are grateful for the assistance provided by the National Forensic Sciences University.

Declaration of Interests: The authors declare that they have no competing interests.

Funding: The authors declared that this study has received no financial support.

REFERENCES

- Danner MC, Robertson A, Behrends V, Reiss J. Antibiotic pollution in surface fresh waters: occurrence and effects. *Sci Total Environ*. 2019;664:793-804. [\[CrossRef\]](#)
- Balarabe BY, Bowmik S, Ghosh A, Maity P. Photocatalytic dye degradation by magnetic XFe₂O₃ (X: Co, Zn, Cr, Sr, Ni, Cu, Ba, Bi, and Mn) nanocomposites under visible light: a cost efficiency comparison. *J Magn Magn Mater*. 2022;562:169823. [\[CrossRef\]](#)
- Yaou Balarabe B, Illiassou Oumarou MN, Koroney AS, Adjama I, Ibrahim Baraze AR. Photo-oxidation of organic dye by Fe₂O₃ nanoparticles: catalyst, electron acceptor, and polyurethane membrane (PU-Fe₂O₃) effects. *J Nanotechnol*. 2023;2023:1-12. [\[CrossRef\]](#)
- Balarabe BY, Maity P, Teixeira ACSC, Iwarere SA. h-BN nanosheet-modified Ag₂WO₄ nanocomposite for improved photocatalytic dye removal: insights into catalyst stability and reusability. *Inorg Chem Commun*. 2023;158. [\[CrossRef\]](#)
- Dzinun H, Othman MHD, Ismail AF, Puteh MH, Rahman MA, Jaafar J. Photocatalytic degradation of nonylphenol by immobilized TiO₂ in dual layer hollow fibre membranes. *Chem Eng J*. 2015;269:255-261. [\[CrossRef\]](#)
- Balarabe BY, Irédon A, Hassimi M, Illiassou Oumarou MN, Masiyambiri V, Gunda TJ. Effective removal of emerging organic pollutants using hybrid Ag@ZnO supported reduced-graphene oxide nanocomposite under visible light. *Hybrid Advances*. 2023;100114. [\[CrossRef\]](#)
- Hu X, Hu X, Peng Q, et al. Mechanisms underlying the photocatalytic degradation pathway of ciprofloxacin with heterogeneous TiO₂. *Chem Eng J*. 2020;380. [\[CrossRef\]](#)
- Yaou Balarabe B, Paria S, Sekou Keita D, et al. Enhanced UV-light active α-Bi₂O₃ nanoparticles for the removal of methyl orange and ciprofloxacin. *Inorg Chem Commun*. 2022;146:110204. [\[CrossRef\]](#)
- Masiyambiri V, Yaou Balarabe B, Adjama I, Moussa H, Illiassou Oumarou MN, Iro Sodo AM. A study of the phytoremediation process using water lettuce (*Pistia Stratiotes*) in the removal of ciprofloxacin. *Am J Life Sci Innov*. 2023;1(3):1-8. [\[CrossRef\]](#)
- Jackson BP, Bertsch PM, Cabrera ML, Camberato JJ, Seaman JC, Wood CW. Trace element speciation in poultry litter. *J Environ Qual*. 2003;32(2):535-540. [\[CrossRef\]](#)
- Bednar AJ, Garbarino JR, Ferrer I, et al. Photodegradation of roxarsone in poultry litter leachates. *Sci Total Environ*. 2003;302(1-3):237-245. [\[CrossRef\]](#)
- Makris KC, Quazi S, Punamiya P, Sarkar D, Datta R. Fate of arsenic in swine waste from concentrated animal feeding operations. *J Environ Qual*. 2008;37(4):1626-1633. [\[CrossRef\]](#)
- Liu X, Zhang W, Hu Y, Cheng H. Extraction and detection of organoarsenic feed additives and common arsenic species in environmental matrices by HPLC-ICP-MS. *Microchem J*. 2013;108:38-45. [\[CrossRef\]](#)
- Olsen CE, Liguori AE, Zong Y, Lantz RC, Burgess JL, Boitano S. Arsenic upregulates MMP-9 and inhibits wound repair in human airway epithelial cells. *Am J Physiol Lung Cell Mol Physiol*. 2008;295(2):L293-L302. [\[CrossRef\]](#)
- Stolz JF, Perera E, Kilonzo B, et al. Biotransformation of 3-nitro-4-hydroxybenzene arsonic acid (Roxarsone) and release of inorganic arsenic by clostridium species. *Environ Sci Technol*. 2007;41(3):818-823.
- D'Angelo E, Zeigler G, Beck EG, Grove J, Sikora F. Arsenic species in broiler (*Gallus gallus domesticus*) litter, soils, maize (*Zea mays* L.), and groundwater from litter-amended fields. *Sci Total Environ*. 2012;438:286-292. [\[CrossRef\]](#)
- Balarabe BY, Maity P. Visible light-driven complete photocatalytic oxidation of organic dye by plasmonic Au-TiO₂ nanocatalyst under

- batch and continuous flow condition. *Colloids Surf A Physicochem Eng Asp.* 2022;655:130247. [\[CrossRef\]](#)
18. Rauf MA, Meetani MA, Hisaindee S. An overview on the photocatalytic degradation of azo dyes in the presence of TiO₂ doped with selective transition metals. *Desalination.* 2011;276(1-3):13-27. [\[CrossRef\]](#)
 19. Emadian SS, Ghorbani M, Bakeri G. Magnetically separable CoFe₂O₄/ZrO₂ nanocomposite for the photocatalytic reduction of hexavalent chromium under visible light irradiation. *Synth Met.* 2020;267:116470.
 20. Gil A, García AM, Fernández M, et al. Effect of dopants on the structure of titanium oxide used as a photocatalyst for the removal of emergent contaminants. *J Ind Eng Chem.* 2017;53:183-191. [\[CrossRef\]](#)
 21. Ohtani B, Prieto-Mahaney OO, Li D, Abe R. What is Degussa (Evonik) P25? Crystalline composition analysis, reconstruction from isolated pure particles and photocatalytic activity test. *J Photochem Photobiol A.* 2010;216(2-3):179-182.
 22. Ohtani B. Preparing articles on photocatalysis - beyond the illusions, misconceptions, and speculation. *Chem Lett.* 2008;37(3):216-229. [\[CrossRef\]](#)
 23. Crnjak Orel Z. MICROWAVE-ASSISTED NON-AQUEOUS SYNTHESIS OF ZnO NANOPARTICLES SINTEZA NANODELCEV ZnO V NEVODNEM MEDIJU POD VPLIVOM MIKROVALOV.
 24. Shankar R, Groven L, Amert A, Whites KW, Kellar JJ. Non-aqueous synthesis of silver nanoparticles using tin acetate as a reducing agent for the conductive ink formulation in printed electronics. *J Mater Chem.* 2011;21(29):10871-10877. [\[CrossRef\]](#)
 25. Lamiel C, Nguyen VH, Tuma D, Shim JJ. Non-aqueous synthesis of ultrasmall NiO nanoparticle-intercalated graphene composite as active electrode material for supercapacitors. *Mater Res Bull.* 2016;83:275-283. [\[CrossRef\]](#)
 26. Marycleopha M, Balarabe BY, Adjama I, Hassimi M, Anandaram H, Razak MWA. Anhydrous sol-gel synthesis of anatase TiO₂ nanoparticles: evaluating their impact on protein interactions in biological systems. *J Trace Elem Med.* 2023;100114. [\[CrossRef\]](#)
 27. Atchudan R, Edison TNJI, Perumal S, Karthikeyan D, Lee YR. Facile synthesis of zinc oxide nanoparticles decorated graphene oxide composite via simple solvothermal route and their photocatalytic activity on methylene blue degradation. *J Photochem Photobiol B.* 2016;162:500-510. [\[CrossRef\]](#)
 28. Feng Y, Feng N, Wei Y, Zhang G. An in situ gelatin-assisted hydrothermal synthesis of ZnO-reduced graphene oxide composites with enhanced photocatalytic performance under ultraviolet and visible light. *RSC Adv.* 2014;4(16):7933-7943. [\[CrossRef\]](#)
 29. Karimipour M, Sadeghian M, Molaei M. Fabrication of white light LED photocatalyst ZnO-rGO heteronanosheet hybrid materials. *J Mater Sci Mater Electron.* 2018;29(16):13782-13793. [\[CrossRef\]](#)
 30. Bamola P, Sharma M, Dwivedi C, et al. Interfacial interaction of plasmonic nanoparticles (Ag, Au) decorated floweret TiO₂ nanorod hybrids for enhanced visible light driven photocatalytic activity. *Mater Sci Eng B.* 2021;273:115403. [\[CrossRef\]](#)
 31. León A, Reuquen P, Garín C, et al. FTIR and Raman characterization of TiO₂ nanoparticles coated with polyethylene glycol as carrier for 2-methoxyestradiol. *Appl Sci.* 2017;7(1). [\[CrossRef\]](#)
 32. Yaou Balarabe B, Maity P. A polymer-Au/TiO₂ nano-composite based floating catalyst for photocatalytic dye degradation under natural sunlight. *J Photochem Photobiol A.* 2024;449:115405. [\[CrossRef\]](#)
 33. Yaou Balarabe B. B. Green synthesis of gold-titania nanoparticles for sustainable ciprofloxacin removal and phytotoxicity evaluation on aquatic plant growth. *Hybrid Adv.* 2023;4:100107. [\[CrossRef\]](#)
 34. Mezni A, Ibrahim MM, El-Kemary M, et al. Cathodically activated Au/TiO₂ nanocomposite synthesized by a new facile solvothermal method: an efficient electrocatalyst with Pt-like activity for hydrogen generation. *Electrochim Acta.* 2018;290:404-418. [\[CrossRef\]](#)
 35. Mao J, Zhao B, Zhou J, et al. Identification and characteristics of catalytic quad-functions on Au/anatase TiO₂. *ACS Catal.* 2019;9(9):7900-7911. [\[CrossRef\]](#)
 36. Potle VD, Shirsath SR, Bhanvase BA, Saharan VK. Sonochemical preparation of ternary rGO-ZnO-TiO₂ nanocomposite photocatalyst for efficient degradation of crystal violet dye. *Optik.* 2020;208. [\[CrossRef\]](#)
 37. Di X, Guo F, Zhu Z, Xu Z, Qian Z, Zhang Q. In situ synthesis of ZnO-GO/CGH composites for visible light photocatalytic degradation of methylene blue. *RSC Adv.* 2019;9(70):41209-41217. [\[CrossRef\]](#)